

THESIS ON INFORMATICS AND SYSTEM ENGINEERING C120

# **Fluid Body Interaction of Biomimetic Underwater Robots**

GERT TOMING

**TUT**  
PRESS

TALLINN UNIVERSITY OF TECHNOLOGY  
Faculty of Information Technology  
Centre for Biorobotics

**This dissertation was accepted for the defence of the degree of Doctor of Philosophy in Computer and Systems Engineering on December 16, 2016.**

**Supervisor:** Prof. Maarja Kruusmaa  
Centre for Biorobotics  
Tallinn University of Technology  
Tallinn, Estonia

**Opponents:** Prof. John Hallam  
SDU Embodied Systems for Robotics and Learning  
The Maersk Mc-Kinney Moller Institute  
University of Southern Denmark  
Odense, Denmark

Assoc. Prof. Jo Arve Alfredsen  
Department of Engineering Cybernetics  
Norwegian University of Science and Technology (NTNU)  
Trondheim, Norway

**Defence of the thesis:** February 21, 2017, Tallinn

**Declaration:**

*Hereby I declare that this doctoral thesis, my original investigation and achievement, submitted for the doctoral degree at Tallinn University of Technology has not been submitted for doctoral or equivalent academic degree.*

*Gert Toming*



European Union  
European Social Fund



Investing in your future

Copyright: Gert Toming, 2017  
ISSN 1406-4731  
ISBN 978-9949-83-071-8 (publication)  
SBN 978-9949-83-072-5 (PDF)

INFORMAATIKA JA SÜSTEEMITEHNIKA C120

# **Biomimeetiliste robotite ja vedeliku vastasmõju**

GERT TOMING



# Table of Contents

ABSTRACT .....	8
KOKKUVÕTE .....	10
ACKNOWLEDGEMENTS .....	12
LIST OF PUBLICATIONS .....	13
AUTHOR’S CONTRIBUTION TO THE PUBLICATIONS .....	14
OTHER RELATED PUBLICATIONS .....	15
INTRODUCTION .....	19
CONTRIBUTION OF THE THESIS .....	21
1 BACKGROUND .....	22
1.1. Fish locomotion .....	22
1.1.1. Physics of fish locomotion.....	24
1.1.2. Locomotion in turbulence .....	26
1.2. Fish migration .....	28
1.2.1. Problems of migration.....	29
1.3 Experimental fluid dynamics .....	30
1.3.1. Pressure and velocity .....	31
1.3.2. Force measurements.....	32
1.4. Particle image velocimetry .....	32
1.4.1. Light sources and light sheet optics .....	33
1.4.2. Tracer particles .....	35
1.4.3. Imaging .....	38
1.4.4. Data processing.....	39
1.5. Conclusions.....	40
2 FACILITIES AND EQUIPMENT USED IN THIS THESIS.....	41
2.1. Flow tunnels.....	41
2.1.1. Submerged flow tunnel in Tallinn University of Technology .....	41
2.1.2. Open top flow tunnel in the University of Stuttgart.....	42
2.1.3. Model of a vertical slot fish pass .....	43
2.2. Measurement equipment.....	43

2.2.1. PIV system Version 1 .....	43
2.2.2. PIV system Version 2 .....	44
2.2.3. Force plate Version 1 .....	45
2.2.4. Force plate Version 2 .....	45
2.3. Prototypes .....	45
2.3.1. Prototype 1 .....	46
2.3.2. Prototype 2 – fish dummies .....	47
2.3.3. Prototype 3 – the X-prototype.....	48
2.3.4. Lateral line probe .....	49
2.4. Conclusions.....	50
3 POSITIONING IN A VORTEX STREET .....	51
3.1. Materials and methods .....	51
3.2. Results of flow analysis .....	52
3.3. Results of force measurements .....	53
3.4. Conclusions and discussion .....	55
4 BODY LENGTH TO WAKE WAVELENGTH RATIO.....	57
4.1. Materials and methods .....	57
4.2. Results of flow analysis .....	58
4.3. Results of force measurements .....	59
4.4. Conclusion and discussion.....	62
5 IMPLEMENTATION AND IMPROVEMENT OF INDIRECT FORCE MEASUREMENTS.....	65
5.1. Materials and methods .....	65
5.2. Data analysis .....	66
5.3. Results.....	67
5.4. Conclusions and discussion .....	68
6 LATERAL LINE PROBE FOR STUDYING FISH PASSES .....	70
6.1. Materials and methods .....	70
6.2. Validation results .....	71
6.3. Initial evaluation of fishways.....	73
6.4. Conclusions and discussion .....	75

CONCLUSIONS .....	77
REFERENCES .....	79
Appendix A.....	95
Appendix B.....	103
Appendix C.....	117
Appendix D.....	131
CURRICULUM VITAE.....	143
ELULOOKIRJELDUS .....	144

## ABSTRACT

Earth is a water planet, and organisms have evolved an impressive array of complementary methods to detect, transmit and receive underwater signals. Current underwater robots and flow sensing systems are quite primitive in comparison to their biological counterparts. As an example, for modern undulatory swimming robots turbulence is considered as a major source of disturbance, whereas living fish can utilize complex flows to enhance their propulsive efficiency. Bioinspired underwater robotics therefore strives to study, design and implement propulsion and sensing modalities similar to their biological counterparts. This thesis presents four studies investigating these problems. The work was experimental and consisted of tests in different flow tanks including flow measurements with particle image velocimetry, acoustic Doppler velocimetry (ADV) and laser Doppler anemometry (LDA), direct and indirect force measurements.

The interaction of a bioinspired fish-like robot with regular turbulence was studied. First, separate flow regions in a Kàrmàn vortex street were explored by varying the fish robot's position behind the cylinder longitudinally and laterally. Different regions in the flow were detected, and it was found that a total drag reduction of up to 42% could be achieved, depending on the position of the robot relative to the obstacle. Second, the relation of robotic fish body length to the oncoming vortex street wake wavelength was studied. It was shown how the balance of hydrodynamic forces causing yaw and sway motion change when the body length increases and even exceeds the wake wavelength. The presented relations are valuable for roboticists as to the author's knowledge there are no conclusive studies about the position and size of the robot or fish relative to the obstacle that creates turbulence.

For precise force measurements the measured object must be fixed to the measurement device. This method however has limitations for measuring undulatory swimming robots and is not applicable for real fishes at all. The dynamic force balance can also be calculated from an interrogation of the velocity vector field. In this thesis we propose a novel methodology to improve those indirect force measurements. With the help of a general linear transfer function we have reduced the errors associated with instantaneous force measurements considerably – up to 69% in the streamwise direction and up to 83% in the lateral direction. Allowing for robust and accurate force measurements of undulatory swimmers without complex and time consuming calibration processes or manual detection of flow regions and the need to physically harness the robot or fish to the measurement device.

Currently, there exists a knowledge deficit in measurement systems capable of assessing complex natural flows. We introduce a novel bioinspired measurement device – the lateral line probe. It is meant to measure complex natural flows in rivers and fish passes as the real fish senses the flow. By testing the probe in different flow tunnels and real fish passes we showed it is possible to measure

and present flow and pressure maps surrounding its fish shaped body as well as calculate flow velocities comparable to standard acoustic ADV and LDA devices.

The knowledge gained from the position and size relation to the hydrodynamic forces affecting fish shaped objects in a turbulence can be used to design more energy efficient underwater robots for flowing waters and other complex environments. The design can be further improved by combining the technology from the lateral line probe to underwater robots for better assessment of flow conditions. The probe can be used as a static device or included as a multimodal collocated sensing array on underwater robots. The long-term goal is to use this new technology to measure fishways, leading to new knowledge on the complex fluid-body reactions which can be leveraged to restore fish migration.

## KOKKUVÕTE

Maad katab suures osas vesi ja siin elutsevatel organismidel on tuhandete aastate jooksul välja arenenud muljetavaldavad võimed veekeskkonnas liikumiseks ning seal erinevate signaalide väljasaatmiseks ja vastuvõtmiseks. Tänapäevased allveerobotid ja mõõtesüsteemid ei suuda loodusega võistelda, ei signaalide tajumises ega ka liikumises. Kalad näiteks suudavad adapteeruda turbulentsiga ja seda enda huvides kasutada, aga robotite jaoks põhjustab turbulents häireid, nii et seda tuleb vältida või osata selle mõjusid kompenseerida. Bioloogist inspireeritud allveerobootika püüdlebki selle poole, et õppida oma bioloogilistelt eeskujudelt ning järjest paremini projekteerida ja ehitada nende meeleeelunditele ja liikumismehhanismidele sarnaseid tehnilisi lahendusi. Käesolev doktoritöö annab ülevaate neljast eksperimentaalsest uurimustööst selles valdkonnas. Nendes kasutati kalaroboteid, erinevaid voolutunneleid, veevoolu kiiruse mõõtmise vahendeid – Doppleri akustilist anemomeetrit (ADV), laseranemomeetrit (LDA) ja heljumikiirusvälja digifotograafiat (PIV) ning jõumõõtmise seadmeid.

Uuriti kalarobotite ja turbulentsse veevoolu vastasmõju Kärnäni tänavas. Selleks paigutati kalarobot keeriseid tekitava poolsilindri taha erinevatele kaugustele, samuti muudeti positsiooni voolutunneli ristisuunas. Selle tulemusena tehti kindlaks erinevad regioonid poolsilindri taga ja leiti, et sõltuvalt kalaroboti asetusel on võimalik tema takistusjõudu vähendada kuni 42%. Järgnevalt uuriti kalaroboti kehapiikkuse ja keeriste tänava lainepikkuse suhet, näidates eksperimentaalselt, kuidas muutuvad külgsuunalised jõud ja nende eeldatav mõju, kui muutub kalaroboti ja Kärnäni tänava suuruse suhe. Esitletud tulemused on väärtuslikud robotikutele ja bioloogidele, kuna autorile teadaolevalt ei eksisteeri varasemast põhjapanevaid uuringuid roboti ega päris kala suuruse ja paiknemise olulisusest keeriseid tekitava objekti suhtes.

Traditsiooniliselt on olnud täpsete jõumõõtmiste jaoks vajalik mõõdetava objekti kinnitamine mõõtevahendi külge, see seab aga olulised piirangud komplekselt ujuvate robotite mõõtmisele ja ei võimalda teha katseid päris kaladega. Hüdrodünaamilisi jõudusid on võimalik arvutada ka kiirusvektoritest ja käesolev väitekiri tutvustabki uudset meetodikat sellise kaudse jõumõõtmise täiustamiseks. Kasutades signaalitöötluse valdkonnas tuntavaid lineaarseid ülekandefunktsioone suutsime me jõudude arvutamisel tekkivaid vigu vähendada kuni 83%. Seda meetodit kasutades on seega võimalik kaudselt mõõta kalarobotite ja ka päris kalade poolt tekitatavaid jõude ja ka neile mõjuvaid jõude kiirelt ja täpselt.

Hetkel puuduvad välitöödel kasutatavad mõõtevahendid, millega saaks iseloomustada keerukaid looduses esinevaid veevoolutingimusi. Käesolev väitekiri tutvustab uudset bioloogist inspireeritud mõõteseadet – küljejoone andurit, mis on mõeldud jõgedes ja kalapääsudes esinevate komplekssete veevoolude mõõtmiseks sarnaselt sellele, kuidas tunnetavad veevoolu päris kalad. Testides seda seadet mitmetes voolutunnelites ja ka päris kalapääsudes

näitasime, et on võimalik taasesitada kalakujulist vahendit ümbritsev kiiruse ja rõhuväärtuste väli ning leitud kiiruste väärtused on võrreldavad kommertsiaalsete ADV ja LDA süsteemidega.

Saadud tulemusi katsetest erinevate kalarobotite asetuste ja suurustega turbulentses voolus saab edaspidi kasutada projekteerimaks energiasäästlikumaid allveeroboteid vooluveekogude ning muude keeruliste veekeskondade uurimiseks. Küljejoone andurit ennast võib kasutada iseseisva seadmena, samuti võib selle integreerida allveerobotitega, võimaldades robotitel hinnata veekeskonda nende ümber ning sooritada teadlastele vajalikke mõõtmisi. Pikaajalisem eesmärk on siin kirjeldatud tehnoloogiaid edasi arendada ning kasutada neid kalapääsude hindamisel, võimaldamaks uusi teadmisi, mille abil saaks luua paremaid kalapääse ja seega taastada kalade migratsiooni.

## **ACKNOWLEDGEMENTS**

I would like to express my sincere gratitude to my supervisor Professor Maarja Kruusmaa. Her guidance, support, criticism and knowledge made this work possible.

I want to thank Dr. Jeffrey A. Tuhtan, Dr. Lily D. Chambers and Dr. Otar Akanyeti for their support and all of my colleagues from the Centre for Biorobotics for providing all kind of support.

Financially the research presented in this thesis was funded by the FILOSE project, supported by the European Union seventh framework programme (FP7-ICT-2007-3); and by the FISHVIEW project funded from BONUS, the joint Baltic Sea research and development programme (Art 185), funded jointly by the European Union's Seventh Programme for research, technological development and demonstration, and by the Academy of Finland (under the grant 280715), the German Federal Ministry for Education and Research (BMBF FKZ:03F0687A), and the Estonian Environmental Investment Centre (KIK P.7254 C.3255). My studies have also been supported by the Archimedes Foundation.

Finally I want to thank my family and friends for their encouragement and support to finish my doctoral studies.

## LIST OF PUBLICATIONS

The work of this thesis is based on the following publications. All publications are reprinted in the Appendix of this thesis.

- A G. Toming, T. Salumae, A. Ristolainen, F. Visentin, O. Akanyeti, and M. Kruusmaa, “Fluid dynamics experiments with a passive robot in regular turbulence,” in *Conference Proceedings – Robotics and Biomimetics (ROBIO 2012)*, pp. 532–537, 2012.
- B G. Toming, L. D. Chambers, and M. Kruusmaa, “Experimental study of hydrodynamic forces acting on artificial fish in a von Kármán vortex street,” *Underw. Technol.*, vol. 32, no. 2, pp. 81–91, 2014.
- C J. A. Tuhtan, G. Toming, T. Ruuben, and M. Kruusmaa, “A method to improve instationary force error estimates for undulatory swimmers,” *Underw. Technol.*, vol. 33, no. 3, pp. 141–151, 2016.
- D J. A. Tuhtan, J. F. Fuentes-Pérez, N. Strokina, G. Toming, M. Musall, M. Noack, J. K. Kämäräinen, and M. Kruusmaa, “Design and application of a fish-shaped lateral line probe for flow measurement”, *Review of Scientific Instruments*, vol. 87, no. 045110, pp.1–8, 2016.

## **AUTHOR'S CONTRIBUTION TO THE PUBLICATIONS**

Contribution to the papers in this thesis are:

- A Contributed by planning and conducting the force measurement experiments. Constructed the low cost PIV system. Planned and conducted PIV experiments and processed PIV data. Contributed by writing the paper.
  
- B Contributed by defining the research problem. Manufactured all prototypes. Planned and conducted experiments along with necessary software development. Developed methodology and processed and analyzed PIV and force measurements data accordingly. Wrote the paper.
  
- C Contributed by defining the problem. Developed force plate control software with PIV synchronization. Designed and conducted experiments. Processed PIV data and contributed to writing the paper.
  
- D Contributed in the novel sensor system design. Designed the experiments in a model fish pass and participated in lab and field experiments. Contributed to writing the paper.

## OTHER RELATED PUBLICATIONS

The following papers are published in similar fields but do not form the main part of the thesis.

On biomimetic underwater robots design and testing:

1. M. Kruusmaa, et al. (21 authors), “FILOSE for Svenning: A Flow Sensing Bioinspired Robot”, in *IEEE Robotics and Automation Magazine*, 21 (3), 2014, pp. 51–62.
2. T. Salumäe, R. Raag, J. Rebane, A. Ernits, G. Toming, M. Ratas, and M. Kruusmaa, “Design principle of a biomimetic underwater robot U-CAT” in Conference Proceedings – *IEEE OCEANS*, St. Johns, Newfoundland, Canada; 14-19 September 2014, pp. 1–5.
3. H. El Daou, T. Salumae, G. Toming, and M. Kruusmaa, “A Bio-inspired Compliant Robotic Fish: Design and Experiments”, in Conference Proceedings – *IEEE International Conference on Robotics and Automation (ICRA)*, May 14-19, 2012, pp. 5340–5345.
4. M. Kruusmaa, T. Salumäe, G. Toming, J. Ježov, and A. Ernits, “Swimming Speed Control and on-board Flow Sensing of an Artificial Trout”, in Conference Proceedings – *Int. Conf. of Robotics and Automation (IEEE ICRA)*, Shanghai, China, May 9-13, 2011: Int. Conf. of Robotics and Automation (IEEE ICRA 2011), Shanghai, China, 9-13 May, 2011, pp. 1791–1796.
5. H. EL Daou, T. Salumae, A. Ristolainen, G. Toming, M. Listak, and M. Kruusmaa, “A Bio-mimetic Design and Control of a Fish-like Robot using Compliant Structures”, in Conference Proceedings – *The 15th International Conference on Advanced Robotics (IEEE ICAR)*, Tallinn, June 20-23, 2011, pp. 563–568.
6. H. EL Daou, T. Salumae, A. Ristolainen, G. Toming, M. Listak, and M. Kruusmaa, “A bio-mimetic design of a fish-like robot with compliant tail”, in *International Workshop on Bio-Inspired Robots*, Nantes, France, 6-8 April, 2011.
7. G. Toming, “TTÜ juhtimisel luuakse robotkala”, *Keskkonnatehnika*, 5, 2011, pp. 8–9.

8. O. Akanyeti, A. Ernits, C. Fiazza, G. Toming, G. Kulikovskis, M. Listak, R. Raag, T. Salumäe, P. Fiorini, and M. Kruusmaa, “Myometry-Driven Compliant-Body Design for Underwater Propulsion” in *Conference Proceedings – IEEE International Conference on Robotics and Automation (ICRA)*, Anchorage, Alaska, 3 - 8 May, 2010, pp. 84–89.

On lateral line sensing and flow classification:

9. K. Chen, J. A. Tuhtan, J. F. Fuentes-Perez, G. Toming, M. Musall, N. Strokina, J.-K. Kämäräinen and M. Kruusmaa, “Estimation of Flow Turbulence Metrics with a Lateral Line Probe and Regression”, in *IEEE Transactions on Instrumentation and Measurement*, Forthcoming 2016.
10. J. A. Tuhtan, J. F. Fuentes-Perez, G. Toming and M. Kruusmaa, Flow Velocity Estimation Using a Fish-Shaped Lateral Line Probe with Product-Moment Correlation Features and a Neural Network, in *Flow Measurement and Instrumentation*, Forthcoming 2016.
11. N. Muhammad, G. Toming, J. A. Tuhtan, M. Musall, and M. Kruusmaa, “Underwater map-based localization using flow features,” in *Autonomous Robots*, pp. 1–20, 2016.
12. J. A. Tuhtan, J. F. Fuentes-Perez, G. Toming, M. Kruusmaa, N. Muhammad, N. Strokina, J. K. Kämäräinen, M. Musall, R. Carbonell-Baeza; M. Noack, and M. Schletterer, “Ecohydraulic flow sensing and classification using a lateral line probe,” in *11th International Symposium on Ecohydraulics*, Melbourne, Australia, 2016.
13. J. A. Tuhtan, N. Strokina, G. Toming, N. Muhammad, M. Kruusmaa, and J. K. Kämäräinen, “Hydrodynamic Classification of Natural Flows using an Artificial Lateral Line and Frequency Domain Features”, in *E-proceedings of the 36th IAHR World Congress: International Association of Hydraulic Research (IAHR) World Congress*, 28 June - 3 July, The Hague, Netherlands, 2015, IAHR, 1–8.
14. J. F. Fuentes-Pérez, J. A. Tuhtan, R. Carbonell-Baeza, M. Musall, G. Toming, N. Muhammad, and M. Kruusmaa, “Current velocity estimation using a lateral line probe”, in *Ecological Engineering*, 85, pp. 296–300, 2015.

15. N. Muhammad, N. Strokina, G. Toming, J. A. Tuhtan, J. K. Kämäräinen, and M. Kruusmaa, “Flow feature extraction for underwater robot localization: preliminary results”, in *Conference Proceedings - IEEE International Conference on Robotics and Automation (ICRA)*, May 26-30, 2015, Seattle, Washington, pp. 1125–1130.
16. J. A. Tuhtan, N. Strokina, G. Toming, N. Muhammad, M. Kruusmaa, and J. K. Kämäräinen, “Hydrodynamic classification of natural flows using an artificial lateral line”, in *26th Sachverständigen-Kuratorium (SVK) Fischereitagung*, 02-03 March, 2015, Fulda, Germany.
17. J. A. Tuhtan, M. Kruusmaa, M. Schneider, G. Toming, and I. Kopecki, “FishView: Developing a Hydrodynamic Imaging System Using a Robot Fish with an Artificial Lateral Line”, in *10th International Symposium on Ecohydraulics*, Trondheim, Norway, 2014, pp. 1-4.
18. R. Venturelli, O. Akanyeti, F. Visentin, J. Ježov, L. D. Chambers, G. Toming, J. Brown, M. Kruusmaa, W. Megill, and P. Fiorini, “Hydrodynamic pressure sensing with an artificial lateral line in steady and unsteady flows”, in *Bioinspiration & Biomimetics*, vol. 7, no. 3, 2012, pp. 036004:1-12.

On the development of field particle image velocimetry:

19. P. Thumser, C. Haas, J. A. Tuhtan, M. Schneider, G. Toming, and M. Kruusmaa, “RAPTOR: Real-time particle tracking in rivers”, in *11th International Symposium on Ecohydraulics*, Melbourne, Australia, 2016.
20. A. Erm, F. Buschmann, M. Listak, J. Rebane, and G. Toming, “Underwater Experiments and a Theoretical Model – Case Study in Tallinn Bay” in *Journal of Coastal Research*, SI65 (1), 2013, pp. 1521–1526.
21. F. Buschmann, A. Erm, M. Listak, J. Rebane, and G. Toming, “Autonomous Underwater Device for 2D Particle Image Velocimetry Field Analysis”, in *BSSC 9th Baltic Sea Science Congress 2013: New Horizons for Baltic Sea Science*, Klaipeda, Lithuania, 26-30 August, 2013, pp. 147.
22. A. Erm, M. Listak, J. Rebane, G. Toming, and F. Buschmann, “Autonomous PIV-measurements in the Tallinn Bay”, in *ICS2013 International Coastal Symposium: Book of Abstracts*, Plymouth University, 8-12 April, 2013, pp. 376.

23. F. Buschmann, A. Erm, V. Alari, M. Listak, J. Rebane, and G. Toming, “Monitoring sediment transport in the coastal zone of Tallinn Bay”, in Symposium Proceedings – *Baltic International Symposium (BALTIC), 2012 IEEE/OES*, Kalipeda, Lithuania, 8-11 May, 2012, pp. 1–13.
24. A. Erm, F. Buschmann, V. Alari, K. Kask, M. Listak, J. Rebane, and G. Toming, “Near bottom sediment transport in some possible wind farm locations in the Estonian coastal sea”, in *Geological Survey of Finland, Guide 57 (Abstract Book): 11th Colloquium on Baltic Sea Marine Geology*, Helsinki, Finland 19–21 Sept., 2012, pp. 15–16.

## INTRODUCTION

Fish have developed highly evolved sensory [1]–[4] and propulsion systems [5], tailoring them for over more than 200 million years to a wide variety of aquatic environments. Their superior swimming capabilities include high speed escape swimming and excellent maneuverability. Concurrently, they achieve highly efficient locomotion, enabling some species to travel more than 5000 km migration routes, some even going long periods without feeding [6]–[8]. In the epoch of the Anthropocene, their habitats have been eliminated or degraded, blocking previous natural migration to enable the transport of goods, hydropower generation and water supply. The current trend is to preserve fish and their habitats which includes restoring their migration ways, often by building fish passes [9], [10]. Biorobotics is one possible approach to understanding fish sensing and locomotion abilities. The knowledge gained with this approach can improve the preservation of fish.

In recent years there has been a rapid development in the field of biorobotics. Underwater robots mimicking fish swimming e.g. [11]–[16] and sensing [17], [18] have been designed and built. However, due to the complexity of undulatory locomotion control the majority of prototypes require still water conditions. Some are capable of swimming subject to a steady flow. In general, fish robots are not capable of swimming in the majority of naturally occurring aquatic environments. Correspondingly, there is a lack of studies on the interaction between turbulent flows and underwater robots. At the same time, this knowledge can improve the design (e.g. dimensioning the body of robot and control in the flow) of underwater robots for different environments and purposes.

The main motivation of bioinspired research is to generate new knowledge by adapting modern technologies to existing biological analogs. Thus contemporary underwater robots are often tethered (remotely operated vehicles) via a cable for control and energy supply. Important topics in current underwater robotics are therefore addressing problems associated with data transmission, control and energy efficiency. Furthermore due to the complexities involved in fluid-body interactions, flow and associated turbulence is largely considered as a disturbance to be compensated for [19]. This stands in stark contrast to fish, which have developed advanced sensing and propulsion capabilities which leverage turbulent flows as a source of energy and information [20]–[22]. Thus fishes should be seen as the “masters of their domain” and mimicking them is likely to aid both fundamental and applied applications relevant to underwater robotics. Our objective is to develop fish-like robots which can in turn be used by biologists to study fishes, their habitat, fish migration including passes, and even schooling behavior.

The focus of this thesis is the investigation of hydrodynamic forces affecting fish-shaped bodies subject to turbulent flow. First, the relation of forces and position of the body behind an obstacle generating turbulent wake is studied. Another key aspect is the determination of the body length scale and its influence on the near-

body hydrodynamics subject to a wake with periodical vorticity and known wavelength. In this thesis I show experimentally how the hydrodynamic forces affecting the fish robot change in the Kàrmàn vortex street (periodic pattern of vortices caused by the unsteady separation of flow around blunt bodies) depending on the lateral and longitudinal position of the fish robot and how they depend on the body size of the fish shaped object. This is followed by introducing a novel methodology to improve the accuracy of indirect force measurements making it possible to measure forces affecting or exerted by the freely swimming robot or real fish. This method fuses high-resolution particle image velocimetry data in conjunction with a filter function and signal processing to generate accurate instantaneous force estimates. Data are calculated from the velocity field and calibrated transfer functions between estimated and measured are used to significantly decrease the time-averaged error and eliminate the phase shift (time delay). Finally, a novel measurement system is introduced consisting of a fish shaped device for measuring fish passes and rivers from the “fish’s point of view”.

This thesis is divided into six main parts: in the first chapter I provide a short overview of fish swimming and migration including common problems induced by human activity. Following this, an overview of experimental hydrodynamics and methods is presented. Chapter 2 describes the facilities and equipment used for this work.

Chapter 3 and 4 give an overview of my research on hydrodynamic forces in a vortex street affecting differently positioned and sized fish shaped objects. This includes a full description of the investigations on force measurements and flow structures in turbulent flows, including an in-depth analysis and discussion of results. Chapter 5 introduces a novel methodology for improving indirect force measurements based on particle image velocimetry. And finally chapter 6 describes the validation of a fish shaped lateral line probe meant for measuring complex flows in fish passes, and results from the initial testing in real fish passes. Chapters 3, 4, 5 and 6 are based on four publications that are reprinted in Appendix.

## **CONTRIBUTION OF THE THESIS**

This thesis contributes to the development of underwater robotics and bioinspired flow sensing by:

- Experimentally determining relations between hydrodynamic forces and the robot's position behind an obstacle whose wake generates periodic vorticity.
- Providing critical relations relating the robotic body length scale to the vortex street wake wavelength, illustrating how the ratio of these scales influences the forces acting on the sensing body and showing how large robotic fish can energetically benefit from the impinging flow of a vortex street.
- Implementing and improving a novel indirect force measurement methodology, capable of providing robust and accurate instantaneous force calculations without the need to physically harness the robot (or a fish) to a force gauge.
- Introducing a novel, bioinspired flow measurement device for evaluating complex natural flows in river beds and manufactured fish pass structures.

# 1 BACKGROUND

There are over 25,000 species of fish living today and over 200 million years of evolution they have developed very efficient propulsive systems. Fish exhibit superior capabilities in swimming in complex and turbulent flows, many species even prefer turbulent regions to uniform flow regions due to the smaller energy expenditure. As this is contrary to state-of-the art human made devices there is still much to learn from fish. Fortunately there are new methods of experimental hydrodynamics available for studying and comparing real fish to human made robots. This includes both direct and indirect force measurements and whole field velocity measurements. This chapter gives an overview of fish swimming, their energy efficiency, human caused problems on fish migration, and experimental methods used in this thesis.

## 1.1. Fish locomotion

Fish have highly evolved swimming and sensory capabilities which are greatly affected by the physical properties of the surrounding fluid. Water has a high density as compared to air, and acts as an incompressible fluid meaning that any movement induced by an aquatic animal or underwater robot will set the surrounding medium in motion [23], [24]. Considering flow sensing, the opposite case also holds; fish can maintain position and let “flow information” travel at the speed of sound in water come to them. As water density is close to the density of fish, they are close to neutrally buoyant. Thus contrast to terrestrial organisms, fishes do not need to expend large amount of propulsive effort to overcome the pull of gravity. For this reason fish locomotion could be considered as “aquatic flight”, allowing them to focus their efforts onto the generation of forward thrust [5].

Most fish swim by pushing water back with the undulations of their body or fins [5]. There are many ways to classify fish swimming, divided into two main categories:

- Steady swimming – characterized by cyclically repeated propulsive movements, this mode is used when swimming at constant speed and by species that typically cover large areas;
- Unsteady swimming – characterized by rapid, non-periodic movements that typically last only a fraction of a second, unsteady movements are used for turning, escaping or catching prey.

Fish swimming can be also categorized into different modes according to types of propulsive movements used by fish. This was at first done in 1926 by Breder [25], it has been criticized and later improved but nevertheless Breder’s classification is still often used and cited as the basis. The extended version of this nomenclature [5] is shown in Figure 1.1.

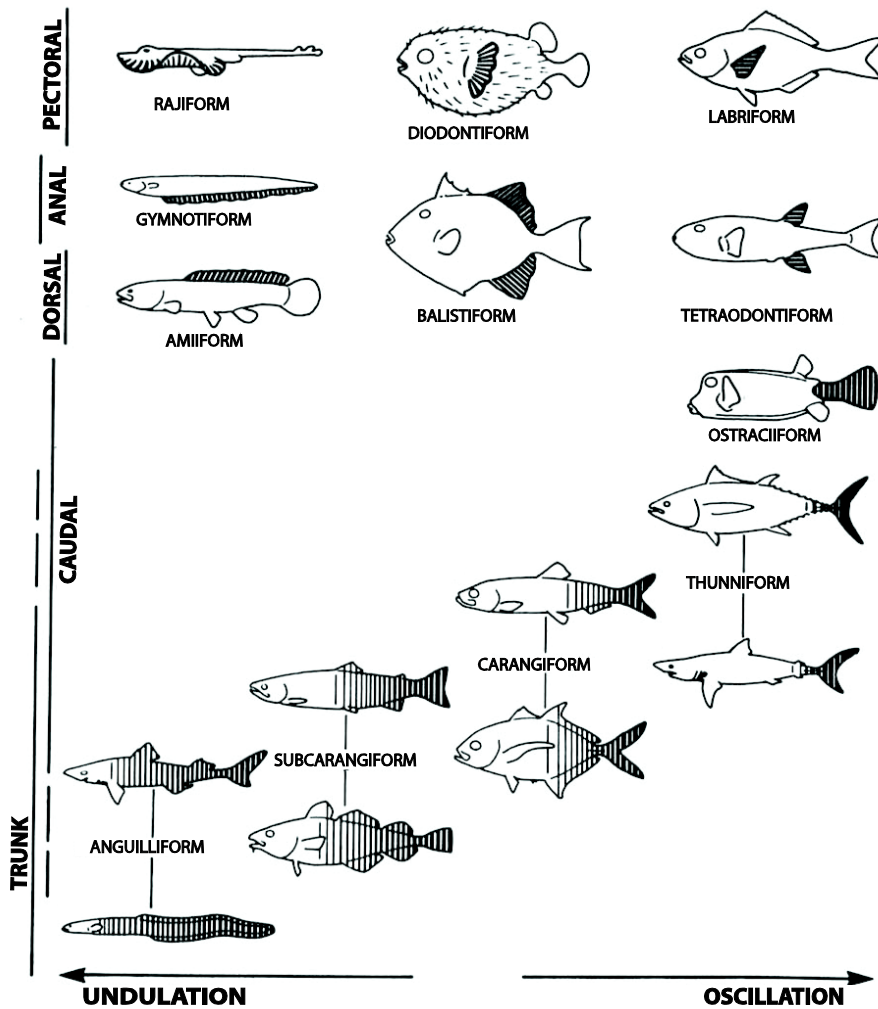


Figure 1.1 Forward swimming modes of fish. Fish are aligned along the vertical axis based on the propulsive contributions of body and fins, and along the horizontal axis according to swimming modes from undulatory to oscillatory. Reprinted from *Fish Physiology*, Vol. VII, C. C. Lindsey, *Form, Function and Locomotory Habits*, Pg. 9, Copyright 1978, with permission from Elsevier.

Most fish, especially those who swim long distances, generate thrust by bending their bodies to create a backward-moving propulsive wave that extends to its caudal fin. This kind of locomotion is classified as body and/or caudal fin (BCF) locomotion [24]. Some other species use different swimming mechanisms that involve using their median and pectoral fins, this is called median and/or paired fin (MPF) locomotion [5], [24]. Only about 15% of fish use MPF for forward

motion, mostly BCF is used for propulsion and MPF is used for stabilization and maneuvering purposes. This thesis focuses therefore on BCF swimming.

### 1.1.1. Physics of fish locomotion

A fish's body is affected by several different forces. In the vertical direction the forces acting on a body are weight, buoyancy and hydrodynamic lift. Drag and thrust affect the body in the horizontal direction. In order the fish to hold its position or swim steadily these forces must be in equilibrium. The drag force itself can be broken down into viscous drag (or friction drag) – friction between a fish body and the boundary layer of water; form drag (pressure drag) – pressure differences are formed when pushing water away so the fish can move forward; induced drag – energy lost in vortices created by fish body and fins; and gill resistance – some species ventilate their gills by swimming forward with open mouth, resulting in internal friction [26].

Viscous drag is calculated using the standard Newtonian equation

$$D_v = \frac{1}{2} C_f S U^2 \rho, \quad (1.1)$$

where  $D_v$  is viscous drag,  $C_f$  is a coefficient of frictional drag depending on the Reynolds number  $R_e$ ,  $S$  is the total wetted surface area,  $U$  is the swimming speed and  $\rho$  is the density of water [27].

Reynolds number – a ratio of inertial forces to viscous forces – can be calculated with the equation

$$R_e = \frac{Ul}{\nu}, \quad (1.2)$$

where  $R_e$  is the Reynolds number,  $U$  is the swimming speed,  $l$  is the body length of fish, and  $\nu$  is the kinematic viscosity of water (at 20°C  $\nu = 1.004 \times 10^{-6} \text{ m}^2\text{s}^{-1}$ ).

Frictional drag coefficients can be calculated separately for laminar and turbulent flow conditions with the following equations [26]

$$C_{f \text{ laminar}} = 1.33 R_e^{-\frac{1}{2}} \quad (1.3)$$

$$C_{f \text{ turbulent}} = 0.074 R_e^{-\frac{1}{5}} \quad (1.4)$$

The form drag can be included to the drag coefficient

$$C_D = C_f \left[ 1 + 1.5 \frac{d}{l} + 7 \left( \frac{d}{l} \right)^3 \right], \quad (1.5)$$

where  $C_D$  is the combined drag coefficient,  $C_f$  is a coefficient of frictional drag,  $d$  is the body thickness and  $l$  is the body length.

Induced drag can be calculated with the equation

$$D_i = \frac{2L^2}{\pi\epsilon U^2 b_p^2}, \quad (1.6)$$

where  $D_i$  is the induced drag,  $L$  is the required lift force,  $U$  is the speed of the fish,  $b_p$  is the span of the pectoral fins, and  $\epsilon$  is the efficiency factor.

The gill resistance depends directly on the swimming speed, ventilation volume and the density of water and can be calculated using the equation

$$R_G = \rho V_G U \left(1 - \sqrt{\frac{2\Delta H}{\rho U^2}}\right), \quad (1.7)$$

where  $R_G$  is the gill resistance,  $\rho$  is the density of water,  $U$  is the swimming speed of fish and  $\Delta H$  is the head loss (typically about 2000 dynes  $\text{cm}^{-2}$ ).

The total drag is a combination of the previously described components and is also greatly affected by propulsive movements, often these components cannot be isolated [28]. However Magnuson calculated these components for a sustained-swimming skipjack tuna and found that 53% of the total drag is from viscous and form drag, 30% is from induced drag and 17% from the gill resistance [26]. Form drag has been later studied experimentally using modern technology [29].

Thrust force propels the fish forward and it can be calculated using equation (1.8) proposed by Lighthill in 1970 [30]

$$F_T = \frac{1}{2} \rho S_c W_{rms}^2 C_T, \quad (1.8)$$

where  $F_T$  is a thrust force,  $\rho$  is the density of water,  $S_c$  area of caudal fin,  $W_{rms}$  is the lateral velocity of the caudal fin and  $C_T$  is a thrust coefficient.

Thrust can be directly related to rate of change of momentum in the volume surrounding the fish. When the planar distribution of the momentum flux entering and exiting the control volume is known and making assumptions that the incoming flow is planar and uniform with the zero lateral flow speed the thrust force can be calculated using a following equation

$$F = -\rho \int \frac{du}{dt} dV + \rho \int (u_3^2 - u_1^2) dz_1 + \int (p_3 - p_1) dz_1, \quad (1.9)$$

where  $F$  is streamwise force,  $\rho$  is density of fluid,  $u$  streamwise velocity,  $z_1$  is the vertical elevation with constant reference,  $p$  is pressure at boundaries and  $t$  is time. Control volume surfaces 1 and 3 are shown in the Figure 1.2.

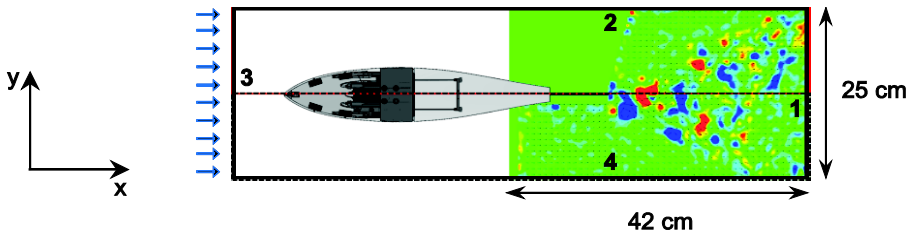


Figure 1.2 Placement of the control volume surfaces.

Steady swimming (time-averaged body velocity is constant) occurs when drag and thrust forces are equal. This requires periodical repetition of undulatory movement which can be approximated as a sinusoidal representation of body deflection as suggested in [31] by Videler

$$h(x, t) = A(x) \sin(kx - \omega t), \quad (1.10)$$

where  $h(x, t)$  is the swimming body's displacement as a function of space and time,  $A(x)$  is the amplitude envelope,  $k = \frac{2\pi}{\lambda}$  is the wave number and  $\omega$  is the tail beat frequency.

In 1958 Bainbridge studied trout (*Salmo irideus*), dace (*Leuciscus leuciscus*) and goldfish (*Carassius auratus*) and determined that relationship between the tailbeat frequency and swimming speed is linear, also in frequencies higher than 5 Hz swimming speed is directly dependent on the frequency and can be expressed with the following equation [32]

$$V = \frac{1}{4}[L(3f - 4)], \quad (1.11)$$

where  $V$  is the speed,  $L$  is the body length, and  $f$  is the frequency in tail beats per second.

Later this relationship has been also verified for other species such as the jack mackerel (*Trachurus symmetricus*) [33], largemouth bass (*Micropterus salmoides*) [34]. In 1984 Webb empirically determined the relationship (Equation 1.12) between swimming speed, tailbeat frequency and body length for rainbow trout (*Salmo gairdneri*) [35]

$$f = 3.19L^{-\frac{1}{3}} + 1.29\frac{V}{L}, \quad (1.12)$$

where  $f$  is the tailbeat frequency,  $L$  is the body length, and  $V$  is the swimming speed.

In general, the linear form has found to hold for all the species studied so far.

Even though fish swimming has been thoroughly studied [36]–[38], the exact physical mechanisms driving undulatory locomotion are still not fully understood. Mastering undulatory swimming is of interest in biorobotics since it is highly energy efficient (fish swimming efficiency can be up to 97% [39]) compared to man-made devices (propellers achieve only up to 70% of efficiency [40]).

### 1.1.2. Locomotion in turbulence

Fish locomotion in flowing and turbulent water is far beyond the current state-of-the-art. Studies [20], [22], [41], [42] show that fish, for example rainbow trout (*Oncorhynchus mykiss*) may even prefer turbulent conditions to uniform flow conditions when swimming upstream. In 2010 Przybilla investigated rainbow

trout swimming in the wake of a D-shaped cylinder. She found that there are four distinct zones near the cylinder where trout prefer to stay [43]: the bow wake zone in front of the object, two entraining zones on both side of the object, and the Kàrmàn vortex street behind the object.

The Kàrmàn vortex street (KVS) is a periodically repeating vorticity pattern that is caused by the unsteady separation of flow around blunt bodies (see Figure 1.3.) [44], [45]. This phenomenon is named after Hungarian-American physicist and engineer Theodore von Kàrmàn (1881 - 1963) [46]. KVS frequently appears in natural flows behind stones, branches, pillars and even islands. It is also very predictable, and can be repeated in laboratory conditions and is thus often used by fish biologists and roboticists [47], [48].

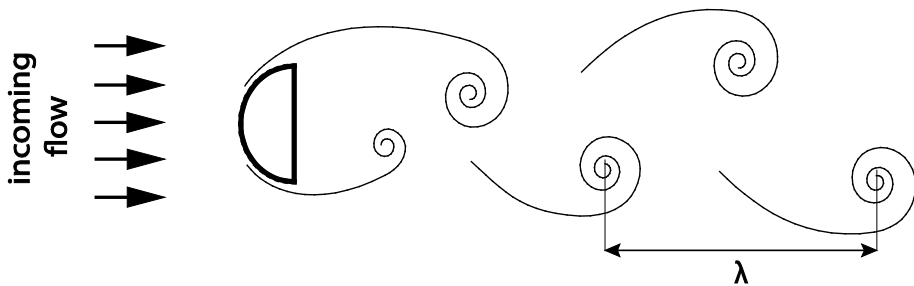


*Figure 1.3 Kàrmàn vortex street generated by the D-shaped cylinder.  $\lambda$  – is the wake wavelength.*

The interaction of some fish species and periodic vortices in KVS has been studied in [22], [42], [49]–[56]. It was found that trout alter their body kinematics when swimming in a KVS compared do swimming in uniform flow. This behavior is called Kàrmàn gaiting. Kàrmàn gaiting fish has larger body curvature, amplitude and lateral motion than those of a fish swimming at same speed in non-disturbed flow, the tail beat frequency however is lower and matches the vortex shedding frequency of the KVS [51].

Regardless of the altered body kinematics, with larger body amplitudes it is experimentally shown by measuring the oxygen consumption [53], [54] and muscle activity [52], [57] that trout uses less energy when Kàrmàn gaiting compared to swimming in the uniform flow with the same speed. In 2006 Beal showed that even a dead trout can swim upstream when placed into a KVS [58]. These studies suggest that fish can gain advantage from environmental forces and hold station or even move upstream passively. Similar, supporting studies have been also made with artificial devices like hydrofoils [59]–[61] and flexible filaments [62] and as well with fish robots [48], where it is shown that when interacting properly with oncoming vortices, a substantial increase in efficiency can be gained. This stands in stark contrast to traditional underwater vehicles where the turbulence and oncoming vortices are often the source for instability and lower propulsive performance [19].

In Nature, flowing waters are almost always turbulent especially in areas where fish prefer to habitate. Objects causing turbulence e.g. stones, branches, uneven bottom surfaces, etc. often offer places to hide, rest, feed or reproduce. Fish migration takes place largely in turbulent flows. Thus to further the state of the art in biorobotic propulsion and to improve our knowledge of undulatory locomotion, more studies in natural turbulent environments are needed.

## 1.2. Fish migration

Energy efficient swimming techniques are especially relevant in the context of fish migration as some fish species need to swim thousands of kilometers without feeding. Therefore, studying migration ways can give new information for building efficient bioinspired underwater robots. Applying bio-inspired technology also helps to gain more knowledge on how to design and build artificial fish passes in natural migration paths.

One way of defining migration is the following; migration requires that individuals, populations or parts of populations move between two defined habitats on a temporally predictable basis with regular periodicity [63]–[65]. There are many ways to categorize migration, one is by function: spawning migration, seasonal refuge from climate on predators and feeding migration. The second way is to classify by habitat: oceanodromy – migrations happening entirely at sea; potamodromy – migrations happening entirely in fresh water; diadromy – migrations occurring between freshwater and marine environments [65]. Diadromy in turn has two subgroups: anadromy – migrating from freshwater to marine habitats, e.g. salmonids, who as juveniles migrate to sea, and return to spawn into exactly the same rivers or streams where they were born [63], [66]; and catadromy – migration from marine to freshwater environments, e.g. the European eel (*Anguilla anguilla*) who migrates from the Sargasso Sea to spend its adult life in the rivers and lakes of Europe and in the end of its life cycle returns to its natal habitat to reproduce and die [63], [7]. In addition a smaller scale migration exists e.g. vertically [67] and between offshore and littoral zone [68].

Salmonoids are migrating fish that spawn in a cold and well-oxygenated stream waters on gravel and stone bottoms with different flow speeds and size of the stones in redds, depending on the size and species of fish [64], [69]. The route to the spawning area can be more than 1000 km long, containing a diverse set of aquatic environments. In rivers, calm areas alternate with faster flowing regions and rapids with high flow speed and turbulence. During these long and complex migration journeys fish often do not feed so they must be extremely energy efficient. While salmonoids are considered very efficient swimmers [6], there are even more efficient species. European eel for example is considered to be 4 – 5 times more efficient swimmer, as their migration distance can be 5000 – 6000 km long [7], [8].

Efficient energetics and timing have key roles in migration since anadromous fish do not feed during the migration and many fish die after spawning, meaning they have only one chance to reproduce [70]–[72]. Studies of migration energetics are based on two approaches, in the first one the energy usage is estimated by collecting fish samples from different regions in river, killing them and then measuring energy contents of tissues [70], [73], [74]; in the other group, EMG electrodes are placed into fish muscles and radio transmitters are placed into or under the fish belly, fish swimming activity and speed is obtained from the radio signals [72], [75]–[78].

Migration of salmonoids is widely studied, Atlantic (*Salmo salar*) and Pacific salmon (*Oncorhynchus* spp.) are excellent examples of energy conservation and usage. The energy cost of migration and spawning for these species is about 60% of their total somatic energy and about 75% - 82% respectively [65], [70]. Energy consumption during migration depends also on the obstacles, temperature and discharge of the river [72], [79], [80]. EMG studies show that high riverbed gradients, highly turbulent sections and areas with fast flow are difficult to pass and require high energy expenditure. However fish tend to swim faster in these areas thus spend less time struggling to difficulties and have relatively low energy expenditure [76].

In addition in 2000 Hinch and Rand discovered that at some sites the migration speed of some fish exceeded their known maximal swimming speeds [81]. They proposed that salmon can exploit flow structures such as vortices with reverse flow. This is also supported by studies of Makiguchi et al. who showed that chum and pink salmon tend to swim near river banks and near the bottom where the water flow is smaller and more objects are found that could create complex flow structures [78].

### **1.2.1. Problems of migration**

Rivers are not only home for fish and other aquatic animals but they have also been widely used by humans for transportation and to power hydroelectric power plants – these unfortunately block the natural migration ways [10]. Today, the restoration of rivers' longitudinal connectivity is a sociopolitical goal [9]. The most common way to do this is to build fish passes (also known as fish ladders or fishways) structures around artificial (sometimes also around natural) barriers to facilitate fish migration.

Constructing fish passes is a not trivial task as parameters that affect the efficiency of a fishway are water velocity, discharge, gradient, turbidity, attraction flow, temperature, lightning, design of the bottom, the exact location of it, the size and swimming capabilities of the fish that the fishway is designed for, etc. [9], [82], [83]. In general, fish passes can be divided into two main groups; some seek to emulate nature, others are constructed in a purely technical way. The first group includes natural looking bypass channels and fish ramps [9],

[84], [85]. Common technical fishways are eel ladders [9], pool-type passes [86], [87], vertical slot fish passes [83], [88]–[90], Denil fish passes [91]–[93] and fish lifts [9], [93].

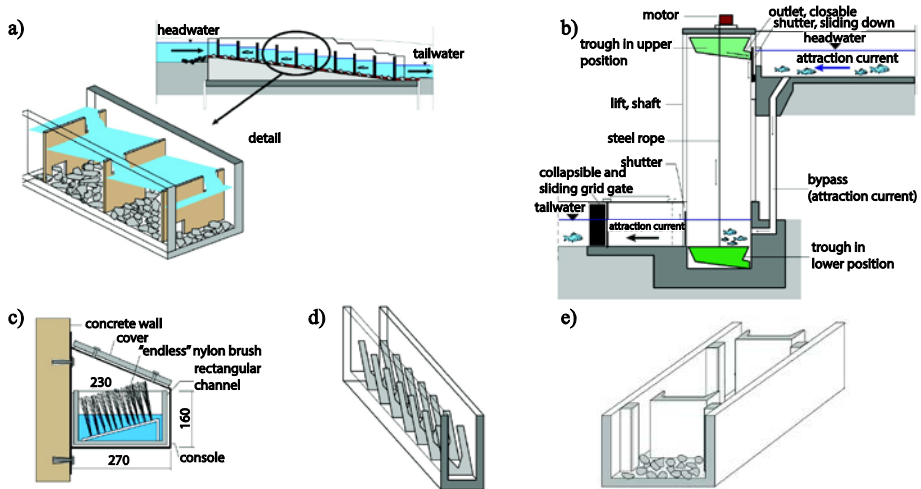


Figure 1.4 Common types of technical fish passes: a) Pool-type fish pass, b) fish lift, c) eel ladder, d) Denil fish pass, e) vertical slot fishway, with two slots. Adopted from [9].

Once constructed it remains necessary to monitor fish passage structures to evaluate their efficiency. This is done by counting the number of fish entering the fish pass (attractiveness) and compare this to the actual number that successfully exit the fish pass (passability). Several methods are commonly applied; catching, counting and releasing all fish at the entrance, inside the fish pass and after the exit; tagging fish with dye or electronic transmitters and finally automatic devices including movement sensors and cameras [9], [85], [94]–[97].

### 1.3 Experimental fluid dynamics

A fluid can be defined as a substance that continuously deforms under an applied shear stress. Life would not exist without fluids (e.g. air and water) and without the specific properties that they have. The most important properties of fluids are [98]: density, pressure, viscosity, surface tension, thermal conductivity and diffusivity. Fluids are widely studied both in science and engineering and three main approaches exist:

- Theoretical (analytical);
- Computational (CFD);
- Experimental.

Experimental fluid dynamics can be divided into four large groups (that in some cases overlap) based on the principles used:

- Pressure measurements;
- Velocity measurements;
- Flow visualization;
- Force measurements.

In this thesis the experimental approach including velocity and pressure measurements is used. Experimental methods were chosen since they give most accurate results and prototypes of fish-shaped robots and sensor systems are available in the laboratory from previous and ongoing research projects.

### 1.3.1. Pressure and velocity

**Pressure** is mostly measured at walls or in the freestream. Measurements at walls are usually conducted using small taps installed flush to the wall, and transducers are then connected. Measuring the freestream pressure is more complicated, and the common way is to use static pressure tubes. In both cases, in order to achieve satisfactory sensitivity, it is important to choose the suitable transducer, construct and place the measurement device in the way that the flow is disturbed as little as possible [99]. In recent years also pressure sensitive paint is used in wind tunnels. This method allows to measure pressure directly on the surface of a model without using any transducers, tapings or tubes. The paint changes its luminescence depending on the air pressure and is used to cover the model. With proper illumination and imaging systems, the image shows the direct pressure distribution over the model [99].

There are numerous ways to measure **velocity** in fluids [100]–[103]. Commonly used methods can be divided into 2 main groups whether they are intrusive (pressure based approaches utilizing the Bernoulli equation, hot wire anemometry, propeller anemometry and ADV – acoustic Doppler velocimetry ) or non-intrusive (LDV – laser Doppler velocimetry, PIV – particle image velocimetry, MTV – molecular tagging velocimetry). Another option is to measure point-wise (pressure based techniques, hot wire anemometry, propeller anemometry, ADV, LDV), portions of the field can also be recovered using PIV, MTV, and DGV (Doppler global velocimetry).

The main method used for the work in this thesis is PIV. The principles of PIV are summarized in Chapter 1.4. ADV and LDV are also used in this thesis to provide ground truth data when testing a new prototype. All three methods require particles in the flow. ADV and LDV are based on the Doppler shift. ADV probe sends out an acoustic impulse and uses three receivers to detect the reflected signal enabling 3D flow measurements with sampling rate generally below 50 Hz. More details about ADV can be found in [104]. LDV uses laser light instead of sound waves, typically one laser beam is split into two beams which are then

crossed in the flow where they interfere and create fringes. Particles moving through that spot reflect the light that is collected and velocities are calculated based on the change of wavelength of the reflected light. By combining lasers with different wavelengths 2D and 3D flow measurements are possible, typical sampling rate is in MHz range and for commercial solutions can reach up to 800 MHz [105]. More details of LDV can be found in [100].

Velocities in steady mid to high velocity flows are often estimated from pressure measurements. Pressure and velocity in incompressible fluids can be related using the Bernoulli equation [100]

$$p_0 - p = \frac{1}{2} \rho U^2, \quad (1.13)$$

Where  $p_0$  is pressure at the stagnation point,  $p$  is a free stream static pressure,  $\rho$  is the local density of fluid and  $U$  is mean local velocity along the streamline.

### 1.3.2. Force measurements

In fluid dynamics, especially in aerodynamics the measurement of forces in wind tunnels is one of the main tasks. In hydrodynamics the force measurements are less common but are still used. Historically the force measurement instruments were mechanical and they resembled balances for weighing. Today's systems are based on transducers but the name balance is still used. Balances can be distinguished by their location – inside or outside of the object; and by number of force components it is able to measure – one to six components.

Forces on the object are detected by measuring the strain on a deforming body, the strain can be caused by bending, shear or tensile stress. Load cells (cantilever beams, parallelogram-types and torque transducers) based on the measurement of bending stress are most commonly used. Cell types can however vary. These types of load cells are able to measure only one force component (both positive and negative direction). To measure more components it is necessary to combine multiple load cells.

Force measurements are useful in robotics, biorobotics and in studying fish. Force measurements systems can be placed both outside of the water [58], [59], [106]–[112] and underwater [113]–[115].

### 1.4. Particle image velocimetry

PIV is the mainly used experimental method in this thesis. 2D PIV was chosen for velocity measurements because of its following properties – it is non-intrusive 2D whole field method with high sampling frequency and accuracy, thus enabling reliable velocity measurements simultaneously in the free stream flow as well as in the vicinity and on the boundaries of an object.

The motion of common fluids like water and air is not visible to the human eye or to cameras as these liquids are transparent and homogeneous. Some options to visualize the flow is to seed it with particles, dye, smoke or small bubbles [116]. The motion of these tracer particles is visible to imaging devices and humans, making it possible to measure the flow speed and direction. The principle of PIV is based on calculating these quantities from the displacement of particle images [117]. Although observations of water flow using particles date back hundreds or even thousands of years, the term PIV first appeared in scientific literature in 1984 [118]. PIV is a non-intrusive, indirect whole field measurement technique [119]. The measurement system typically consists of the following sub-systems: lighting systems, imaging devices, recording or data storage devices, synchronization systems and data processing systems. Since 1984 the techniques used have changed and evolved together with development of computers, cameras and other electronics but the principle (see Figure 1.5) stays the same.

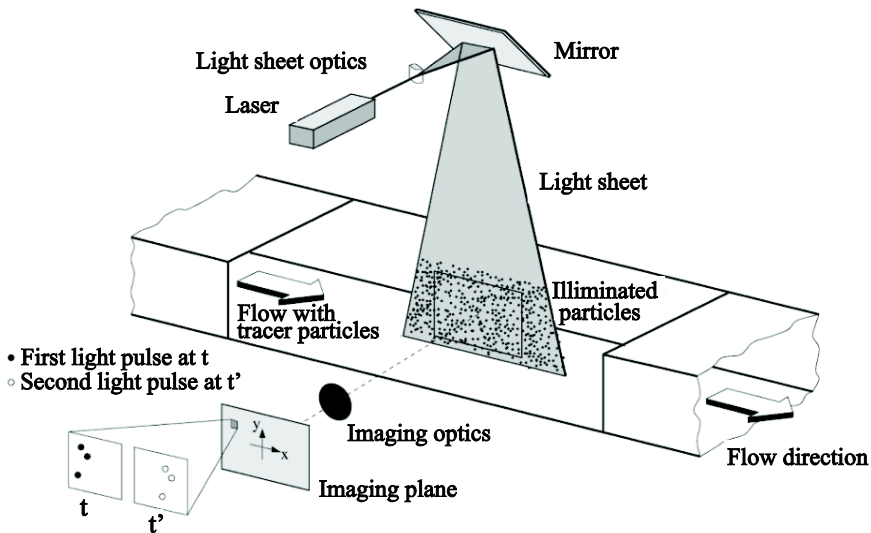


Figure 1.5 Experimental arrangement for particle image velocimetry in a wind tunnel. Reprinted from *Particle Image Velocimetry A Practical Guide, Second Edition*, 2007, Pg. 4, M. Raffel, © Springer-Verlag Berlin Heidelberg 1998 2007, With permission of Springer.

#### 1.4.1. Light sources and light sheet optics

Generally for PIV setups light sources with monochromatic and coherent light are preferred since these properties allow the usage of optical bypass filters with very specific wavelengths and form a distinct light sheet or volume with simple optical lenses. PIV systems can be said to rely on coding the light in time, it can be done by using pulsed light sources, a shutter in front of the light source or imaging device may be also used. The energy of the pulses has to be sufficient

for the imaging device to be able to capture the reflections from small particles [120]. Lasers fulfill all of these requirements. Historically, double pulsed ruby lasers, excimer lasers, Cu vapor lasers and cavity dumped Argon ion lasers have been used [120]. The first use of the double-pulsed solid-state laser in PIV is documented in 1986. Later on, when solid-state lasers especially Nd:YAG (neodymium-doped yttrium aluminum garnet;  $\text{Nd:Y}_3\text{Al}_5\text{O}_{12}$ ) evolved, became smaller and started to have self-cooled power supplies, they became the most used light sources in this field [118], [121]. In addition to lasers also xenon flash lamps, halogen lamps and arc lamps [120], [122]; LEDs [123] and LCD projectors [124] have been used. Recently, due to the rapid development of semiconductor lasers (diode lasers), smaller, cheaper and easily movable coherent light sources have become available [117].

The first task in forming a light sheet is to get the light from the laser to the experimental area. There are three options: using an optical fiber between the laser and the light sheet optics [125], using mirrors to guide the laser beam, and finally to place the laser directly near the experimental area. PIV measurement relies on the assumption that illuminated particles lay on a thin light sheet, so it is possible to focus the camera only on that layer of particles [117]. It is thus required that the thickness of the light sheet is significantly smaller (about 1%) than its width and height [100]. The laser beam is highly collimated and to form a light sheet it only requires de-collimation in one dimension, usually with the help of a cylindrical lens [126]. Typical laser irradiance profile is characterized by equation

$$\frac{I}{I_0} = \frac{2}{\pi\omega^2} \exp\left(\frac{-2r^2}{\omega^2}\right), \quad (1.14)$$

where  $I$  is radiant intensity,  $I_0$  is peak intensity,  $\omega$  is the beam waist and  $r$  is radius of a beam.

Over 99% of the energy is located in the circle with a radius of  $1.5\omega$  while at the waist it is only 13.5%. According to Snell's law the incident and refracted light rays are related with the following equation

$$n' \sin \theta_i = \sin \theta_r, \quad (1.15)$$

where  $n'$  is real part of complex refractive index,  $\theta_i$  is incident angle and  $\theta_r$  is refraction angle.

Since  $\sin \theta_i = \frac{y}{r_c}$ , the Equation (1.15) can be rewritten as

$$\theta_r = \sin^{-1} \frac{n'y}{r_c}, \quad (1.16)$$

where  $y$  Cartesian coordinate is and  $r_c$  is radius of a cylindrical lens.

The fan angle is expressed as

$$\theta_f = \sin^{-1} \frac{n'y}{r_c} - \sin^{-1} \frac{y}{r_c} \quad (1.17)$$

Considering that the typical value of  $\omega$  is 0.4 mm, 99% of energy will fall in

$y = 1.5\omega = 1.5 \times 0.4 \text{ mm} = 0.6 \text{ mm}$ . Now supposing the refractive index of glass is  $n' = 1.55$  and using Equation (1.17), we obtain  $\theta_f$  values of  $1.9^\circ$ ,  $3.8^\circ$  and  $31.6^\circ$  for the cylinder diameters of 10 mm, 5 mm and 1 mm, respectively [126]. It is possible to avoid extremely small diameters by combining multiple lenses in series so that every following lens amplifies the divergence.

Nevertheless, simplest systems utilize only a single cylindrical rod or lens [127], or a condenser lens in the case of volumetric PIV [123]. More sophisticated systems use a combination of many spherical and cylindrical lenses, making it possible to change the width and thickness of the light sheet [117].

### 1.4.2. Tracer particles

Tracer particles can be added to the flow or in some situations they are naturally present. Ideally, particles should exactly follow the flow without affecting it and without affecting each other. The other key requirement is that the particles must have good light scattering qualities [128]. In most cases it is also important that particles are non-toxic, chemically inert and non-abrasive [129]. In practice particles with nearly ideal properties can be found by commercial suppliers.

One of the main error sources in PIV experiments is the influence of gravitational forces if the densities of fluid and tracer particles do not match [117]. The motion of particles is often modeled using the Stokes' drag law, with the assumptions that particles are spherical and the Reynolds number is very small [117], [130]. Using the described assumptions the velocity of a particle induced by gravity can be described with a following formula [117]

$$U_g = d_p^2 \frac{(\rho_p - \rho_f)}{18\mu} g, \quad (1.18)$$

where  $U_g$  is the gravitationally induced velocity,  $d_p$  is the diameter of a particle,  $\rho_p$  is the density of a particle,  $\rho_f$  is the density of a fluid,  $\mu$  is the dynamic viscosity of a fluid and  $g$  is acceleration due to gravity.

The estimate of a velocity lag of a particle in a continuously accelerating fluid can be derived similarly [117]

$$U_l = U_p - U_f = d_p^2 \frac{(\rho_p - \rho_f)}{18\mu} a, \quad (1.19)$$

where,  $U_l$  is the velocity lag between the fluid and a particle,  $U_p$  is the velocity of a particle,  $U_f$  is fluid velocity and  $a$  is the local acceleration vector of a fluid.

In practice, especially in case of liquid flows the calculation of  $U_g$  and  $U_l$  can be neglected as it is possible to choose matching particles for the fluid.

The light scattering efficiency is determined by the difference in index of refraction for the fluid and the particles. This difference for liquids and solid is quite small, so relatively large particles of about  $10\ \mu\text{m}$  are needed. Smaller particles may not reflect a sufficient amount of light and larger sizes may affect the flow itself. The dynamics of turbulent flows can be altered when the diameter of particles is comparable with the Kolmogorov length scale, in laboratory-type flows this determined to be about  $100\ \mu\text{m}$  [128]. Thus in laboratory scale liquid flows the tracer particle sizes are mostly between  $\sim 10\ \mu\text{m}$  and  $100\ \mu\text{m}$  [129], and in the studies of micro scale flows between  $200\ \text{nm}$  and  $2\ \mu\text{m}$  [131].

In case of spherical particles with the diameter larger than the wavelength of the incident light, the light scattering can be described with Mie's scattering theory. The Mie scattering is characterized by the normalized diameter [117]

$$q = \frac{\pi d_p}{\lambda}, \quad (1.20)$$

where,  $q$  is the normalized diameter,  $d_p$  is the diameter of a spherical particle and  $\lambda$  is the wavelength of the incident light.

According to Mie's theory when increasing the  $q$ , the ratio of forward to backward scattering intensity increases rapidly (see Figure 1.6). Thus the most efficient method to record is forward scatter [117]. However, in practice the camera is most commonly positioned perpendicularly to the light sheet, due to the limited depth of field. A thorough description of light scattering from different particles is given in [132].

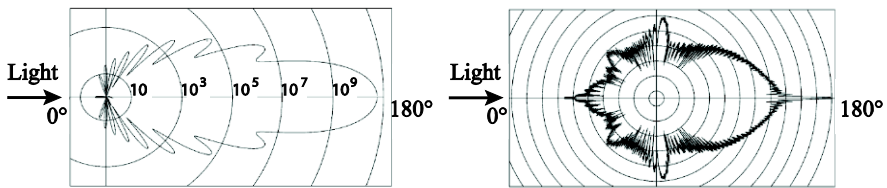


*Figure 1.6 On the left: Light scattering by a  $1\ \mu\text{m}$  glass particle in water. On the right: Light scattering by a  $30\ \mu\text{m}$  glass particle in water. Reprinted from Particle Image Velocimetry A Practical Guide, Second Edition, 2007, Pg. 20, M. Raffel, © Springer-Verlag Berlin Heidelberg 1998 2007, With permission of Springer.*

Generally PIV measurement seeding should be uniform over the entire measurement area. In laboratory studies of liquids closed flow tunnels are often used and it is relatively easy to obtain sufficient and uniform seeding, as particles can be added to the system before starting the experiment and letting them diverge

[129]. In the studies of gaseous fluids it is often not possible to use the closed tunnel and therefore the flow has to be seeded directly in front of the experiment area, making it more difficult to obtain uniform pattern. Particle image density can be too low, and in this case it is possible to detect and track the images of individual particles. The corresponding method is called PTV – particle tracking velocimetry. In the other extremum when the density is too high, it is not possible to detect individual particle images as they overlap and form speckles, in this case the measurement method is called LSV – laser speckle velocimetry [117], [133]. Approaches of image processing for PTV and LSV are also described in [134] and [135].

For high quality PIV measurements it is necessary to have about 15 particle images per interrogation window [136], for many experimental setups it has corresponded to the concentration of about  $10^8 - 10^{10} \text{ m}^{-3}$  [129].

In Table 1.1 frequently used particles in the studies of gaseous and liquid flows are shown.

*Table 1.1 commonly used particles in PIV ([119], [129]).*

<b>Gaseous flows</b>		<b>Liquid flows</b>	
<b>Material</b>	<b>d (μm)</b>	<b>Material</b>	<b>d (μm)</b>
TiO <sub>2</sub>	0.1 – 5	TiO <sub>2</sub>	3
Al <sub>2</sub> O <sub>3</sub>	0.2 – 5	Al <sub>2</sub> O <sub>3</sub>	9.5
Polycrystalline	30	Conifer pollen	50 – 60
Glass spheres	0.2 – 3	Polystyrene	15
Oil	0.5 – 10	Thermoplastic	6
Smoke		Microspheres	<30
Polystyrene	< 1	H <sub>2</sub> bubbles	
Glass balloons	0.5 – 10	Aluminum flakes	2 – 7
Helium filled soap bubbles	30 – 100	Hollow glass spheres	10 – 100
Granules for synthetic coating	1000 – 3000	Oil	50 – 100
	10 – 50	Oxygen bubbles	50 – 1000

### 1.4.3. Imaging

In the early years of PIV mostly photographic methods were used to record the particle images. Today, this has been replaced with digital imaging from CCD or CMOS sensors. A thorough comparison of CCD and CMOS cameras for fluid mechanics applications is provided by Hain et al. in [137]. Nevertheless photo or movie cameras with photographic films might be still used when super high resolution or high framerate is required [119], [138]. The resolution of a film can be up to 300 lines per mm for a 35 mm (Kodak Technical Pan) [118] which is still higher resolution than high speed digital PIV cameras have.

Three main modes of image acquisition are used. The first one – double-exposure recording – is used for both photographic film cameras and digital cameras. Two exposures are stored on the same frame, with the help of pulsed light source [117]. The advantages of this method is the possibility to use low speed cameras that usually are cheaper and getting smaller data amounts. The disadvantage is that from a double exposure frame, it is not possible to detect the direction of motion.

The second option is to use a high speed camera and store the single exposure frames continuously. This enables the use of both continuous and pulsed lasers; also frames are analyzed in pairs and the sign of the direction of motion is easily detectable.

The third option is to use the double-frame mode (frame straddling). This can be realized with a camera that has an electronic shutter. The camera outputs frames that each contain a pair of images with half of the vertical resolution. E.g. all odd lines comprise the first PIV frame and even lines comprise the second frame respectively [117]. Dedicated PIV cameras typically have the frame straddling time around 200 ns [139], [140] and even down to 1 ns [141] enabling the study of extremely fast flows. This method has also been realized with two synchronized cameras [142].

Keane and Adrian [136], Westerweel [143], McKeon et al. [100] have determined the general imaging criteria for optimal PIV analysis:

- The optimal particle image diameter is between 1 and 4 pixels;
- The number of particle images per interrogation area should be about 15 (10 - 15);
- The displacement of particle images should be about  $\frac{1}{4}$  of the diameter of the interrogation area;
- The out of plane displacement should be less than  $\frac{1}{4}$  of the diameter of the interrogation area;
- The flow velocity is measured as the displacement of the particle images

$$D(X; t', t'') = \int_{t'}^{t''} v[X(t), t] dt, \quad (1.21)$$

where  $D(X; t', t'')$  is the displacement of the tracer particles and  $v[X(t)]$  is the velocity of the tracer particle. It is assumed that the displacement field provides the average velocity over time interval  $\Delta t$ ,  $D$  cannot be the exact representation of the fluid velocity  $u$ , but rather an approximation with the error  $\varepsilon$

$$\|D - u\Delta t\| < \varepsilon \quad (1.22)$$

In order to  $\varepsilon$  to be negligible the spatial and temporal resolution of imaging must be small compared to the spatial and temporal resolution of the flow. If all requirements are properly fulfilled then the measurement error typically remains 1% or less [100].

#### 1.4.4. Data processing

In the early years of PIV optical methods it was common to rely on two-dimensional Fourier transfer of Young's fringe patterns to extract the velocity info from images [117], [119]. Detailed information about fully optical and semi-optical (the first Fourier transform is made optically and the second in the computer with FFT) methods is given in [144], [145] and about Fourier optics in general in [146].

Due to the development of personal computing power, the advances of digital cameras and the complexity of optical PIV (theory and practice of Fourier optics, optical and electro-mechanical parts and additionally the need to still use digital imaging and computers) the optical PIV evaluation is nowadays rarely used, instead digital spatial correlation is used. PIV images are divided into small interrogation areas and analyzed statistically. The commonly used method is discrete cross-correlation

$$R(x, y) = \sum_{i=-K}^K \sum_{j=-L}^L I(i, j) I'(i + x, j + y), \quad (1.23)$$

where  $R$  is the spatial cross-correlation,  $I$  and  $I'$  are the samples extracted from images so that  $I'$  is larger than the template  $I$ ,  $x$  and  $y$  are the coordinates of the image plane.

The template  $I$  is linearly shifted around in the sample  $I'$ , each sample shift  $(x, y)$  produces one cross-correlation value. This operation is repeated for a range of shifts, ultimately forming a correlation plane. The highest value in the obtained correlation plane is then used as the direct estimate of the particle image displacement [117], [147], [148]. As this method results in only the first order displacement vector (linear shift), the interrogation window size must be small such that the second order effects can be disregarded. The computational cost for a  $N \times N$  cross-correlation plane is  $O[N^4]$  operations. By utilizing the correlation theorem the cross-correlation of two functions provides an equivalent complex conjugate multiplication of their Fourier transforms. This makes it possible to

reduce the computational cost to  $O[N \log_2 N]$  [149]. Further reading about utilization and optimization of FFT in PIV can be found in [150]–[153].

The raw data obtained from cross-correlation often contains spurious and missing vectors. This can be caused by inhomogeneous seeding or illumination, out of plane motion of particles, or even poor quality camera lenses. In order to ensure that the PIV data is suitable for scientific work, post processing of the velocity fields is required. Common steps in post processing are: detecting and correcting spurious vectors, filling in the missing vectors and smoothing the data. In addition to the steps outlined in [117], more information about post processing the PIV data can be found in [154]–[157] as well as a discussion on the experimental uncertainties [158].

## 1.5. Conclusions

This chapter provides an overview of fish swimming, its classifications and physics of both the thrust and drag forces. The efficiency of fish (97%) still exceeds the efficiency of conventional propeller-based human made vehicles (efficiency up to 70%). Their outstanding energy efficiency especially in turbulent flows was illustrated with the description of migration on their long and difficult routes. However the migration in rivers is often blocked due to human made weirs and power plants that fish are not able to overcome, leading to the decrease in the population of migrating fish in these rivers.

The efficient swimming capabilities as well as the ability to adopt to different flow conditions properties should be studied in greater detail, resulting in underwater vehicles and robots with higher efficiency and capabilities.

Finally, a better understanding of fish, their locomotion and preferences in choosing routes and positions in flow could help engineers to design better fish passes to restore the natural migration routes for fish.

## **2 FACILITIES AND EQUIPMENT USED IN THIS THESIS**

This thesis provides an experimental study of the interaction of compliant bodies subject to turbulent water flows. Experiments were carried out in different flow tunnels, utilizing several velocity and force measurement techniques. This chapter describes in details the flow tunnels, measurement equipment and robotic fish prototypes.

### **2.1. Flow tunnels**

Experimental work with a robotic fish and lateral line prototype was carried out in three flow tunnels. That includes a closed and submerged tunnel located in the Centre for Biorobotics, Tallinn University of Technology, a 27 m long open top flow tunnel located in the University of Stuttgart, Germany and a 1:1.6 scale vertical slot fishway model located at the Karlsruhe Institute of Technology, Germany. The following sub-chapters describe these facilities in detail.

#### **2.1.1. Submerged flow tunnel in Tallinn University of Technology**

All experiments in studies described in Chapters 3, 4 and 5 were conducted in the flow tunnel located at the Centre for Biorobotics, Tallinn University of Technology, Estonia. The flow tunnel is fully submerged in a tank of dimensions 4×1.46×1.30 m (width × height × depth) and maximal water column height of 1.11 m. CAD drawing and a photo of the flow tunnel is shown in Figure 2.1. To ensure optical access to the working section, the tank has a glass wall and open top; the flow tunnel also has a side wall and top wall made from transparent glass. As the tunnel is submerged it is possible to reconfigure it by adding or removing parts as necessary with relatively little effort. The working section of the flow tunnel is 1.5 m long and has a cross section of 0.5×0.5 m. The flow is generated with the help of a AC motor АЙР100S2У3 (Mogilevsky zavod Electrodvigatel, Mogilev, Belarus) mounted on a Neptun 23 outboard motor, manufactured by The Chernyshev Moscow Machine-Building Enterprise (former *Московский завод «Красный октябрь»*, Moscow, Russia). AC motor is controlled using a frequency inverter of type MFR-F740 (Mitsubishi Electric Corporation, Tokyo, Japan). The relationship between the motor control frequency and flow speed from 0.05 – 0.5 ms<sup>-1</sup> has been validated with PIV. To achieve uniform flow, two sets of collimators with the 0.2 m gap distance are used in front of the working section, each of them consists of a grid of 0.15 m long rectangular channels with a cross section of 0.009×0.009 m. Further details of design and construction of the flow tunnel can be found in [127], with the exception of minor modifications.

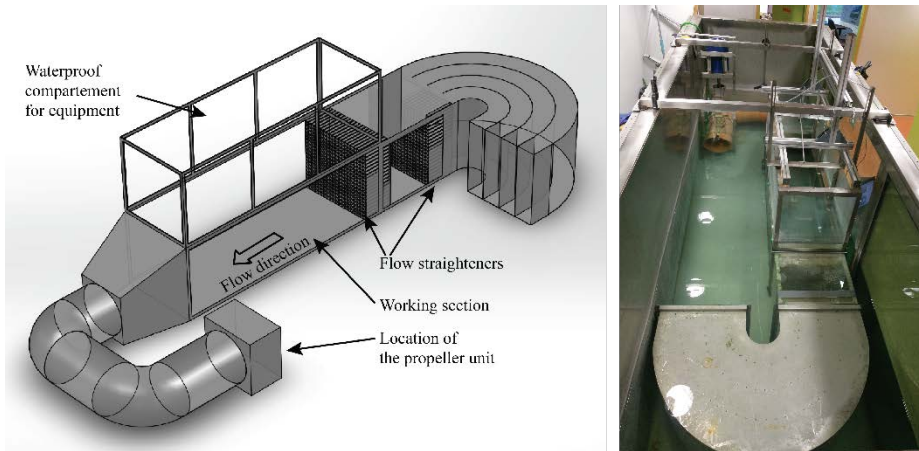


*Figure 2.1 Flow tunnel located at the Centre for Biorobotics, Tallinn University of Technology.*

### **2.1.2. Open top flow tunnel in the University of Stuttgart**

The flow tunnel used in experiments in Chapter 3.4. is located at the Institute for Modelling Hydraulic and Environmental Systems, University of Stuttgart, Stuttgart, Germany. Total length of the tunnel is 27 m, width is 1 m and height 0.6 m. Tested flow rates are from  $32 \text{ ls}^{-1}$  to  $276 \text{ ls}^{-1}$  with variable a slope from 0 to 11.5. The time-averaged flow speeds are from  $0.1 \text{ ms}^{-1}$  to  $1.2 \text{ ms}^{-1}$ . Photo of a experimental setup in the flow tunnel is shown in Figure 2.2.



*Figure 2.2 Left: typical experimental setup at the open top flow tunnel in the University of Stuttgart. 1 – Lateral line probe, 2 and 3 – acoustic Doppler velocimeters probe and data logger. Right: close up photo of the probes.*

### 2.1.3. Model of a vertical slot fish pass

The experiments described in Chapter 3.4. were conducted in the 1:1.6 scale model of a vertical slot fish pass constructed on the River Rheine in Koblenz, Germany. The model is located at the hydraulics laboratory of the Institute of Water and River Basin Management, Karlsruhe Institute of Technology, Karlsruhe, Germany. The scale model has 3 basins (the actual fish pass has 18 basins in total) and two user selectable flow rates of  $130 \text{ ls}^{-1}$  and  $170 \text{ ls}^{-1}$ . All experiments were conducted in the second basin (middle). A photo and a CAD drawing with dimensions of one of the basins is shown in Figure 2.3. More details on the model fish pass and its analysis can be found in [159].

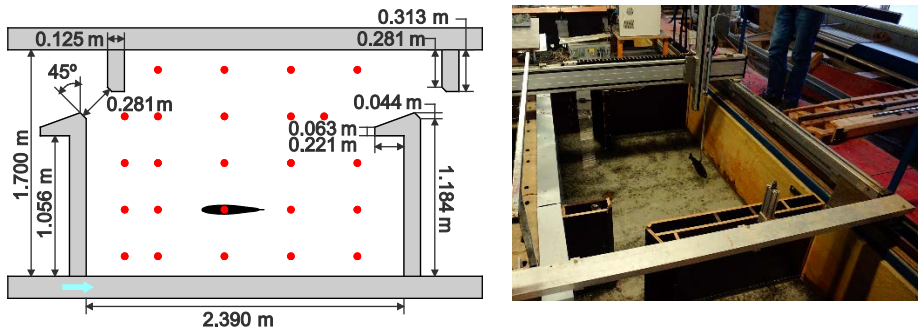


Figure 2.3 Left: drawing of a model fish pass, red dots represent the measurement points, black fish shape represents the lateral line probe and cyan arrow shows the flow direction (image on the courtesy of Juan Francisco Fuentes-Pérez). Right: photo of a second pool of the model fish pass and lateral line probe mounted on a Cartesian robot.

## 2.2. Measurement equipment

The work presented in this thesis was carried out with using multiple self-made and commercial measurement devices. The following sub-chapters describe the particle image velocimetry system and two force measurement devices designed and built in the Centre for Biorobotics, Tallinn University of Technology and one commercial particle image velocimetry system.

### 2.2.1. PIV system Version 1

The PIV system used for the experiments presented in Chapters 3.1 and 3.2 was a low-cost system built in house.

- As a light source a laser diode from 22x LG DVD writer (LG Corporation, Seoul, South Korea) was used, the light sheet was created with the help of one cylindrical lens mounted directly on the custom

housing of the laser. The wavelength of the laser is around 660 nm (red) and the maximum output power is between 200 and 250 mW [160], [161].

- As a camera, UI-5240HE-M (IDS Imaging Development Systems GmbH, Obersulm, Germany) was used. The camera achieves 60 fps at the resolution of  $1,280 \times 1,024$  pixels.
- Due to the low output power of the laser, relatively large particles – EPS-5 raw material (Polyston, LLC., Tallinn, Estonia) with a diameter of  $\sim 1$  mm were used.
- Data analysis was conducted in Matlab 7.1 (The MathWorks, Inc., Massachusetts, USA) using MatPIV 1.6.1 [162]. Additional details about the choice of software and its improvements are given in [127].

### **2.2.2. PIV system Version 2**

The second PIV system is a commercial product built by Dantec Dynamics (Dantec Dynamics A/S, Skovlunde, Denmark), it was used for the experiments presented in Chapter 3.3. The system consists of:

- RayPower 5000 – continuous class 4, 5W diode pumped solid state laser with a wavelength of 532 nm (green). Light sheet optics consist of multiple optical elements making it possible to adjust the fan angle from  $3^\circ$  to  $30^\circ$  and width of the light sheet.
- Synthetic polyamide tracer particles Vestosint 1101 (Evonik Industries AG, Essen, Germany) with a density of  $1.02 \text{ gmm}^{-2}$  and average diameter of 100  $\mu\text{m}$ .
- Single or stereoscopic cameras (2D or stereoscopic PIV) SpeedSense M310 with the resolution of  $1280 \times 800$  pixels and maximum frame rate of 3260 fps at full resolution.
- Dantec Timer Box 80N77 – enables to control and synchronize the camera with laser pulses (if pulsed laser is used) and other optional external equipment.
- DynamicStudio v4 – software package from Dantec Dynamics for configuring and controlling experimental equipment, data acquisition, pre/post processing and analyzing the data.
- Dedicated PIV PC – Dell Precision T7600 with two Intel Xeon E5-2609 processors and 8GB of RAM.

### **2.2.3. Force plate Version 1**

The first version of force plate was designed and built to measure the downstream and lateral forces in the flow tunnel and was used in the work described in Chapter 3. It consisted of two aluminum plates and four load cells with the working range up to 10 kg placed to the corners between these plates. Signals were amplified with instrumentation amplifiers INA128UA (Texas Instruments, Dallas, Texas, United States), digitized with the 16 bit analog to digital converter LTC1867 (Linear Technology, Milpitas, California, United States) and sent to PC with the help of ATmega168 (San Jose, California, United States) using RS-232 port. The force plate was calibrated with a commercial force gauge LG-5000A (Lutron Electronic Enterprise CO., LTD, Taipei, Taiwan). Force plate version 1 is shown in Figure 2.4.

### **2.2.4. Force plate Version 2**

The second version of the force plate was also custom made at the Centre for Biorobotics and was utilized in the work described in Chapters 4 and 5. This version has a completely sealed case, CNC milled from Polyoxymethylene (POM). In comparison to the previous version, it is also possible to measure the torque around the vertical axis. All sensors and electronics are located in a watertight compartment. Another upgrade is the changeable rod for attaching different objects. The rod can be thin to minimize its hydrodynamic effects or it can be larger and contain a DC motor for the devices that need external actuation. The force plate consists of four load cells for measuring stream wise and lateral forces and extra four load cells to measure the torque. The electronics is similar to the previous version, and consists of instrumentation amplifiers INA128UA, analog to digital converter LTC1867 and ATmega328 microcontroller. The device was calibrated using a LG-5000A force gauge.

## **2.3. Prototypes**

For the experimental work, the author used two different robotic fish prototypes, a set of silicone fish dummies with variable size and a lateral line probe – a novel device for measuring water flows from the perspective of fish. All prototypes were designed and mostly manufactured in the Centre for Biorobotics as a process of continuous studying and research in the fields of fish- and biorobotics.

### 2.3.1. Prototype 1

All fish models and fish robots used in this thesis are inspired by rainbow trout. The first prototype was used for the research described in Chapter 3. The body shape of the Prototype 1 was designed using the analytical model describing the body using elliptical cross-sections [163]. According to the proposed model the major and minor radiuses  $R$  and  $r$  of the cross-sections along the anteroposterior axis  $x$  are defined with the following equations

$$R(x) = R_1 \sin(R_2 x) + R_3 (e^{R_4 x} - 1), \quad (2.1)$$

$$r(x) = r_1 \sin(r_2 x) + r_3 \sin(r_4 x), \quad (2.2)$$

where  $R_i$  and  $r_i$  are constants depending on the species.

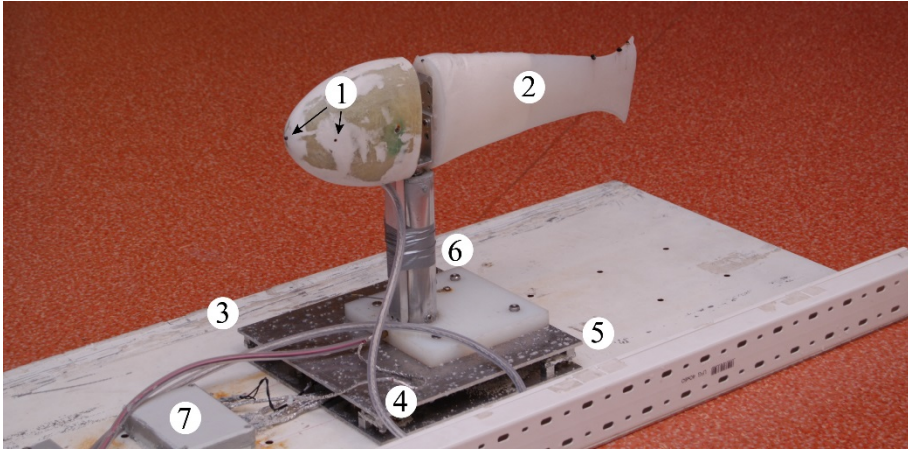


*Figure 2.4 Prototype 1 mounted on the force plate version 1. 1 – Rigid head, black arrows indicating pressure sensors; 2 – compliant tail; 3, 4, 5, 6 – load cells; 7 – watertight compartment for electronics.*

As mentioned earlier, trout is a subcarangiform BCF propulsor, meaning that it creates thrust by body and caudal fin propulsion with about 3/5 of the posterior body. The length of the first prototype is 0.43 m, maximum size on the dorsoventral axis is 0.125 m and on the left-right axis 0.06 m. To achieve a suitable bending stiffness, the posterior part of the body was casted from the combination of two materials Soma Foama® 15 (Smooth-On, Inc., Macungie, Pennsylvania, United States) and high performance platinum cure silicone rubber Dragon Skin® 10 (Smooth-On, Inc.). The anterior part of the prototype was built out of glass fiber and epoxy with a hollow compartment for the pressure sensors and electronics. Actuation of the tail was possible with an external DC motor mounted onto a force plate. Photo of the Prototype 1 is shown in Figure 2.4. Further details of designing and testing the tail, including determining the tail material properties can be found in [164].

### 2.3.2. Prototype 2 – fish dummies

To investigate the effect of the body size to hydrodynamic forces (research described in Chapter 4) in a vortex street, five different fish shaped dummies were made. To mimic a trout five freshly killed trout were brought from a local fish breeder and used to make gypsum molds. The bodies were casted purely from silicone rubber Dragon Skin® R10, the Young’s modulus DragonSkin R10 was determined experimentally by Salumäe [164] and found to be 181 kPa. The physical parameters of the dummies are shown in a Table 2.1.

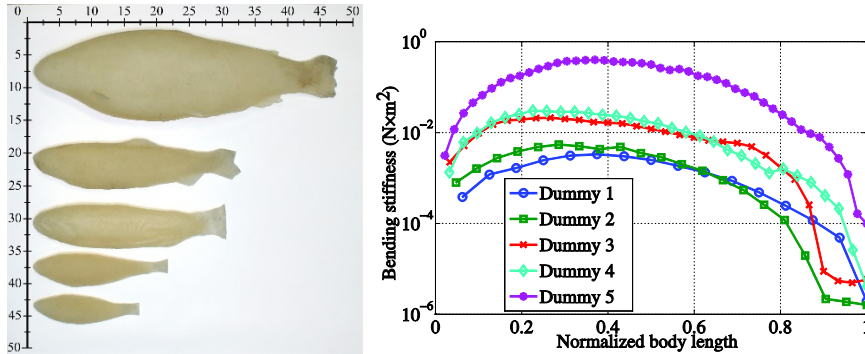


Figure 2.5 – Left: a photo of fish dummies. Right: Bending stiffness of fish dummies.

Table 2.1 Dimensions of the fish dummies.

Dummy number	Length (m)	Normalized length*	Height (m)	Width (m)	Transverse projected area (m <sup>2</sup> )	Mass (kg)	$I_{zz}^{**}$ (kg m <sup>2</sup> )
1	0.162	0.405	0.044	0.020	0.00477	0.0591	$7.37 \times 10^{-5}$
2	0.205	0.513	0.052	0.023	0.00674	0.0992	$1.66 \times 10^{-4}$
3	0.292	0.730	0.067	0.034	0.01512	0.336	$1.38 \times 10^{-3}$
4	0.314	0.785	0.070	0.038	0.01661	0.454	$2.31 \times 10^{-3}$
5	0.467	1.168	0.135	0.069	0.04222	1.720	$1.39 \times 10^{-2}$

\* Normalized against the wake wavelength of the vortex street used (0.4 m)

\*\* Fish dummy’s moment of inertia with respect to the axis (z) of the measured momentum

After production, body shapes of the dummies were 3D scanned using DAVID-Laserscanner Software (DAVID Vision Systems GmbH, Koblenz, Germany) and SolidWorks 2013 (Dassault Systèmes SOLIDWORKS Corp, Massachusetts, United States) was used to determine the physical parameters. For validation the prototypes were also manually weighed, height and width were measured with

the step of 0.01 m. The measured cross-sections were approximated as ellipses for calculating the bending stiffness. Results are plotted in Figure 2.5 along with the photo of dummies.

### 2.3.3. Prototype 3 – the X-prototype

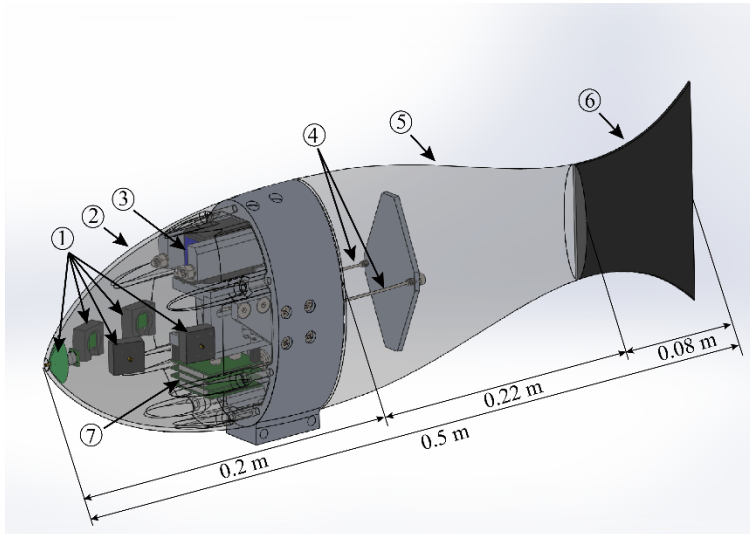


*Figure 2.6 – Prototype 3. 1 – pressure sensors, 2 – 3D printed rigid head, 3 – servo motor, 4 – a rigid plate and cables connecting it to the servo motor, 5 – soft tail, 6 – rigid caudal fin, 7 – ARM based computer.*

Prototype 3 was used in Chapter 5 and is referred to as “the X-prototype” since it had to be ready for Christmas 2010. The body motion mimics that of a rainbow trout, however the anterior part was constructed to house the electronics. The body is 0.5 m long with maximum size 0.15 m along the dorsoventral axis and 0.08 m along the lateral axis. The 3D-printed head and CNC-milled aluminum mid part of the body are rigid and watertight whereas the posterior part consists of a 0.22 m long compliant tail made out of a mixture of the Dragon Skin® 20 (Smooth On, Inc.) and Slacker® (Smooth-On, Inc.) including a 0.08 m long rigid tail fin. Cad drawing of Prototype 3 is shown in Figure 2.6. More information about the development of the initial and improved versions of the X-prototype can be found in [164] and [14] respectively. Modelling of the robot is described in [14], [115] and [165].

The prototype is self-actuating, using a high-power brushless servo motor Futaba BLS152 (Futaba Corporation, Mobarra, Japan) and a 400 MHz ARM based computer running Linux. As a sensory system the X-prototype has an artificial lateral line consisting of five piezo resistive absolute pressure sensors MS5407-

AM from Measurement Specialties (Measurement Specialties Inc., Hampton, United States).

### 2.3.4. Lateral line probe

In order to conduct in-situ flow measurements in fish passes on fish migration routes, a fish shaped sensor was created. Its body shape is same as of the fifth dummy described in Chapter 2.3.2 although exact dimensions due to the different manufacturing processes. The first 2/3 of the body is 3D printed out of ABS plastic and forms a waterproof enclosure for sensors and other electronics. The anterior part is made out of urethane rubber and is slightly flexible.

The synchronous collocated sensor system consists of 16 pressure sensors and two 3D accelerometers. One pressure sensor is placed at the nose, five sensors to the right side of the body, five at the left side of the body and five to the belly. The nose sensor together with laterally placed sensors form an artificial lateral line, mimicking one sensing modality of the octavolateralis system of real fish [166]. Body shape, its dimensions and location of sensors are shown in Figure 2.7.

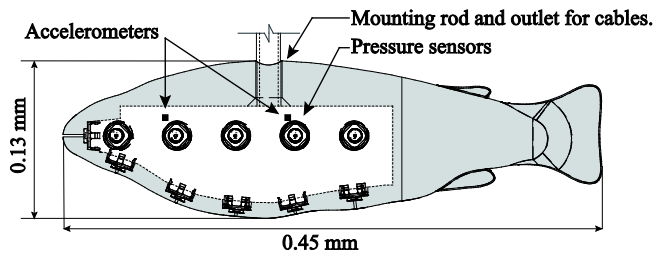


*Figure 2.7 – The lateral line prototype. 2D drawing of the lateral line prototype marking its size and locations of sensors. Laterally placed pressure sensors are equally placed on both sides. Dimension on the lateral axis (not marked) is 0.066 m.*

The pressure sensors used are of type SM5420-C-030-A-P-S (Silicon Microstructures, Inc., Milpitas, California, USA) and accelerometers are ADXL325BCPZ (Analog Devices, Inc., Massachusetts, USA). Pressure sensor signals are amplified in two stages, the first stage has a gain of 20.84 and uses an instrumentation amplifier AD8421ARMZ (Analog Devices, Inc.), resulting in a resolution of 7.6 Pa/LSB. In the second stage, signals are amplified 16.43 times with the operational amplifier AD8656ARMZ (Analog Devices, Inc.), providing signals at a resolution of 0.46 Pa/LSB. Sensor readings are sampled at 2500 kHz and subject to 10 times oversampling. The sensor data is then transferred to PC via virtual COM port, sampling frequency is user selectable from 50 Hz up to 500 Hz, where the latter is only available without second stage amplification.

The lateral line probe (LLP) was used in the work described in Chapter 6.

## **2.4. Conclusions**

The research presented in this thesis is experimental and utilized multiple robotic fish prototypes and a novel measurement devices. Fish robot prototypes were developed consecutively and the process ended up with a development of a complex measurement device – the LLP. Experimental work was conducted in multiple environments – three flow tunnels that were described in this chapter. As the tunnels located in Germany are fundamentally different from the one in the Centre for Biorobotics, they allowed experiments which would not have been feasible or even possible in the flow tunnel located at the Centre for Biorobotics. Also the PIV systems and custom made force measurement equipment described here made possible the research presented in Chapters 3, 4, and 5.

### 3 POSITIONING IN A VORTEX STREET

Flow turbulence is considered as disturbance for robots whereas for fish it can act as both sources of information and energy reduction (see Chapter 1). Therefore an improved understanding of drag and lateral forces considering regular turbulence would aid roboticists in future developments and the control of underwater robots. One key design requirement in underwater robotics is the robot's energy expenditure. Developing the ability to take advantage of the flow and its structures, similar to fish, is one possible way to achieve increased energy efficiency and thus extend the working time and or reduce the battery requirements.

This thesis studies the interaction of water and fish shaped objects to better understand the design requirements for fish robots. The problem is studied using PIV and force measurement techniques described in Chapter 2.2. Chapters 3 and 4 focus on experimental studies of forces affecting compliant fish shaped bodies in turbulent flows, Chapter 5 describes the improvement of indirect and non-intrusive force measurements using a data-driven method derived from signal processing. The final chapter introduces a novel instrument to measure complex flows from the fish's perspective. Thus the focus is not only on developing better robots, but also how to leverage fish like sensing to explore natural habitats thus making it possible to understand complex hydrodynamic environment – fish passes and rivers – from the fish perspective.

This chapter is based on the research published in [167] (APPENDIX A).

As described in Chapters 1.1.2 and 1.2.1, fish swim more effectively in turbulence, especially in regular turbulence. The aim of this research is to study how the magnitudes of hydrodynamic forces affecting the robot change in a vortex street depending on the robot's position. The knowledge gained from these experiments can be used when planning swimming routes of fish like robots as it shows which regions are favorable and which should be avoided. Experiments were performed by inserting a fish shaped robot into different locations behind an object that created a vortex street. The robot was rigidly fixed and the forces were directly measured.

#### 3.1. Materials and methods

For the experiments we used Prototype 1 (Chapter 2.3.1) and the first version of the force plate (Chapter 2.2.3), all experiments were run in the flow tunnel (Chapter 2.1.1). We used two flow configurations – uniform flow and a Kàrmàn vortex street created with the help of a D-shaped semi cylinder with an outer diameter of 0.1 m. For both cases two free stream velocities were investigated,  $0.31 \text{ ms}^{-1}$  and  $0.48 \text{ ms}^{-1}$ . Velocities were measured and the presence of a stable vortex street was determined with DPIV system 1 (Chapter 2.2.1). A dedicated PIV post processing toolbox developed for Matlab by Visentin et al. [168] was

used for analyzing PIV data. For validation the theoretical parameters  $R_e$ ,  $S_t$ , and  $f_{vs}$  of the vortex streets were calculated.  $R_e$  was calculated using Equation 1.2.  $S_t$  was calculated from  $R_e$  with Equation 3.1, this equation holds if the  $R_e$  is between 250 and  $2 \times 10^5$ .

$$S_t = 0.198 \left( 1 - \frac{19.7}{R_e} \right), \quad (3.1)$$

The vortex shedding frequency was calculated using the equation

$$f_{vs} = \frac{U \times S_t}{D}, \quad (3.2)$$

where  $U$  is the flow speed and  $D$  is the diameter of a cylinder.

In order to move the force plate and fish robot along x and y axis a custom rig was built. The position of the measurement equipment was adjusted manually. In order to further investigate the relation between the hydrodynamic forces and the downstream position of a fish robot, a series of experiments were conducted varying the distance between the cylinder and the nose of the robot between 0.05 m and 0.35 m with an increment of 0.03 m. The lateral position was kept fixed at the center line of the vortex street. The relation between the forces and lateral position of a robot was determined by fixing the fish robot 0.2 m downstream from the cylinder and varying the lateral position  $\pm 0.1$  m from the center line using an increment of 0.025 m. At each position we recorded the force values for 90 s.

### 3.2. Results of flow analysis

For the lower flow speed the velocity profile for  $V_x$  and turbulence intensity are shown in Figure 3.1 a) and b) respectively. Key values of the vortex street parameters are the suction zone length, which was at 0.11 m for both flow speeds, the vortex street width of 0.23 – 0.24 m, wake wavelength for lower flow speed was 0.32 m and for higher flow speed 0.26 m, vortex shedding frequencies 0.68 Hz and 1.13 Hz respectively. Additional details can be found in Table 1 in APPENDIX A

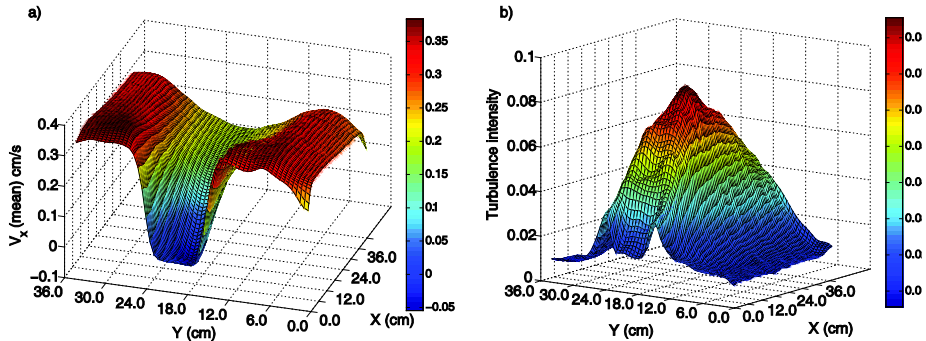


Figure 3.1 Results of flow analysis of  $0.31 \text{ ms}^{-1}$  flow scenario. a) – time averaged velocity  $V_x$ ; b) – Turbulence intensity. © 2012 IEEE [167].

A strong correlation between the predicted and measured values was found, and the flow field behind the cylinder can be divided into clearly distinguishable regions:

- the suction zone with a negative  $V_x$ . The suction zone is also shown in Figure 3.1 a) – the blue color indicates the negative (flowing backwards) velocity;
- vortex formation zone – the region where vortices are formed;
- vortex shedding point – the point where fully formed vortices are “detached” and start to move along the flow, this region is marker in Figure 3.1 b) with dark red;
- the vortex street – region where vortices are advected along the flow at nearly constant speed.

### 3.3. Results of force measurements

At first comparative experiments of the forces in uniform flow and in Kàrmàn vortex street using both flow speeds were made where Prototype 1 was fixed 0.23 m from the cylinder (directly after the vortex shedding point). Results are shown in Figure 3.2. It is seen that for the  $0.31 \text{ ms}^{-1}$  flow speed, the drag force ( $F_x$ ) is 42% smaller in the vortex street than in uniform flow, and at  $0.48 \text{ ms}^{-1}$  the difference is 38%. Lateral forces significantly increased in the vortex street as the vortices alternately push the body from the left and the right.

The relation of forces affecting the robotic fish as a function of its downstream position are shown in Figure 3.3, it is seen that the drag force  $F_x$  follows the same trend with  $V_x$  and until the distance of 0.15 m from the cylinder the drag force is negative – a passive fish robot tries to move forward. This is in good agreement with the suction zone length. It must be noted that even when the anterior end of the robot (up to 0.1 m) is in the suction zone, the majority of its body is still affected by the downstream flow as the total body length of Prototype 1 is 0.43 m. In the vortex formation zone (up to 0.19 m) the drag force increases rapidly and after which the increase slows down until it terminates as the robotic fish is too far from the cylinder to take advantage from the shadowing effect.

Analysis of lateral velocity  $V_y$  and lateral force  $F_y$  are done in the RMS domain as they are oscillating around zero. Results are plotted in Figure 3.3 b).  $F_y$  also follows the same trend with the  $V_y$  and a rapid increase of  $F_y$  is seen after the vortex shedding point.

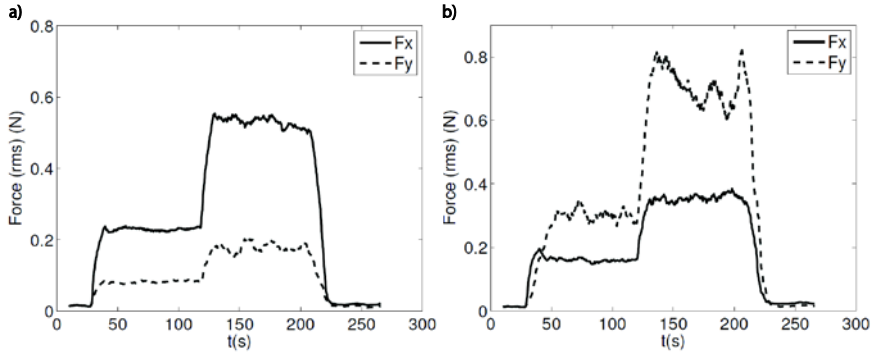


Figure 3.2 Comparison of forces measured in uniform flow and in vortex street, for the flow speeds of 0.31 ms<sup>-1</sup> ( $30 < t < 120$ ) and 0.48 ms<sup>-1</sup> ( $120 < t < 240$ ). First 30 s and last 60 s corresponds to still water. a) – measurements in uniform flow; b) – measurements in a vortex street. © 2012 IEEE [167].

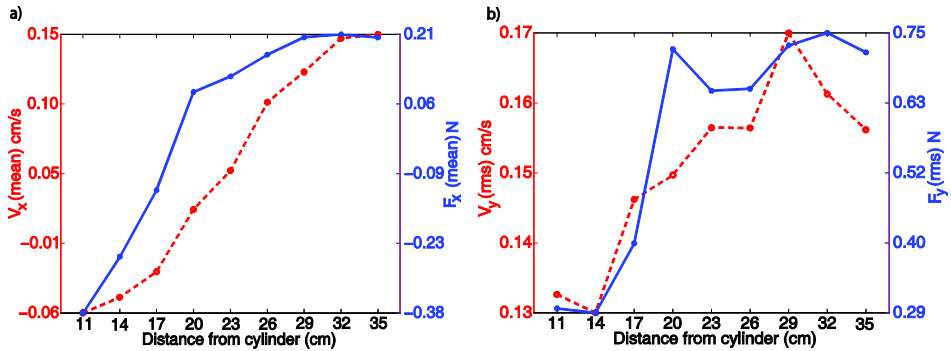


Figure 3.3 Drag force and lateral force versus downstream distance from the cylinder at the flow speed of 0.48 ms<sup>-1</sup>. a) Average drag force versus downstream position; b) RMS value of lateral force versus downstream position. © 2012 IEEE [167].

Study results on the lateral deviation from the center of the vortex street are plotted in Figure 3.4. It is seen that the drag force depends entirely on the  $V_x$  and both of them depend strongly on the lateral position. This result has a strong correlation with the PIV flow field indicating that smaller flow speeds are to be expected along the center of the vortex street and higher speeds at the edges and outside of it.

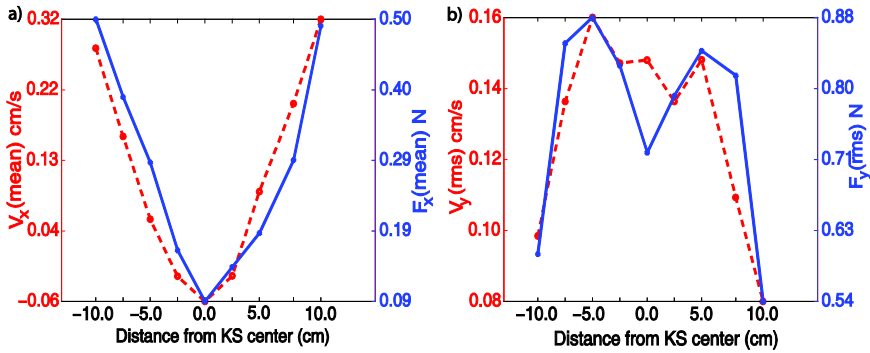


Figure 3.4 Drag force and lateral force versus lateral deviation from the vortex street center at the flow speed of  $0.48 \text{ ms}^{-1}$ . a) Average drag force versus lateral position; b) RMS value of lateral force versus lateral position. © 2012 IEEE [167].

Plots of  $F_y$  and  $V_y$  are both M shaped which matches the PIV analysis results – peaks for both  $V_y$  and  $F_y$  are located at the centerlines of the vortex rows (-0.05 m and +0.05 m from the center of the street) and after the vortices both  $V_y$  and  $F_y$  are decreasing rapidly. Measurements in all points except in the center of the street follow the same trend. This is caused by the fact that the wake wavelength of the vortex street is 0.23 m while the length of Prototype 1 is 0.43 m. Two oppositely signed vortices are affecting the prototype simultaneously from both sides, counterbalancing the lateral forces.

### 3.4. Conclusions and discussion

We conducted experiments with passive fish robot in a flow tunnel using two flow speeds and two different flow conditions – uniform flow and vortex street. The aim was to study the force-position relationship in a vortex street and compare these results to uniform flow scenarios. Experiments show that when increasing the flow speed the drag force affecting the robot in uniform flow increases considerably while the change (and overall magnitude) in lateral forces is negligible. In the vortex street it is vice versa –  $F_y$  has higher magnitude and also changes more. For the lower flow speed ( $0.31 \text{ ms}^{-1}$ ) the drag force is 42% smaller compared to the drag force in uniform flow, for the higher flow speed ( $0.48 \text{ ms}^{-1}$ ) the difference is about 38%.

In general both  $F_x$  and  $F_y$  are changing considerably depending on the location of a robot in the vortex street. The drag force has a single local minimum along longitudinal and lateral axis. This point can be used as a set point for underwater robots swimming in a complex environments in order to:

- hold station to communicate, reload batteries, etc.,

- swim forward with a minimum effort,
- follow another underwater vehicle with minimal energy expenditure.

We have shown that it is possible to minimize drag and thus energy consumption by searching for a suitable place in the flow. This can be done by analyzing the oncoming flow or by directly monitoring the current consumption of motor(s). The results of this study are later used by Salumäe and Kruusmaa to develop a control for station holding for Prototype 2 in KVS [169]. The other option to save energy is to interact with the flow more akin to real fish (Kàrmàn gaiting) as described in section 1.1.2. The second option has been implemented on a stationary fish robot with the efficiency gain of 23% by Ježov in 2012 [48]. Both methods are valuable when designing underwater vehicles for complicated environments or special purposes e.g. trailing either biological or man-made objects. While Kàrmàn gaiting is realizable on biomimetic robots, the first method is applicable also for traditional robots.

## 4 BODY LENGTH TO WAKE WAVELENGTH RATIO

Experiments with real fish show that not all fish prefer to use the Kàrmàn gaiting zone, e.g. in experiments conducted by Liao [56] fish spent 80% of the total time in the Kàrmàn gaiting zone while in experiments made by Przybilla [43] this value was only 7.9%. It is not known why some fish prefer to utilize the vortex street and others do not but an important factor is believed to be the fish body length to the cylinder diameter ratio [54], [56]. This chapter focuses on the study of hydrodynamic forces acting on different sized fish-shaped objects in a same vortex street.

The aim of this study is to experimentally show how the forces change and if they can still be used by fish or robots for energy saving. This knowledge can be useful when designing and dimensioning a biomimetic underwater robot for specific environments. The research presented in this chapter is based on the results published in [170] (APPENDIX B).

### 4.1. Materials and methods

In this study the Prototypes No. 2 – fish dummies were used. A detailed description of the dummy fish and their production is given in section 2.3.2. Force measurements were conducted with the force plate version 2 (details in chapter 2.2.4) and the flow was measured with the DPIV system 1 (chapter 2.2.1). All experiments were conducted in the flow tunnel described in chapter 2.1.1. Force and torque were measured with instrumentation uncertainties of  $u(F_y) = F_y \times 8.27 \times 10^{-5}$  and  $u(\tau) = \tau \times 4.83 \times 10^{-4}$  at confidence level on 95% while the detected standard deviations of the measurement noises were  $\sigma_{F_y} = 0.377N$  and  $\sigma_\tau = 0.0025Nm$ .

A Kàrmàn vortex street was generated with the help of a semi cylinder with a diameter of 0.1 m. In all experiments the flow speed was fixed to  $0.3 \text{ ms}^{-1}$  resulting in a Reynolds number of 30000. Initial PIV experiments were performed without dummies to acquire data about global flow conditions. To cover a longer area in the tunnel, two camera positions with a small overlap were used. The first field of view started directly behind the straight edge of the semi cylinder and covered the horizontal distance of 0 – 0.42 m, the second position covered 0.35 – 0.77 m as shown in Figure 4.1. The width of the field of view was 0.42 m leaving out 0.04 m from both edges of the tunnel.

After the flow regime characterization the lateral force for the unit area ( $1 \text{ cm}^2$ ) was measured. A metal plate with a surface area of  $4 \text{ cm}^2$  was mounted on the force plate and inserted to the flow tunnel. The force signals were recorded and used in MATLAB to generate an idealized force signal with the same amplitude and wavelength to estimate the forces affecting on prototypes.

This idealized  $F_y$  and transverse projected surface areas of fish dummies were used to calculate the theoretical torque that would affect the dummies in the flow. To simplify the model some assumptions were made. The bodies of prototypes were assumed to be stiff and flat, their lengths were rounded to the nearest integer and the drag force was ignored. Theoretical torque was calculated with the Equation 4.1:

$$\tau = \sum_{i=1}^n F_{y_i} A_i (l_i - l_{com}), \quad (4.1)$$

where  $\tau$  is torque,  $F_y$  is the lateral force applied to the unit area,  $A$  is the surface area of prototypes body at given position,  $l$  is distance from the nose (calculation point's coordinate),  $l_{com}$  is the coordinate of center of mass,  $i$  is position (coordinate) on the body, and  $n$  is number of subdivisions ( $n = \text{bodylength}$  as the length of each subdivision is 0.01 m).

Finally, tests with fish dummies were conducted. Dummies were fixed to the force plate with an aluminum rod with a diameter of 12 mm, the rod was isolated from the flow using a plastic pipe fixed to the body of force plate. Each prototype was one by one fixed to the rod at their center of mass and placed so that the nose of the prototype was 0.35 m downstream from the cylinder's edge. Comparative experiments with uniform flow at the same location in the flow tunnel were also made. LabVIEW was used to record both the force signals and PIV videos simultaneously. Each experiment lasted 120 seconds, the first 60 s were used to let the flow conditions fully develop and the following 60 s were used to record the data. The sampling frequency for the force plate was 100 Hz and for PIV camera 50 Hz, both limited by the hardware specifications. Data processing was done later using MATLAB.

## 4.2. Results of flow analysis

Before the actual experiments the expected Strouhal number and vortex shedding frequency were calculated with Equations 3.1 and 3.2. For the  $0.30 \text{ ms}^{-1}$  flow speed the theoretical  $F_s$  was 0.74 Hz and  $S_t$  was 0.2. To determine the presence of a stable Kàrmàn vortex street and its parameters 500 frames of PIV data were analyzed again with a MATLAB based post processing toolbox. The detected key parameters for this study were the following: the vortex shedding frequency was 0.7 Hz, wake wavelength was 0.4 m, street width was between 0.138 – 0.226 m and vortex shedding point was about 0.195 m from the cylinder. More details about the vortex street are given in Table 2 in APPENDIX B. As in the previous chapter (Chapter 3), predicted values were found to provide an overall satisfactory match to the measurements.

To validate the presence and stability of vortices in the whole experiment area the automatic vortex tracking function of the PIV toolbox was used for the both camera locations. The results are plotted in Figure 4.1, it is clearly seen that

vortices are present in the whole region. From the figure it is also seen how the vortex strength grows in the vortex formation region until to the shedding point and then starts decreasing when the vortex travels downstream. The average vortex strengths measured in the region where fish dummies were placed are decreasing slowly, meaning the vortex street is stable and suitable for experiments. Strength values vary more when measured further away from the cylinder but are still easily detectable by the MATLAB toolbox.

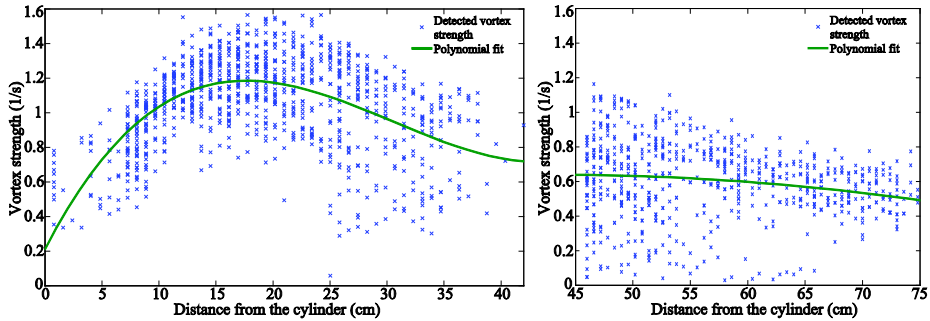


Figure 4.1 Vortex' strength versus its distance from the cylinder. On left: the first position of the camera. On right: the second position of the camera.

### 4.3. Results of force measurements

Results from experiments in uniform flow and in the vortex street are plotted along with the theoretical torque values in Figure 4.2. Small non-periodic fluctuations are seen in the uniform flow measurements, these can be caused by the irregularities in the flow and by the defects of the dummy bodies. The results show that the heavily simplified model have an acceptable match with the data from real experiments. However considering the experimental data, it was found that the strength and wake wavelength of travelling vortices varies. It is also seen that  $\tau$  is minimal for the two smallest fish dummies. After the point where the body length exceeds half of the wake wave length (two opposite signed vortices are pushing the body from anterior and posterior end at opposite sides) a higher  $\tau$  is produced.

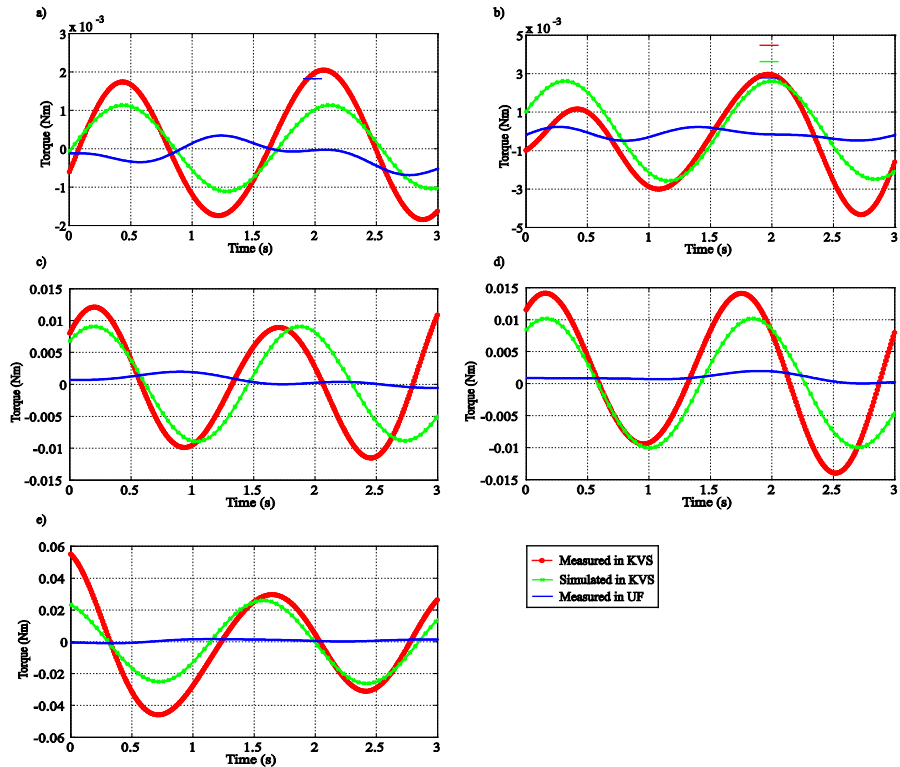


Figure 4.2 Measured and simulated torque for five fish dummies in uniform flow (UF) and in a Kàrmàn vortex street (KVS). Results are plotted in order of size starting from the smallest dummy in a) and ending with the largest one in e).

Figure 4.3 show that the RMS values of both  $\tau$  and  $F_y$  are increasing along with the body size. However since the body mass and moment of inertia are also increasing, the yaw and sway motion are reduced.

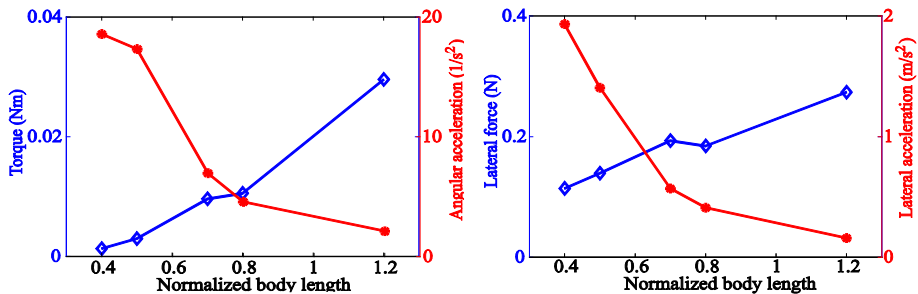


Figure 4.3 Torque and lateral force versus body length. Body lengths of fish dummies are normalized to the wake wavelength of the vortex street.

To validate the theory of vortex spacing on the body and resultant forces the PIV processing results were plotted along with the force and torque measurements. Both measurements were synchronized making it possible to match up the force data to the corresponding PIV image frame. Results for the smallest and biggest prototype are shown in Figures 4.4 and 4.5 respectively.

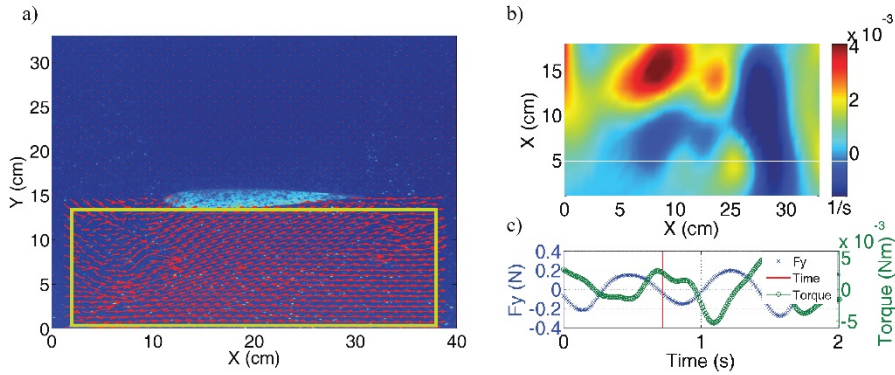


Figure 4.4 PIV along the left side of the smallest dummy. a) vector field, yellow rectangle marks the region where vorticity analysis were done; b) vorticity, red color marks counter clockwise vortex and blue color corresponds to clockwise vortices; c) torque and lateral force, red line marks the time corresponding to the PIV image.

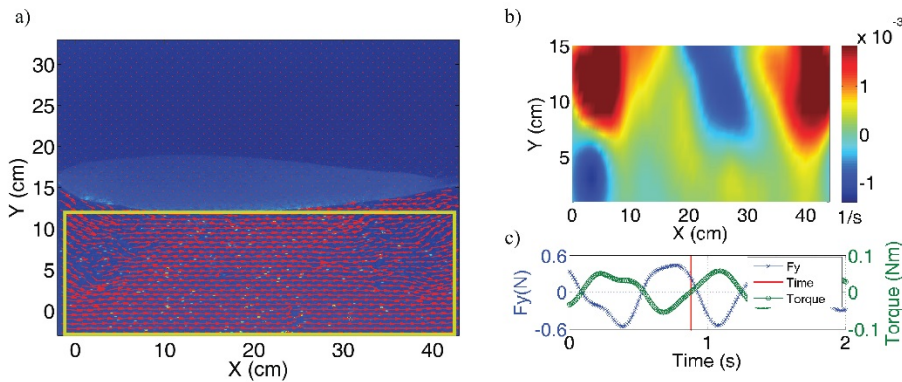


Figure 4.5 PIV along the left side of the largest dummy. a) vector field, yellow rectangle marks the region where vorticity analysis were done; b) vorticity, red color marks counter clockwise vortex and blue color corresponds to clockwise vortices; c) torque and lateral force, red line marks the time corresponding to the PIV image.

From Figure 4.4 it is seen that when a CCW vortex contacts the fish dummy, the maximal CW torque is generated. In Figure 4.5 two CCW vortices impinge the body, one from the head and one from the posterior part of the body, at the same time one CW vortex impacts the body from the opposing side about the center of

the body. From the force measurement it is seen that at this point the torque felt is almost zero, however there is some net lateral force affecting the body.

#### 4.4. Conclusion and discussion

In this study we investigated hydrodynamic forces affecting fish shaped objects subjected to a Kàrmàn vortex street. We conducted direct force measurements with five different sizes of fish dummies as well as PIV experiments of the Kàrmàn vortex street with and without fish dummies. Body lengths were in the range from 0.16 m to 0.47 m while the wake wave length of the vortex street was 0.4 m. In previous similar studies with hydrofoil [58] and flexible cylinders [62] the body length to wake wave length ratio was less than 0.5. Additionally, a simplified model predicting the yaw motion of passive fish shaped body was created and its results were correlated with direct force measurements and PIV analysis showing experimentally how vortices are traveling along the body and how they could induce yaw and sway motions which are part of the Kàrmàn gaiting [51].

One possible explanation to the passive yaw motion is shown in Figure 4.5. If a fish or fish like robot is passive, the forces coming from a vortex or vortices on the side of it are responsible of the characteristic motions of the Kàrmàn gaiting. Figure 4.6a shows a fish dummy with a body length shorter than half of a wake wavelength, in this case it experiences high  $F_y$  but smaller  $\tau$  compared to a dummy whose body is affected by two vortices from opposite sides (see also Figure 4.4). This means that if the smallest prototype would not be harnessed it would experience heavy sway motion. This result agrees with the previous studies of Lupandin where he showed that when the fish body length scale is too small compared to the vortex length scale (when the vortex size exceeds two-thirds of a fish body length) then vortices distract the fish and its swimming performance decreases [171].

Interestingly, a completely different situation occurs with the fifth and largest dummy. Its body length exceeds the wake wavelength of travelling vortices such that it is always affected by two or three vortices. The resultant force of multiple vortices depends on their location, swirling direction and strength. From Figure 4.6e it is seen that when the body is simultaneously influenced by three vortices the resultant torque should be zero or minimal and also the lateral motion caused by vortices should be small. This is verified by the PIV analysis shown in Figure 4.5. Two vortices of the same sign work in concert to push the body from anterior and posterior ends cancelling out each other and in opposition to the third opposite signed vortex on the other side of a body. Although vortices become distorted and are dissipated when travelling along the flow due to the surface friction and viscous forces they still significantly influence its motion.

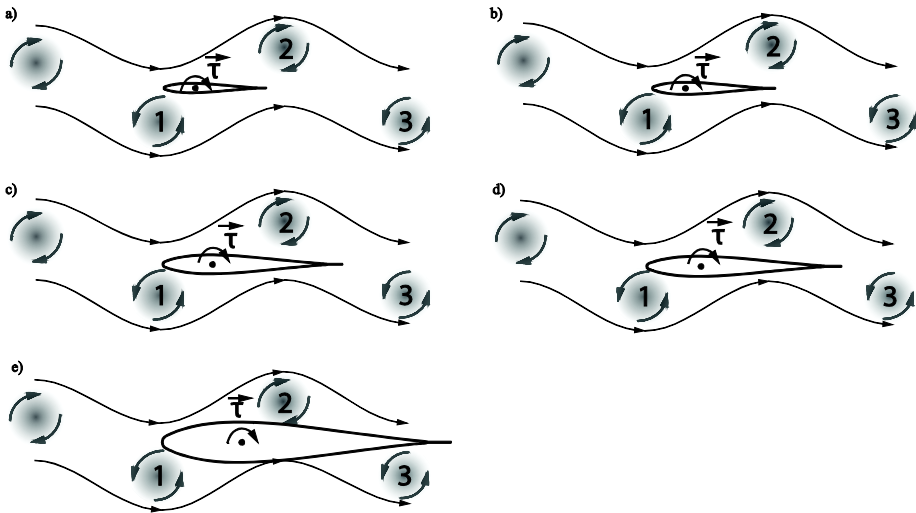


Figure 4.6 Scaled representations of fish bodies with respect to the vortex street for all tested cases (adapted from Liao, 2003). a) fish body length is smaller than half of the wake wavelength and fish is affected by only one vortex; b) normalized body length is 0.5, and vortices 1 and 2 are affecting the fish from the opposite sides, resulting in the maximum rotational torque  $\tau$  and minimal lateral force; c) – d) normalized body length is from 0.5 to 0.8 and bodies are affected simultaneously by two vortices; e) normalized body length is 1.2, two opposite signed vortices (1 and 2) are generating the torque  $\tau$ , while the third vortex (3) is counterbalancing this effect.

Fish dummies 2, 3 and 4 have body lengths longer than the first, smallest, one and shorter than the fifth, largest one, and their force measurements also fall between the first and the fifth one. Starting from the body length to wake wave length ratio of 0.5 until to about 1, fish dummies are affected by one or two vortices simultaneously depending on their position. From Figure 4.6 it is seen that the torque measured for the second dummy is 10 times higher than of the first one. Situations when it's being influenced by one or two vortices alternate periodically causing strong oscillating  $F_y$  and  $\tau$  which in turn cause alternating heave and yaw motions – the characteristic Kàrmàn gaiting movements – suggesting that there is a minimal body length that is needed to properly exploit vortices.

One of the aims of this study was to see if there is a specific range of the ratio of body length to wake wavelength where the passive Kàrmàn gaiting is efficient and what happens if the body length exceeds the wake wavelength. We showed experimentally that after this point,  $F_y$  and  $\tau$  do not decrease. Instead, the phase shift between  $F_y$  and  $\tau$  increases along with the body length to wake wave length ratio and for the fifth dummy it reaches nearly  $180^\circ$ . However the best phase shift for effective energy harvesting is previously shown to be  $90^\circ$  [58]. Secondly since

the body mass and inertia also grow, the resultant angular and rotational accelerations and thus yaw and sway motions decrease commensurately.

This work has some limitations which however allowed us to directly measure the hydrodynamic forces. Firstly the artificial fish were stiff compared to real biological fish and secondly they were rigidly fixed to the force plate which did not allow them to yaw or sway. Nevertheless this study supports the hypothesis that there is a certain body length to wake wave length ratio when the Kàrmàn gaiting of is effective and helps to understand the complex locomotion of fish in turbulence. The results are also important when designing fish like robots for turbulent environments as they show how the hydrodynamic forces change depending on the body size or environment. Based on these new findings, roboticists can optimize the body size of a robot or develop control strategies that can handle effects caused by hydrodynamic forces. Alternatively, an active control of body length or stiffness could help to control the phase angle and hence use the energy of vortex streets with different parameters.

## 5 IMPLEMENTATION AND IMPROVEMENT OF INDIRECT FORCE MEASUREMENTS

In Chapters 3 and 4 all forces were measured directly as the testing bodies were affixed to the force plate. The method presented chapters allows for the precise measurement of forces but is subject to some basic constraints: the submerged body (in this case a robotic fish) has to be stationary and in order to measure momentum, the yaw motion has to be restricted. Fish however move also laterally along with the yaw motion when they swimming in uniform flow and especially when slaloming between vortices e.g. Kàrmàn gaiting. In order to measure forces without disturbing the natural motion of real fish or fish like robots the measurement have to be indirect and ideally could be used both in laboratory conditions and in the field, e.g. rivers or fish passes.

Swimming fish generate a strong vortical wake behind the tail that is easily detectable at least 30 s after the fish was swimming in the measurement region and distinct particle motion can be detected for as long as 3 minutes [172]. One way of measuring forces is to use PIV velocity fields and directly link thrust to the geometry and strength of the vortical wake behind the tail [39], [173]–[177].

The present chapter focuses on the implementation and improvement of indirect underwater force measurements and is based on the work published in [178] (APPENDIX C).

### 5.1. Materials and methods

All experiments were conducted in the flow tunnel described in Chapter 2.1.1. Prototype 3 – the X-prototype (Chapter 2.3.3) was used together with the second PIV system and the second version of the force plate, description of these measurement systems can be found in Chapters 2.2.2 and Chapter 2.2.4 respectively. Experiments were divided into two phases, in the first one the robotic fish was kept passive (no body actuation), and lateral and stream wise forces were measured along with PIV images. Six different flow speeds were used, from  $0.1 \text{ ms}^{-1}$  to  $0.35 \text{ ms}^{-1}$  with the increment of  $0.05 \text{ ms}^{-1}$ . In the second phase the X-prototype was actuated to match the flow speed. The actuation frequency was kept constant (2 Hz, the natural frequency of the tail) and the tailbeat amplitude was varied according to the following equation [169]:

$$V = \frac{A+9.1}{1.56}, \quad (5.1)$$

where  $V$  is the swimming speed and  $A$  is tail beat amplitude. If  $V$  is equal to flow speed the freely swimming robotic fish will hold station.

The experimental procedure involved the following steps:

- the fish robot was fixed to the force plate without the possibility to move in the streamwise or lateral directions;
- forces were measured in still water;
- flow was started and after switching to new flow speed the flow was let to develop and stabilize at least 60 s before measurements;
- force signals ( $F_s = 80$  Hz) and PIV images ( $F_s = 400$  Hz) were recorded simultaneously for 10 seconds for every flow speed;
- Dantec Timer Box was used to synchronize the PIV camera and PC with the PC controlling the X-prototype and force plate;
- flow speeds 10, 15 and 20 were repeated with X-prototype actuated according to Eq. (eelmine valem saba liigutamiseks).

## 5.2. Data analysis

Dynamic forces are estimated from velocity vectors by relating the rate of change of momentum to the sum of forces. A planar discrete approximation (Equation 5.2) of Equation 1.9 is used, with small modifications – lateral velocities are included and pressure components neglected. The same approach has previously been used by Leftwich and Smits in 2011 [177] and Leftwich in 2012 [179]:

$$\begin{aligned} \Delta M_x(t) = & \sum_1 \rho u^2 \Delta L + \sum_2 \rho uv \Delta L - \sum_3 \rho u^2 \Delta L - \sum_4 \rho uv \Delta L \\ & + \frac{1}{2\Delta t} \left[ \left( \sum_x \sum_y \rho u \Delta L^2 \right)_{i+1} \right. \\ & \left. - \left( \sum_x \sum_y \rho u \Delta L^2 \right)_{i-1} \right], \end{aligned} \quad (5.2)$$

where  $\Delta M_x(t)$  is the instantaneous streamwise momentum flux,  $u$  and  $v$  are streamwise and lateral velocities.  $\Delta L$  is PIV spatial resolution (distance between vectors) and due to the same dimensions in lateral and streamwise directions  $\Delta L_x = \Delta L_y = \Delta L$ .  $\Delta t$  is the time step between PIV images. The terms 1 to 4 correspond to the surfaces shown in Figure 1.2 and represent the streamwise momentum flux through each of those surfaces.

Errors between directly measured and PIV estimated forces ranged from few percent to well over 50%. To compensate against these errors a general transfer function enabling robust estimations of  $F(t)$  from  $\Delta M(t)$  was created. By using the convolution theorem with impulse response  $h(t)$ , transfer functions were generated separately for all flow speeds and also separately for longitudinal and lateral flow speeds. The relationship between measured and estimated forces was found to be linear and the general transfer function  $H(H_{10}, H_{15}, H_{20})$  for each set of experiments was created so that the estimates of  $F(t)$  from  $\Delta M(t)$  were as

accurate as possible. Three different functions based on the mean, medium and modulo were tested. Performance of these three functions for both  $F_x$  and  $F_y$  is shown in Figure 5.1.

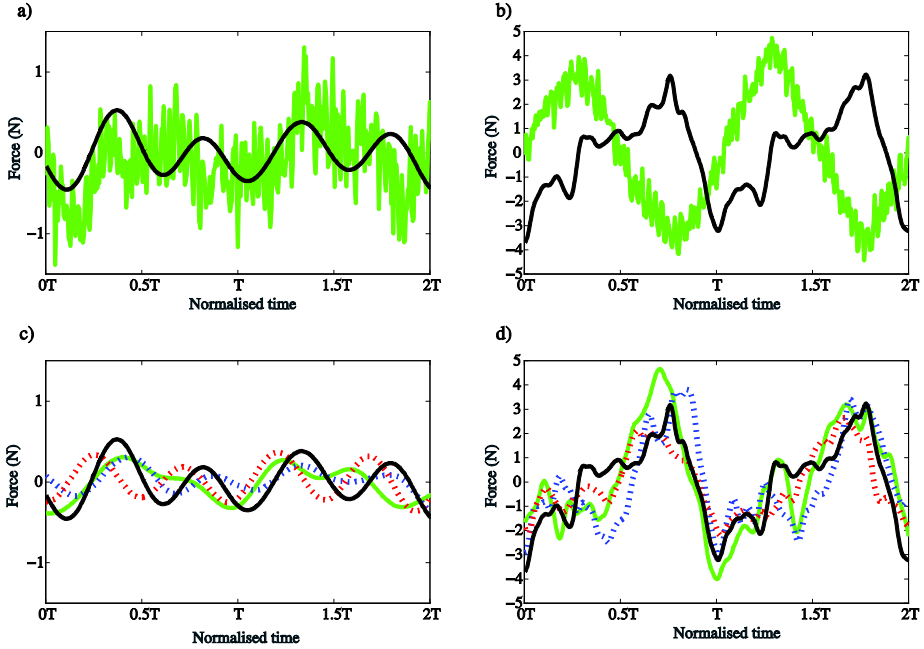


*Figure 5.1 Comparison of instantaneous force measurements, momentum flux estimates and general transfer functions for the turbulent flow experiment at 15 cm/s: a) measured streamwise forces ( $F_x$ , black) and the momentum deficit estimates ( $\Delta M_x$ , green) for two tail beat cycles; b) measured lateral forces ( $F_y$ , black) and the momentum deficit estimates ( $\Delta M_y$ , green); c) measured (solid black) streamwise forces compared with the mean (solid green), modulo (dashed red) and median (dashed blue) general transfer functions; and d) comparison of measured (solid black) and mean (solid green), modulo (dashed red) and median (dashed blue) lateral general transfer function results. The time scale is normalized to the tailbeat period ( $T$ ).*

### 5.3. Results

To evaluate the performance of the error reduction functions the time-averaged error over a 5 s period as a percentage of the mean force was determined. For a passive robotic fish these errors ranged from less than 10% in the streamwise direction up to 69% in the lateral direction. Results of general mean, median and modulo transfer functions to error reduction for the passive robot are given in Table 5.1 and for the actuated robot in Table 5.2.

Table 5.1 Error reduction for measurements with passive robot

Flow velocity (ms <sup>-1</sup> )	Median standard error reduction (%)		Mean standard error reduction (%)		Modulo standard error reduction (%)	
	$F_x$	$F_y$	$F_x$	$F_y$	$F_x$	$F_y$
0.10	36	47	18	42	22	53
0.15	20	49	20	31	47	61
0.20	18	59	14	50	26	68
0.25	45	77	16	70	63	83
0.30	33	75	42	42	41	83
0.35	49	77	24	69	69	81

Table 5.2 Error reduction for measurements with actuated robot

Flow velocity (ms <sup>-1</sup> )	Median standard error reduction (%)		Mean standard error reduction (%)		Modulo standard error reduction (%)	
	$F_x$	$F_y$	$F_x$	$F_y$	$F_x$	$F_y$
0.10	79	89	73	88	81	89
0.15	88	87	64	91	79	91
0.20	68	75	93	87	68	78

It is seen that for passive experiments, all transfer functions were able to reduce errors considerably, however the modulo transfer function performs better than the other two. It leads to the error reduction of 22% - 69% in for  $F_x$  and 53% - 83% for  $F_y$ . Same transfer functions were applied to the data from actuated fish experiments. In this case the performance of the three transfer functions is about the same as seen from Table 5.2 and Figure 5.1. In all cases the error reduction was between 64% to 93% for  $F_x$  and 75% to 91% for  $F_y$ .

#### 5.4. Conclusions and discussion

A new method was developed for calibrating instationary force estimates based on PIV measurements. A series of hydrodynamic experiments were conducted on a passive and moving robotic fish. Measurements were made simultaneously with a force plate and with PIV. By using the momentum deficit method, which relates the forces to the change of momentum in the flow, instantaneous forces were calculated from 2D velocity vectors. Furthermore in order to minimize the errors of indirect force measurements, transfer functions enabling robust and accurate force estimations from the change of momentum were created and evaluated. The use of transfer functions lead to an error reduction of up to 69% in the streamwise direction ( $F_x$ ) and up to 83% in the lateral direction ( $F_y$ ).

Large error/difference between the forces calculated from PIV data and directly measured forces have multiple sources:

- The momentum deficit method requires a defined control volume, a rectangular region around the object; uniform free stream velocity and pressure; negligible viscous dissipation along the boundaries; incompressibility and uniform flow density. If all these conditions hold, then the loss of linear momentum is equal to the difference in linear momentum and static pressure within and through the surface of the control volume. However it is not possible to simultaneously satisfy all these conditions [180].
- The linear momentum should be considered as non-conservative due to the exchange between linear and angular momentum [181].
- Conservation of linear momentum cannot be assumed in case of a single 2D velocity measurement of a 3D volume. Complex out of plane fluxes exist in the wake of a swimming fish as shown by Hanke and Bleckmann in 2004 by measuring the wake in six different layers sequentially [182].
- Flow in the flow tunnel is turbulent while the method assumes uniform freestream flow.
- A phase shift exists between the directly measured instantaneous force signals and the estimated ones. The primary source of the phase shift is caused by direct measurements being conducted at the center of mass of the body – where it is fixed to the rod connecting it to the force plate, while the PIV images are recorded behind the robotic fish tail. Thus the force plate detects the signal immediately when the fish robot moves whereas PIV records the result of the downstream wake.
- Motions of the body transfer to an acceleration of fluid increasing the apparent mass of the body – the added mass effect. Even if the robot is passive still a limited ability (mm) to move exists and since the whole body is not in the PIV field of view, it could generate errors.

From this list it is seen that calculating instantaneous forces affecting robotic fish body or created by it from the flow field after the tail is a complex task and often may not yield precise results as it is seen from the results in this chapter. However this chapter shows that it is indeed possible to considerably reduce the errors and phase shift by using calibrated transfer functions. Such correction is critical both in robotics and especially biology when experimenting with real fish as the motion of real fish is not as predictable and repeatable as in case of robots.

## **6 LATERAL LINE PROBE FOR STUDYING FISH PASSES**

The study of fluid-body interactions in terms of forces affecting fish shaped objects is followed by designing a new sensor system capable of measuring complex flows from the fish's point of view. This study helps to understand what fish feel when swimming in complex environments with high flow speed and turbulence. It also proposes a novel measurement system for evaluating human made fish passes. This chapter is based on the work published in [183], reprinted in APPENDIX D.

As described previously in Chapter 1.2.2, fish encounter many obstructions along their natural migration. The majority of the obstructions are caused by human activities. Today the restoration of fish population in rivers and the reestablishment of migration corridors is gaining in importance. A common way of remediating upstream migration is to build and monitor fish passes. Currently however, are few adequate means to design fish passes with repeatable success for a series of reasons.

Natural flows are a complex mixture of velocity, vorticity and pressure and field measurement devices including both propellers and ADVs, are meant for point measurements and provide low temporal resolution and thus do not allow for the estimation of turbulence metrics. Recent studies however show that fish have a strong response to local fluctuations in the velocity and vorticity fields in addition to general time averaged flow properties [184], [185]. Secondly, numerical modelling can be used to map time and depth averaged hydraulic parameters to known fish preferences (observed habitat usage), but do not take into account the fluid body interactions in fully turbulent flows.

This chapter describes experiments with a novel sensor system designed for evaluating fish passes and compares results from traditional measuring equipment. While conventional measurement techniques are designed to measure “the naked flow”, this device is specially designed to measure the interaction of flow and the streamlined, fish shaped body. It has higher temporal resolution and multiple pressure sensors placed laterally on its body, mimicking the lateral line – the sensing organ of real fish. This configuration enables the flow field measurement around the fish shaped body also due to multiple sensors. Also, high acquisition frequency allows calculations of various flow parameters. Due to the robust body design it is possible to insert the device easily into flow tunnels, rivers, creeks and fish passes. The lateral line probe (LLP) is described in detail in Chapter 2.3.4.

### **6.1. Materials and methods**

In order to test the LLP against commercially available flow measurement instruments two sets of experiments in two different flow tunnels were conducted.

The first set of experiments was conducted in an open top flow tunnel located in the University of Stuttgart, Germany. Details of the flow tunnel are given in Chapter 2.1.2. Water depth was fixed at 0.35 m, and flow speed varied from 0.1 – 1.2 ms<sup>-1</sup> with the increment of 0.1 ms<sup>-1</sup>. All measurements were repeated 10 times, data was logged at 250 Hz for 60 s for each experiment. To calibrate the velocity estimations of the LLP an ADV from Sontek Flowtracker (Sontek, Xylem, Inc., San Diego, USA) was fixed upstream of the fish shaped probe. Photo of the flow tunnel and experimental setup is shown in Figure 2.2.

The second set of experiments were conducted at a model fish pass located in Karlsruhe Institute of Technology, Germany. Further details are given in Chapter 2.1.3. Two different flow rates were measured, 0.130 m<sup>3</sup>s<sup>-1</sup> and 0.170 m<sup>3</sup>s<sup>-1</sup> with water column heights of 0.52 m and 0.56 m. The LLP was fixed to a Cartesian robot and at 60% of the water depth, 24 locations were measured in the basin. Same locations were measured with LDA (2D FlowExplorer System from Dantec Dynamics A/S, Skovlunde, Denmark) for validation. Drawing with the dimensions of the model fish pass is shown in Figure 2.3 along with a photo of the experimental setup.

## 6.2. Validation results

Velocity estimations of the probe are based on the Bernoulli equation (Equation 1.13) which applies the conservation of energy along a streamline to relate the pressure difference of stagnation point (nose sensor) and free stream static pressure (side sensor). The velocity is calculated the formula:

$$U = \sqrt{\frac{2\beta_{U,1}\Delta P_{0,1}}{\rho}}, \quad (6.1)$$

where  $U$  is the magnitude of three Cartesian velocity components,  $\beta_{U,1}$  is semi empirical correction factor depending on the body shape of the LLP and pressure sensors used,  $\Delta P_{0,1}$  is the pressure difference between the nose sensor and one side sensor and  $\rho$  is density of water.

Data from the first and the second set of experiments were used to develop a methodology allowing the usage of the LLP in field studies without the need of calibrating it for every measurement site. For that the mean amplitude estimations method [186] were chosen.

The comparison of velocity measurements with ADV and the LLP is shown in Figure 6.1. It is seen that the results are very similar, except the lowest flow speed 0.1 ms<sup>-1</sup> that was over estimated by the LLP system.

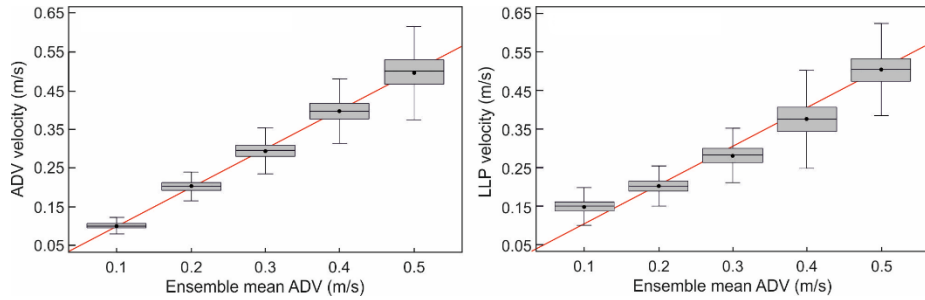


Figure 6.1 Comparison of the ADV (left) and LLP (right) velocity estimates using the mean amplitude method [183].

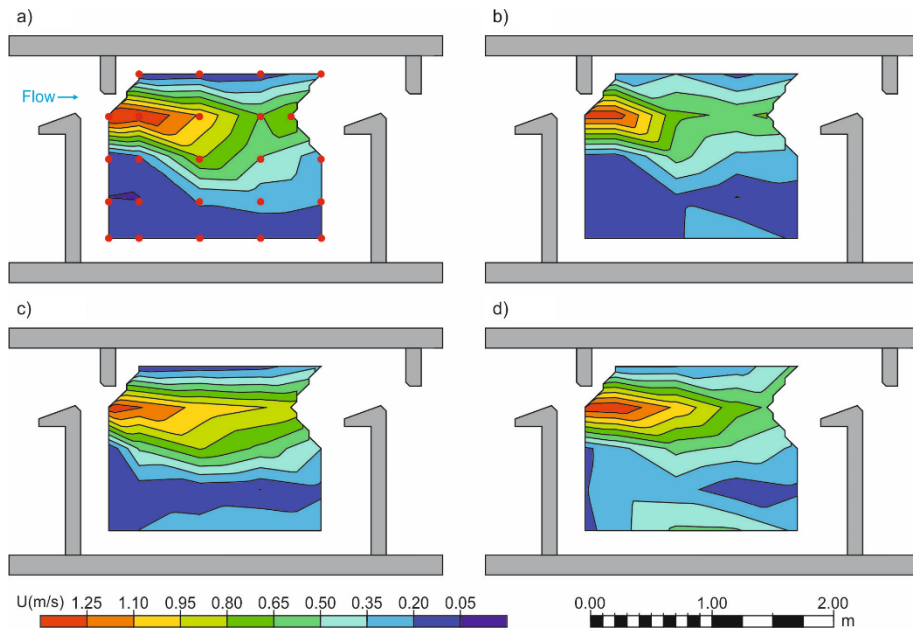


Figure 6.2 Flow map results for LLP, ADV measurements and CFD models: a) LLP flow map, measurement locations are marked with red dots; b) ADV measurements; c) RANS CFD model; d) LES (30s averaged) [183].

In Figure 6.2 a comparison of measurements with the LLP and ADV at the model vertical slot fish pass as well as comparison with CFD simulations with two different models is shown. It is seen that the results from the LLP are in good agreement with both the ADV measurements and simulations although they match more closely to ADV measurements. It is also seen that the velocities from the LLP are higher than from ADV especially in the flow jet from the slot. In

addition to velocity data similar conventional techniques, our LLP is capable of producing velocity and maps of the body oriented pressure distribution.

### 6.3. Initial evaluation of fishways

The LLP has been already tested in three real vertical slot fishways located in Tyrol, Austria in cooperation with the hydropower company TIWAG – Tiroler Wasserkraft AG. The aim was twofold: first, to test the LLP innatura and second, to measure fish passes, detect flow conditions and features and see if any irregularities can be detected. The data presented here is collected in April 2016, processing and analyzing is underway and here only preliminary results of one of the measured fish passes is presented.

The schematics of the fish pass located at the Pitze River near Wenns, Austria is shown in Figure 6.3, more details about the river and fish pass can be found in [187], [188].

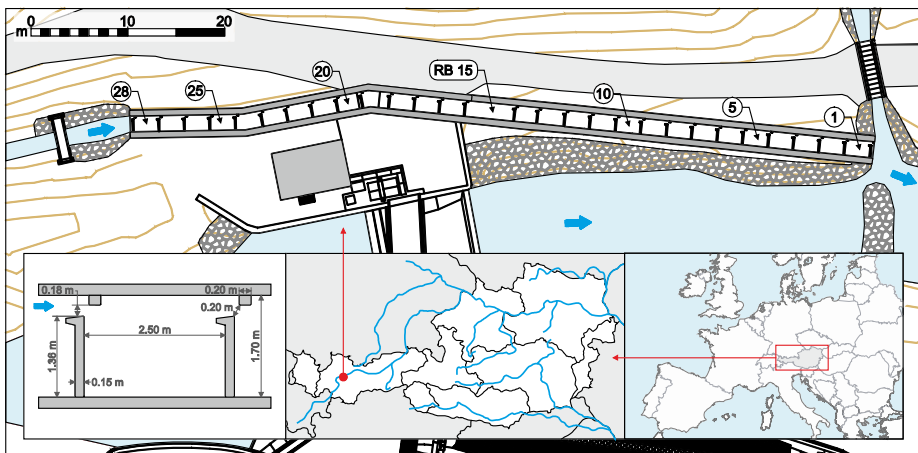


Figure 6.3 Plan and location of the vertical slot fish way at Pitze River, Austria [189].

In this fish pass all 28 slots and three reference basins (no. 7, 15 and 22) were measured. The LLP was mounted to the metal rod so that its height from the bottom was fixed to 40% of the total water depth. For the slot measurements an additional metal mounting system was used to hook the probe onto walls so that it remained rigidly fixed in the jet and directly facing the flow (see Figure 6.4). For basin measurements the probe was inserted along the central cross section and moved laterally with 0.2 m increments.

Preliminary results of slot measurements are shown in Figure 6.4c. The pressure fluctuations for each sensor are converted to a unique probability density function forming a hydrodynamic signature. Finally, the Kullback-Liebler Divergence

metric was used to determine difference of each measurement point from the mean signature. In Figure 6.4a and 6.4b mean values of slots along with the four most divergent ones are shown.

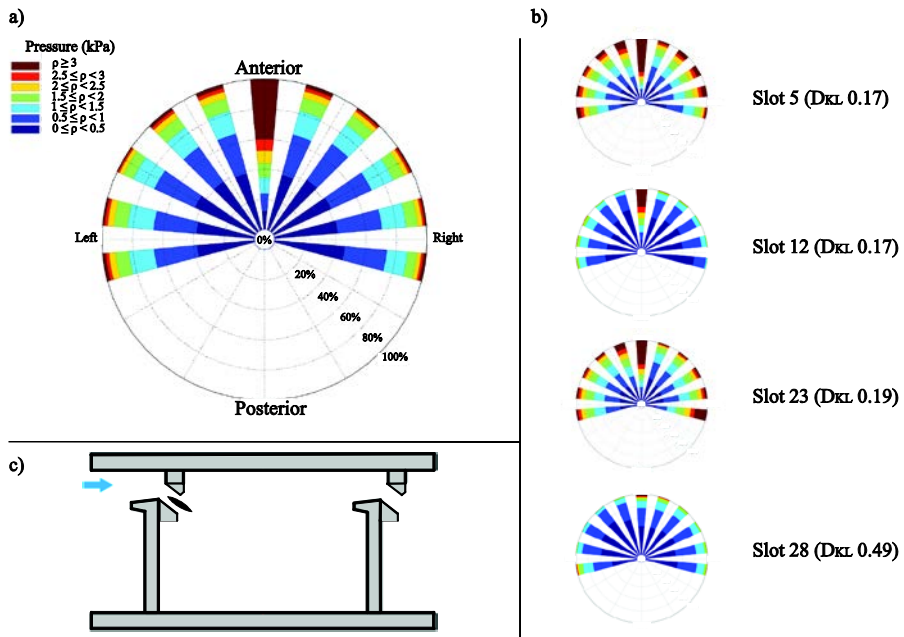


Figure 6.4 Hydrodynamic signatures of vertical slot fishway at the Pitze River, measured in April 2016, with the flow rate of  $350 \text{ ls}^{-1}$ , a) mean values of all slots; b) four most divergent slots detected; c) drawing of a fish pass basin, black fish shape indicates the location of the LLP, modifications made in 2015-2016 to slot configurations are marked with brown. Adopted from [189].

Exemplary measurement results for basins are shown in Figures 6.5. It should be noted that basins 7 and 22 have the standard geometric configuration common to the fish pass, whereas basin 15 is the resting basin with twice the length of the regular one. Three clearly distinguishable regions A, B and C were determined (see Figure 6.6) for regular basins and two for the resting basin. This agrees with previous research as A corresponds to the most typical region of fish passage, B is the jet region and region C is used by fish returning from upstream [90], [190].

350 l/s	A1	A2	A3	B4	B5	C6	C7	C8
7								
22								
	A1	A2	A3	A4	B5	B6	C7	B8
RB 15								

Figure 6.5 Basin cross sections signatures, in basins 7 and 22 and resting basin 22. Measured in April 2016 with the flow rate of  $350 \text{ l/s}^{-1}$  [189].

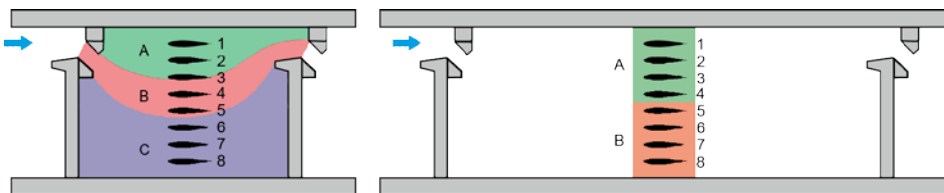


Figure 6.6 Left: regular basin cross section measurement spots and three distinguishable regions A, B and C in basins 7 and 15. Right: measurement spots in resting basin and two distinguishable flow regions A and B. Adopted from [189].

## 6.4. Conclusions and discussion

This chapter presented innatura experiments with a novel sensor system to study the interaction of flowing water and fish or fish shaped objects. The LLP was tested in a straight flow tunnel with different flow speeds from  $0.1 - 0.5 \text{ m/s}^{-1}$  and in a 1:1.6 scale laboratory model of a vertical slot fish pass. In both cases flow speed estimation results were compared to commonly used and commercially available systems – ADV for a flow tunnel data and LDA for fish way data. Data from our LLP and methodology were shown to agree with ADV and LDV. Considering that the LLP measures via fluid body interaction the probe enables to estimate flows from the perspective of fish, contrary to commonly used equipment that measures velocity or pressure at a single point. The LLP has also been tested innatura fish passes and is shown to be usable for detecting flow structures and regions for evaluating and comparing different parts of a fish pass and different fishways.

The LLP and its predecessors have also been used for developing flow measurement and classification methods in the works of Tuhtan [191], [192],

Fuentes-Perez [193], Strokina [194] and Fukuda [195]. Furthermore the lateral line sensor has successfully been used in robotics by Jezov [48] and Salumäe [169] to detect flow features. Muhammad also showed that the sensor system can be used for localization and navigation [196], [197].

In order to use the LLP to evaluate fish passes more work has to be done. This includes analyzing the placement of sensors on the body, body shape and improving algorithms that are used to calculate the velocity values, since the LLP systematically overestimated lower flow velocity values ( $< 10$  cm/s). Data processing algorithms can be further improved to produce new flow based metrics for classification. Future work will also include integrating force sensors enabling direct measurements of drag force, lateral forces and torque of the sensing body. In this way, the data acquired on field can be correlated to laboratory experiments conducted with the force plate described in Chapter 2.2.4.

## CONCLUSIONS

This thesis strove to further the development of bioinspired, energy efficient underwater robots by designing new flow sensing abilities. Four development studies were conducted to investigate how hydrodynamic forcing affecting fish shaped objects subject to turbulent flows. The experimental work within each study made use of the periodic turbulence generated by a Kàrmàn vortex street, direct force measurements, DPIV and pressure measurements.

The first study's aim was to investigate how hydrodynamic forces affect fish shaped robots in a vortex street depending on its position. It was proven that a region exists in a wake of an upstream object where a biomimetic robot can leverage to maximize its propulsion efficiency. In addition, it was found that regions leading to increased energy expenditure can also be clearly identified. The gained knowledge can be used in developing a control strategy for undulatory underwater vehicles in a complex turbulent flow. To distinguish these regions in real time without external force measurement systems this information has to be combined with sensors and algorithms capable of distinguishing complex flow features using artificial lateral line systems. Based on the described results and lateral line sensors a control for station holding for Prototype 3 in a vortex street has been developed by Salumäe and Kruusmaa [169].

The second study provided relations relating the robotic body length scale to the vortex street wake wavelength – it was found that the ratio of these scales influences the forces acting on a sensing body and showed how large fish can energetically benefit from the vortex street. It was found that the values of forces causing yaw and sway motions are driven by lateral forces and modulate torque as a function of increasing body length. As natural surroundings such as a river bed can change suddenly and act to change local flow patterns and since it is not feasible to construct a range of robots, each scaled for exploring a specific range of natural hydrodynamic conditions, it is necessary for the underwater robots to be able to adapt their control strategy on the local fluid-body interactions. Understanding of the forces affecting robots in turbulent flows together with previously described studies of the effects of robots position relative to the obstacle that is generating the turbulence can lead to the development of novel, more efficient underwater robots that are able to adopt to changing environment and flow conditions.

Traditionally in force measurements the object has to be physically fixed to the measurement device, this however restricts the characteristic motion of undulatory swimmers. Forces can be also estimated from PIV measurements but normally this method is sensitive to the control volume size and needs complex calibration to get accurate results. The third study outlined in Chapter 5 proposes a method to substantially improve the indirect force measurement of undulatory swimmers. Longitudinal and lateral forces were calculated from time-resolved velocity fields obtained using PIV measurements. A calibrated generalized linear transfer function was proposed to reduce the instantaneous force errors,

principally by eliminating the phase shift between the signals of directly measured forces at the center of mass of the robot and forces calculated from the velocity field behind the actuated fish robot's tail. This methodology provides a new way to develop and analyze the performance of underwater robots. Future works could apply the method to freely swimming objects in the test tank while the forces generated by them as well as hydrodynamic forces affecting them can be passively measured. Although the method is not as precise as fixing an object to the force gauge directly, it allows for free movement and thus makes possible direct and instantaneous measurements of undulatory swimming robots and live fish.

A novel bioinspired flow measurement device was introduced. Chapter 6 describes *innatura* experiments using a novel fish shaped measurement system. The sensor system was inspired from the lateral line organ of fish and is based on the array of pressure sensors. It was shown that velocity estimations from the LLP agree with conventional measurement equipment (ADV and LDV). This system is designed for measuring flows from "the fish's perspective" and makes it possible to generate pressure and flow maps surrounding a fish shaped body. The study was motivated by a lack of outdoor measurement devices capable of characterizing complex natural flows in rivers and in fish passage structures. Conventional techniques are able to measure the point wise velocity with low acquisition frequency, relative to the rapid motion of the water. Biologists and engineers designing fish passes therefore require a device that in addition to the flow speed, is capable of measuring biologically relevant flow parameters, especially the body oriented pressure distribution and turbulence metrics. The LLP and methodology introduced in Chapter 6 is a clear step in providing this data. In addition to the evaluation of fish passes, this data can also be interesting for biologists to understand the complex flows surrounding fish.

In conclusion this thesis showed that for biomimetic robots in turbulent flows favorable and costly regions exist and these can be detected with different techniques. Moreover an improved indirect force measurement technique and a novel flow field measurement device were introduced. Future work on turbulent fluid body interactions with bioinspired underwater robots should focus on combining novel sensor systems and building fish-like robots with improved swimming strategies to enhance performance. These robots can be used for monitoring the challenging conditions found in Nature. Future swimming robots could then master rocky river beds, helping us to study the turbulence in fish migration structures and aid in understanding the hydrodynamic preferences of fish in their natural environments.

## REFERENCES

- [1] J. Montgomery, S. Coombs, and M. Halstead, "Biology of the mechanosensory lateral line in fishes," *Rev. Fish Biol. Fish.*, vol. 5, no. 4, pp. 399–416, 1995.
- [2] J. C. Montgomery, S. Coombs, and C. F. Baker, "The mechanosensory lateral line system of the hypogean form of *Astyanax fasciatus*," *Environ. Biol. Fishes*, vol. 62, pp. 87–96, 2001.
- [3] J. Mogdans and H. Bleckmann, "Coping with flow: behavior, neurophysiology and modeling of the fish lateral line system," *Biol. Cybern.*, vol. 106, no. 11–12, pp. 1–16, Dec. 2012.
- [4] H. Bleckmann, "3-D-orientation with the octavolateralis system," *J. Physiol. Paris*, vol. 98, no. 1–3 SPEC. ISS., pp. 53–65, 2004.
- [5] C. C. Lindsey, "Form, function, and locomotory habits in fish," in *Fish Physiology Vol. VII Locomotion*, W. S. Hoar and D. J. Randall, Eds. New York: Academic press Inc, 1978, pp. 1–100.
- [6] C. Tudorache, P. Viaene, R. Blust, H. Vereecken, and G. De Boeck, "A comparison of swimming capacity and energy use in seven European freshwater fish species," *Ecol. Freshw. Fish*, vol. 17, no. 2, pp. 284–291, 2008.
- [7] K. Aarestrup, F. Okland, M. M. Hansen, D. Righton, P. Gargan, M. Castonguay, L. Bernatchez, P. Howey, H. Sparholt, M. I. Pedersen, and R. S. McKinley, "Oceanic spawning migration of the European eel (*Anguilla anguilla*)," *Science*, vol. 325, no. 5948, p. 1660, 2009.
- [8] V. van Ginneken, E. Antonissen, U. K. Müller, R. Booms, E. Eding, J. Verreth, and G. van den Thillart, "Eel migration to the Sargasso: remarkably high swimming efficiency and low energy costs.," *J. Exp. Biol.*, vol. 208, no. Pt 7, pp. 1329–1335, 2005.
- [9] DVWK, *Fish passes - Design, dimensions and monitoring*. Rome: Food and Agriculture Organization of the United Nations, 2002.
- [10] S. J. Cooke and S. G. Hinch, "Improving the reliability of fishway attraction and passage efficiency estimates to inform fishway engineering, science, and practice," *Ecol. Eng.*, vol. 58, pp. 123–132, 2013.
- [11] Y. Cai, S. Bi, and L. Zheng, "Design and Experiments of a Robotic Fish Imitating Cow-Nosed Ray," *J. Bionic Eng.*, vol. 7, no. 2, pp. 120–126, Jun. 2010.
- [12] C. Stefanini, S. Orofino, L. Manfredi, S. Mintchev, S. Marrazza, T. Assaf, L. Capantini, E. Sinibaldi, S. Grillner, P. Wallén, and P. Dario, "A novel autonomous, bioinspired swimming robot developed by neuroscientists and bioengineers.," *Bioinspir. Biomim.*, vol. 7, no. 2, p. 25001, Jun. 2012.

- [13] W.-S. Chu, K.-T. Lee, S.-H. Song, M.-W. Han, J.-Y. Lee, H.-S. Kim, M.-S. Kim, Y.-J. Park, K.-J. Cho, and S.-H. Ahn, "Review of biomimetic underwater robots using smart actuators," *Int. J. Precis. Eng. Manuf.*, vol. 13, no. 7, pp. 1281–1292, Jul. 2012.
- [14] H. El Daou, T. Salumae, G. Toming, and M. Kruusmaa, "A bio-inspired compliant robotic fish: Design and experiments," in *2012 IEEE International Conference on Robotics and Automation*, 2012, pp. 5340–5345.
- [15] A. Crespi, K. Karakasiliotis, A. Guignard, and A. J. Ijspeert, "Salamandra Robotica II: An Amphibious Robot to Study Salamander-Like Swimming and Walking Gaits," *IEEE Trans. Robot.*, vol. 29, no. 2, pp. 308–320, Apr. 2013.
- [16] Y. S. Ryuh, G. H. Yang, J. Liu, and H. Hu, "A school of robotic fish for mariculture monitoring in the sea coast," *J. Bionic Eng.*, vol. 12, no. 1, pp. 37–46, 2015.
- [17] L. Devries and D. a Paley, "Observability-based Optimization for Flow Sensing and Control of an Underwater Vehicle in a Uniform Flowfield," in *American Control Conference, Washington, DC, USA*, 2013, pp. 1386–1391.
- [18] M. Kruusmaa, P. Fiorini, W. Megill, M. De Vittorio, O. Akanyeti, F. Visentin, L. Chambers, H. El Daou, M. C. Fiazza, J. Jezov, M. Listak, L. Rossi, T. Salumae, G. Toming, R. Venturelli, D. S. Jung, J. Brown, F. Rizzi, A. Qualtieri, J. L. Maud, and A. Liszewski, "FILOSE for svenning: A flow sensing bioinspired robot," *IEEE Robot. Autom. Mag.*, vol. 21, no. 3, pp. 51–62, 2014.
- [19] J. S. Riedel, "Shallow water stationkeeping of an autonomous underwater vehicle:\nthe experimental results of a disturbance compensation controller," *Ocean. 2000 MTS/IEEE Conf. Exhib. Conf. Proc. (Cat. No.00CH37158)*, vol. 2, pp. 1017–1024, 2000.
- [20] C. L. Gerstner and P. W. Webb, "The station-holding performance of the plaice *Pleuronectes platessa* on artificial substratum ripples," *Can. J. Zool.*, vol. 76, no. 2, pp. 260–268, 1998.
- [21] P. W. Webb, "Entrainment by river chub *Nocomis micropogon* and smallmouth bass *Micropterus dolomieu* on cylinders," *J. Exp. Biol.*, vol. 201, pp. 2403–2412, 1998.
- [22] J. C. Liao, "A review of fish swimming mechanics and behaviour in altered flows," *Philos. Trans. R. Soc. Lond. B. Biol. Sci.*, vol. 362, no. 1487, pp. 1973–93, Nov. 2007.
- [23] D. H. Evans and J. B. Claiborne, *The Physiology of Fishes, Third Edition*, Third Edit. CRC Press, 2006.

- [24] M. Sfakiotakis, D. M. Lane, and J. B. C. Davies, "Review of fish swimming modes for aquatic locomotion," *IEEE J. Ocean. Eng.*, vol. 24, no. 2, pp. 237–252, Apr. 1999.
- [25] C. M. Breder, "The locomotion of fishes," *Zoologica*, vol. 4, pp. 159–256, 1926.
- [26] J. J. Magnuson, "Locomotion by scombrid fishes: Hydromechanics, morphology and behavior," in *Fish Physiology Vol. VII Locomotion*, W. S. Hoar and D. J. Randall, Eds. New York: Academic press Inc, 1978, pp. 239–313.
- [27] T. Y. Wu, "Mathematical biofluidynamics and mechanophysiology of fish locomotion," *Math. Methods Appl. Sci.*, vol. 24, pp. 1541–1564, 2001.
- [28] A. P. Maertens, M. S. Triantafyllou, and D. K. P. Yue, "Efficiency of fish propulsion," *Bioinspir. Biomim.*, vol. 10, no. 4, p. 46013, 2015.
- [29] E. J. Anderson, W. R. McGillis, and M. a Grosenbaugh, "The boundary layer of swimming fish.," *J. Exp. Biol.*, vol. 204, no. Pt 1, pp. 81–102, Jan. 2001.
- [30] M. J. Lighthill, "Aquatic animal propulsion of high hydromechanical efficiency," *J. Fluid Mech.*, vol. 44, no. 2, p. 265, 1970.
- [31] J. J. Videler, *Fish Swimming*. London: Chapman & Hall, 1993.
- [32] B. Y. R. Bainbridge, "The speed of swimming of fish as related to size and the frequency and amplitude of the tail beat," *J. Exp. Biol.*, vol. 35, pp. 109–133, 1958.
- [33] J. R. Hunter, "Sustained speed of jack mackerel, *Trachurus symmetricus*," *Fish. Bull.*, vol. 69, no. 2, pp. 267–271, 1971.
- [34] B. C. Jayne and G. V. Lauder, "Speed effects on midline kinematics during steady undulatory swimming of largemouth bass, *Micropterus salmoides*," *J. Exp. Biol. Biol.*, vol. 198, pp. 585–602, Jan. 1995.
- [35] P. Webb, P. KostECKI, and E. Stevens, "The effect of size and swimming speed on locomotor kinematics of rainbow trout," *J. Exp. Biol.*, vol. 109, pp. 77–95, 1984.
- [36] J. S. Nelson, *Fishes of the World*, First. New Jersey: Wiley-Blackwell, 1976.
- [37] J. Lythgoe and G. Lythgoe, *Fishes of the Sea: Coastal Waters of the British Isles, Northern Europe and the Mediterranean*. London: Blandford Press, 1971.
- [38] J. Lythgoe and G. Lythgoe, *Fishes of the Sea: The North Atlantic and Mediterranean*. Cambridge: MIT Press, 1991.

- [39] U. Müller, B. Heuvel, E. Stams, and J. Videler, “Fish foot prints: morphology and energetics of the wake behind a continuously swimming mullet (*Chelon labrosus* Risso).,” *J. Exp. Biol.*, vol. 200, pp. 2893–906, 1997.
- [40] D. G. M. Watson, *Practical ship design*, Vol. 1. Elsevier Ltd, 1998.
- [41] C. L. Gerstner, “Use of substratum ripples for flow refuging by Atlantic cod, *Gadus morhua*,” *Environ. Biol. Fishes*, vol. 51, pp. 455–460, 1998.
- [42] P. Webb, “Entrainment by river chub *nocomis micropogon* and smallmouth bass *micropterus dolomieu* on cylinders,” *J. Exp. Biol.*, vol. 201 (Pt 16), pp. 2403–12, Aug. 1998.
- [43] A. Przybilla, S. Kunze, A. Rudert, H. Bleckmann, and C. Brücker, “Entraining in trout: a behavioural and hydrodynamic analysis,” *J. Exp. Biol.*, vol. 213, no. Pt 17, pp. 2976–2986, Sep. 2010.
- [44] M. M. Zdravkovich, *Flow Around Circular Cylinders: a Comprehensive Guide Through Flow Phenomena, Experiments, Applications, Mathematical Models, and Computer simulations*. Oxford: Oxford University Press, 1997.
- [45] R. D. Blevins, *Flow-Induced Vibration*, Vol 1. New York: Van Nostrand Reinhold Co, 1977.
- [46] “Wikipedia, Theodore von Kàrmàn.” [Online]. Available: [http://en.wikipedia.org/wiki/Theodore\\_von\\_Kàrmàn](http://en.wikipedia.org/wiki/Theodore_von_Kàrmàn). [Accessed: 12-Mar-2015].
- [47] O. Akanyeti, R. Venturelli, F. Visentin, L. Chambers, W. M. Megill, and P. Fiorini, “What information do Kàrmàn streets offer to flow sensing?,” *Bioinspir. Biomim.*, vol. 6, no. 3, p. 036001 1-12, Sep. 2011.
- [48] J. Ježov, O. Akanyeti, L. D. Chambers, and M. Kruusmaa, “Sensing oscillations in unsteady flow for better robotic swimming efficiency,” in *Conference Proceedings - IEEE International Conference on Systems, Man and Cybernetics*, 2012, pp. 91–96.
- [49] M. S. Triantafyllou, G. S. Triantafyllou, and D. K. P. Yue, “Hydrodynamics of Fishlike Swimming,” *J. Fluid Mech.*, vol. 32, pp. 33–53, 2000.
- [50] M. S. Triantafyllou, a H. Techet, Q. Zhu, D. N. Beal, F. S. Hover, and D. K. P. Yue, “Vorticity Control in Fish-like Propulsion and Maneuvering,” *Integr. Comp. Biol.*, vol. 42, no. 5, pp. 1026–1031, Nov. 2002.
- [51] J. C. Liao, D. N. Beal, G. V Lauder, and M. S. Triantafyllou, “The Kàrmàn gait: novel body kinematics of rainbow trout swimming in a vortex street,” *J. Exp. Biol.*, vol. 206, no. 6, pp. 1059–1073, Mar. 2003.
- [52] J. C. Liao, D. N. Beal, G. V Lauder, and M. S. Triantafyllou, “Fish

- exploiting vortices decrease muscle activity.,” *Science*, vol. 302, no. 5650, pp. 1566–1569, Nov. 2003.
- [53] C. L. Cook and D. J. Coughlin, “Rainbow trout *Oncorhynchus mykiss* consume less energy when swimming near obstructions.,” *J. Fish Biol.*, vol. 77, no. 7, pp. 1716–23, Nov. 2010.
- [54] M. Taguchi and J. C. Liao, “Rainbow trout consume less oxygen in turbulence: the energetics of swimming behaviors at different speeds.,” *J. Exp. Biol.*, vol. 214, pp. 1428–1436, May 2011.
- [55] B. P. Chagnaud, H. Bleckmann, and M. H. Hofmann, “Kármán vortex street detection by the lateral line,” *J. Comp. Physiol. A*, vol. 193, no. 7, pp. 753–63, Jul. 2007.
- [56] J. C. Liao, “The role of the lateral line and vision on body kinematics and hydrodynamic preference of rainbow trout in turbulent flow.,” *J. Exp. Biol.*, vol. 209, no. Pt 20, pp. 4077–4090, Oct. 2006.
- [57] J. C. Liao, “Neuromuscular control of trout swimming in a vortex street: implications for energy economy during the Karman gait,” *J. Exp. Biol.*, vol. 207, pp. 3495–506, Sep. 2004.
- [58] D. N. Beal, F. S. Hover, M. S. Triantafyllou, J. C. Liao, and G. V. Lauder, “Passive propulsion in vortex wakes,” *J. Fluid Mech.*, vol. 549, no. 1, p. 385, Feb. 2006.
- [59] R. Gopalkrishnan, M. S. Triantafyllou, G. S. Triantafyllou, and D. Barrett, “Active vorticity control in a shear flow using a flapping foil,” *J. Fluid Mech.*, vol. 274, p. 1, 1994.
- [60] S. Wang, L. Jia, and X. Yin, “Kinematics and forces of a flexible body in Karman vortex street,” *Chinese Sci. Bull.*, vol. 54, no. 4, pp. 556–561, Feb. 2009.
- [61] K. Streitlien, “Extracting Energy from Unsteady Flows through Vortex Control,” 1994.
- [62] A. B. Phillips, J. I. R. Blake, B. Smith, S. W. Boyd, and G. Griffiths, “Nature in engineering for monitoring the oceans: towards a bio-inspired flexible AUV operating in an unsteady flow,” *Proc. Inst. Mech. Eng. Part M J. Eng. Marit. Environ.*, vol. 224, no. 4, pp. 267–278, Nov. 2010.
- [63] C. Brönmark, K. Hulthén, P. A. Nilsson, C. Skov, L.-A. Hansson, J. Brodersen, and B. B. Chapman, “There and back again: migration in freshwater fishes,” *Can. J. Zool.*, vol. 13, no. June, pp. 467–479, 2013.
- [64] J. W. Banks, “A Review of the Literature on the Upstream Migration of Adult Salmonids,” *J. Fish Biol.*, vol. 1, pp. 85–136, 1969.
- [65] M. C. Lucas and E. Baras, *Migration of Freshwater Fishes*. Oxford: Blackwell Science Ltd, 2001.

- [66] A. P. Hendry, T. Bohlin, B. Jonsson, and O. K. Berg, "To sea or not to sea: Anadromy versus non-anadromy in salmonids," in *Evolution Illuminated: salmon and their relatives*, A. P. Hendry and S. C. Stearns, Eds. Oxford Univ. Press., 2004, pp. 92–125.
- [67] T. Mehner, "Diel vertical migration of freshwater fishes - proximate triggers, ultimate causes and research perspectives," *Freshw. Biol.*, vol. 57, pp. 1342–1359, 2012.
- [68] Z. Maciej Gliwicz, J. Slon, and I. Szykarczyk, "Trading safety for food: Evidence from gut contents in roach and bleak captured at different distances offshore from their daytime littoral refuge," *Freshw. Biol.*, vol. 51, pp. 823–839, 2006.
- [69] A. Klemetsen, P.-A. Amundsen, J. B. Dempson, B. Jonsson, N. Jonsson, M. F. O'Connell, and E. Mortensen, "Atlantic salmon *Salmo salar* L., brown trout *Salmo trutta* L. and Arctic charr *Salvelinus alpinus* (L.): a review of aspects of their life histories," *Ecol. Freshw. Fish*, vol. 12, no. 1, pp. 1–59, 2003.
- [70] G. T. Crossin, S. G. Hinch, a. P. Farrell, D. a. Higgs, a. G. Lotto, J. D. Oakes, and M. C. Healey, "Energetics and morphology of sockeye salmon: Effects of upriver migratory distance and elevation," *J. Fish Biol.*, vol. 65, no. 3, pp. 788–810, 2004.
- [71] S. J. Cooke, S. G. Hinch, A. P. Farrell, M. F. Lapointe, S. R. M. Jones, J. S. Macdonald, D. a. Patterson, M. C. Healey, and G. Van Der Kraak, "Abnormal Migration Timing and High en route Mortality of Sockeye Salmon in the Fraser River, British Columbia," *Fisheries*, vol. 29, no. 2, pp. 22–33, 2004.
- [72] R. Brown and D. Geist, "Determination of swimming speeds and energetic demands of upriver migrating fall chinook salmon (*Oncorhynchus tshawytscha*) in the Klickitat River," Washington, 2002.
- [73] M. G. Mesa and C. D. Magie, "Evaluation of energy expenditure in adult spring Chinook salmon migrating upstream in the Columbia River Basin: An assessment based on sequential proximate analysis," *River Res. Appl.*, vol. 22, pp. 1085–1095, 2006.
- [74] Z. L. Penney and C. M. Moffitt, "Proximate Composition and Energy Density of Stream-Maturing Adult Steelhead during Upstream Migration, Sexual Maturity, and Kelt Emigration," *Trans. Am. Fish. Soc.*, vol. 143, no. 2, pp. 399–413, 2014.
- [75] S. J. Cooke, E. B. Thorstad, and S. G. Hinch, "Activity and energetics of free-swimming fish: Insights from electromyogram telemetry," *Fish Fish.*, vol. 5, no. 1, pp. 21–52, 2004.
- [76] E. C. Enders, C. J. Pennell, R. K. Booth, and D. A. Scruton, "Energetics related to upstream migration of Atlantic salmon in vertical slot

- fishways,” St. John’s NL, 2008.
- [77] S. G. Hinch, E. M. Standen, M. C. Healey, and A. P. Farrell, “Swimming patterns and behaviour of upriver-migrating adult pink (*Oncorhynchus gorbusha*) and sockeye (*O. nerka*) salmon as assessed by EMG telemetry in the Fraser River, British Columbia, Canada,” *Hydrobiologia*, vol. 483, pp. 147–160, 2002.
- [78] Y. Makiguchi, H. Nii, K. Nakao, and H. Ueda, “Upstream migration of adult chum and pink salmon in the Shibetsu River,” *Hydrobiologia*, vol. 582, no. 1, pp. 43–54, 2007.
- [79] P. S. Rand, S. G. Hinch, J. Morrison, M. G. G. Foreman, M. J. MacNutt, J. S. Macdonald, M. C. Healey, a. P. Farrell, and D. a. Higgs, “Effects of River Discharge, Temperature, and Future Climates on Energetics and Mortality of Adult Migrating Fraser River Sockeye Salmon,” *Trans. Am. Fish. Soc.*, vol. 135, no. 3, pp. 655–667, 2006.
- [80] S. G. Hinch and P. S. Rand, “Swim speeds and energy use of upriver-migrating sockeye salmon (*Oncorhynchus nerka*): role of local environment and fish characteristics,” *Can. J. Fish. Aquat. Sci.*, vol. 55, no. 8, pp. 1821–1831, 1998.
- [81] S. G. Hinch and P. S. Rand, “Optimal swimming speeds and forward-assisted propulsion: energy-conserving behaviours of upriver-migrating adult salmon,” *Can. J. Fish. Aquat. Sci.*, vol. 57, no. 12, pp. 2470–2478, 2000.
- [82] K. Aarestrup, M. Lucas, and J. Hansen, “Efficiency of a nature-like bypass channel for sea trout (*Salmo trutta*) ascending a small Danish stream studied by PIT telemetry,” *Ecol. Freshw. Fish*, vol. 12, no. 3, pp. 160–168, 2003.
- [83] T. T. Rodríguez, J. P. Agudo, L. P. Mosquera, and E. P. González, “Evaluating vertical-slot fishway designs in terms of fish swimming capabilities,” *Ecol. Eng.*, vol. 27, no. 1, pp. 37–48, 2006.
- [84] J. M. Santos, M. T. Ferreira, F. N. Godinho, and J. Bochechas, “Efficacy of a nature-like bypass channel in a Portuguese lowland river,” *J. Appl. Ichthyol.*, vol. 21, no. 5, pp. 381–388, 2005.
- [85] E. O. Calles and L. a. Greenberg, “Evaluation of nature-like fishways for re-establishing connectivity in fragmented salmonid populations in the River Em??n,” *River Res. Appl.*, vol. 21, no. 9, pp. 951–960, 2005.
- [86] A. T. Silva, J. M. Santos, M. T. Ferreira, A. N. Pinheiro, and C. Katopodis, “Effects of water velocity and turbulence on the behaviour of Iberian barbel (*Luciobarbus bocagei*, Steindachner 1864) in an experimental pool-type fishway,” *River Res. Appl.*, vol. 27, no. 3, pp. 360–373, 2011.
- [87] J. M. Santos, A. Silva, C. Katopodis, P. Pinheiro, A. Pinheiro, J.

- Bochechas, and M. T. Ferreira, "Ecohydraulics of pool-type fishways: Getting past the barriers," *Ecol. Eng.*, vol. 48, pp. 38–50, 2012.
- [88] M. Liu, N. Rajaratnam, and D. Z. Zhu, "Mean Flow and Turbulence Structure in Vertical Slot Fishways," *J. Hydraul. Eng.*, vol. 132, no. 8, pp. 765–777, 2006.
- [89] M. Mermudez, A. Rodriguez, L. Cea, F. Morcillo, M. Castillo, and E. Aramburu, "Implications of Fish Behavior for Vertical Slot Fishways Design," in *International Symposium on Ecohydraulics*, 2012.
- [90] R. W. Wang, L. David, and M. Larinier, "Contribution of experimental fluid mechanics to the design of vertical slot fish passes," *Knowl. Manag. Aquat. Ecosyst.*, vol. 2, no. 396, 2010.
- [91] N. Rajaratnam and C. Katopodis, "Hydraulics of Denil Fishways," *J. Hydraul. Eng.*, vol. 110, no. 9, pp. 1219–1233, 1984.
- [92] M. Odeh, "Discharge Rating Equation and Hydraulic Characteristics of Standard Denil Fishways," *J. Hydraul. Eng.*, vol. 129, no. 5, pp. 341–348, 2003.
- [93] M. Larinier, "Upstream and Downstream Fish Passage Experience in France," in *Fish Migration and Fish Bypasses*, M. Jungwirth, S. Schmutz, and S. Weiss, Eds. Blackwell Science Ltd: Fishing News Books, 1998, pp. 127–145.
- [94] M. Larinier, M. Chanseau, F. Bau, and O. Croze, "The use of radio telemetry for optimizing fish pass design," in *Aquatic Telemetry: Advances and Applications: Proceedings of the Fifth Conference on Fish Telemetry*, 2005, pp. 53–60.
- [95] E. O. Calles and L. a. Greenberg, "The use of two nature-like fishways by some fish species in the Swedish River Em??n," *Ecol. Freshw. Fish*, vol. 16, no. 2, pp. 183–190, 2007.
- [96] C. M. Bunt, T. Castro-Santos, and a. Haro, "Performance of fish passage structures at upstream barriers to migration," *River Res. Appl.*, vol. 28, no. 4, pp. 457–478, 2012.
- [97] M. L. Moser, P. a. Ocker, L. C. Stuehrenberg, and T. C. Bjornn, "Passage Efficiency of Adult Pacific Lampreys at Hydropower Dams on the Lower Columbia River, USA," *Trans. Am. Fish. Soc.*, vol. 131, no. 5, pp. 956–965, 2002.
- [98] W. A. Wakeham, M. J. Assael, A. Marmur, J. D. Coninck, T. D. Blake, S. A. Theron, and E. Zussman, "Material Properties: Measurement and Data," in *Springer Handbook of Experimental Fluid Mechanics*, C. Tropea, A. Yarin, and J. F. Foss, Eds. Berlin: Springer-Verlag, 2007, pp. 85–178.
- [99] B. J. McKeon and R. H. Engler, "Pressure Measurement Systems," in

- Springer Handbook of Experimental Fluid Mechanics*, C. Tropea, A. Yarin, and J. F. Foss, Eds. Berlin: Springer-Verlag, 2007, pp. 179–214.
- [100] B. J. McKeon, G. Comte-Bellot, J. F. Foss, J. Westerweel, F. Scarano, C. Tropea, J. F. Meyers, J. W. Lee, A. A. Cavone, R. Schodl, M. M. Koochesfahani, D. G. Nocera, Y. Andreopoulos, W. J. A. Dahm, J. A. Mullin, J. M. Wallace, P. V Vukoslavcevic, S. C. Morris, E. R. Pardyjak, and A. Cuerva, “Velocity, Vorticity, and Mach Number,” in *Springer Handbook of Experimental Fluid Mechanics*, C. Tropea, A. Yarin, and J. F. Foss, Eds. Berlin: Springer-Verlag, 2007, pp. 215–472.
- [101] G. Voulgaris and J. H. Trowbridge, “Evaluation of the Acoustic Doppler Velocimeter (ADV) for Turbulence Measurements\*,” *J. Atmos. Ocean. Technol.*, vol. 15, no. 1, pp. 272–289, 1998.
- [102] H. Chanson, “Acoustic Doppler Velocimetry ( Adv ) in the Field and in Laboratory: Practical Experiences,” in *International Meeting on Measurements and Hydraulics of Sewers*, 2008, pp. 49–66.
- [103] R. J. Adrian, “Particle-image techniques for experimental fluid mechanics,” *Annu. Rev. Fluid Mech.*, vol. 23, pp. 261–304, 1991.
- [104] N. C. Kraus, A. Lohrmann, and R. Cabrera, “New Acoustic Meter for Measuring 3D Laboratory Flows,” *J. Hydraul. Eng.*, vol. 120, no. 3, pp. 406–412, 1994.
- [105] TSI Inc., “TSI Incorporated - LDV Systems,” 2016. [Online]. Available: <http://www.tsi.com/ldv-systems/>. [Accessed: 12-Sep-2016].
- [106] M. Mchenry, C. Pell, and J. Jr, “Mechanical control of swimming speed: stiffness and axial wave form in undulating fish models,” *J. Exp. Biol.*, vol. 198, no. Pt 11, pp. 2293–305, Jan. 1995.
- [107] D. S. Barrett, M. S. Triantafyllou, D. K. P. Yue, M. a. Grosenbaugh, and M. J. Wolfgang, “Drag reduction in fish-like locomotion,” *Journal of Fluid Mechanics*, vol. 392, pp. 183–212, 1999.
- [108] P. V. y Alvarado, K. Youcef-Toumi, P. Valdivia Y Alvarado, and K. Youcef-Toumi, “Performance of Machines with Flexible Bodies Designed for Biomimetic Locomotion in Liquid Environments,” in *Proceedings of the 2005 IEEE International Conference on Robotics and Automation*, 2005, vol. 2005, no. April, pp. 3324–3329.
- [109] S. Kobayashi, T. Ozaki, M. Nakabayashi, H. Morikawa, and A. Itoh, “Bioinspired aquatic propulsion mechanisms with real-time variable apparent stiffness fins,” *2006 IEEE Int. Conf. Robot. Biomimetics, ROBIO 2006*, pp. 463–467, 2006.
- [110] G. V Lauder, E. J. Anderson, J. Tangorra, and P. G. a Madden, “Fish biorobotics: kinematics and hydrodynamics of self-propulsion.,” *J. Exp. Biol.*, vol. 210, no. Pt 16, pp. 2767–2780, Aug. 2007.

- [111] O. M. Curet, N. a Patankar, G. V Lauder, and M. a MacIver, “Mechanical properties of a bio-inspired robotic knifefish with an undulatory propulsor.,” *Bioinspir. Biomim.*, vol. 6, no. 2, p. 26004, Jun. 2011.
- [112] K. M. Collins, J. C. Brown, R. R. Ladd, L. D. Chambers, A. Bowyer, and W. M. Megill, “Variable stroke timing of rubber fins’ duty cycle improves force,” *IEEE 15th Int. Conf. Adv. Robot. New Boundaries Robot. ICAR 2011*, pp. 613–618, Jun. 2011.
- [113] M. Kruusmaa, G. Toming, T. Salumäe, J. Ježov, and A. Ernits, “Swimming speed control and on-board flow sensing of an artificial trout,” in *Proceedings - IEEE International Conference on Robotics and Automation*, 2011, pp. 1791–1796.
- [114] T. Salumäe and M. Kruusmaa, “A flexible fin with bio-inspired stiffness profile and geometry,” *J. Bionic Eng.*, vol. 8, no. 4, pp. 418–428, Dec. 2011.
- [115] H. El Daou, T. Salumäe, A. Ristolainen, G. Toming, M. Listak, and M. Kruusmaa, “A bio-mimetic design and control of a fish-like robot using compliant structures,” *IEEE 15th Int. Conf. Adv. Robot. New Boundaries Robot. ICAR 2011*, pp. 563–568, 2011.
- [116] W. Merzkirch, “Flow Visualization,” in *Springer Handbook of Experimental Fluid Mechanics*, C. Tropea, A. L. Yarin, and J. F. Foss, Eds. Berlin: Springer-Verlag, 2007, pp. 857–870.
- [117] M. Raffel, C. E. Willert, S. T. Wereley, and J. Kompenhans, *Particle Image Velocimetry A Practical Guide*, Second Edi. Berlin, Heidelberg, New York: Springer-Verlag, 2007.
- [118] R. J. Adrian, “Twenty years of particle image velocimetry,” *Exp. Fluids*, vol. 39, no. 2, pp. 159–169, Jul. 2005.
- [119] M. Jahanmiri, “Particle Image Velocimetry: Fundamentals and Its Applications,” Göteborg, Sweden, 2011.
- [120] R. J. Adrian, “Multi-point optical measurements of simultaneous vectors in unsteady flow—a review,” *Int. J. Heat Fluid Flow*, vol. 7, no. 2, pp. 127–145, 1986.
- [121] J. Kompenhans and J. Reichmuth, “Particle imaging velocimetry in a low turbulent wind tunnel and other flow facilities,” in *IEEE Montech’86 conference, Montreal, Canada, October 1986. AGARD conference proceedings no. 399*, 1986, p. paper 35.
- [122] L. Zhao, Y. Zhang, X. Wang, G. L. Riskowski, and L. L. Christianson, “Measurement of two-dimensional air velocities in a full-scale room using particle image velocimetry,” *ASHRAE Trans.*, vol. 107 PART 2, pp. 434–444, 2001.
- [123] N. A. Buchmann, C. Willert, and J. Soria, “Pulsed, High-Power Led

- Volume Illumination for Tomographic Particle Image Velocimetry,” in *17th Australasian Fluid Mechanics Conference*, 2010, no. December.
- [124] T. Watamura, Y. Tasaka, and Y. Murai, “LCD-projector-based 3D color PTV,” *Exp. Therm. Fluid Sci.*, vol. 47, pp. 68–80, 2013.
- [125] L. Bertuccioli, G. I. Roth, J. Katz, and T. R. Osborn, “A submersible particle image velocimetry system for turbulence measurements in the bottom boundary layer,” *J. Atmos. Ocean. Technol.*, vol. 16, no. 11 PART 1, pp. 1635–1646, 1999.
- [126] W. L. Snow and O. A. Morris, *Investigation of Light Source and Scattering Medium Related to Vapor-Screen Flow Visualization in a Supersonic Wind Tunnel*. Washington, D.C.: NASA TM 86290, 1984.
- [127] G. Toming, “Development and characterization of a hydrodynamic test bed and a digital particle image velocimetry system,” University of Tartu, 2010.
- [128] J. Westerweel, “Digital particle image velocimetry: Theory and Application,” 1993.
- [129] A. Melling, “Tracer particles and seeding for particle image velocimetry,” *Meas. Sci. Technol.*, vol. 8, no. 12, pp. 1406–1416, 1997.
- [130] I. Grant, “Particle image velocimetry: A review,” *Proc. Inst. Mech. Eng. Part C-Journal Mech. Eng. Sci.*, vol. 211, no. 1, pp. 55–76, 1997.
- [131] S. T. Wereley and C. D. Meinhart, “Recent Advances in Micro-Particle Image Velocimetry,” *Annu. Rev. Fluid Mech.*, vol. 42, no. 1, pp. 557–576, Jan. 2010.
- [132] H. C. van de Hulst, *Light Scattering by Small Particles*. New York: Dover Publications, Inc, 1981.
- [133] M. Kowalczyk, “Laser speckle velocimetry,” in *SPIE 2729 Optical Velocimetry*, 1996, vol. 2729, pp. 139–145.
- [134] L. Hasselink, “Digital image processing in flow visualisation,” *Annu. Rev. Fluid Mech.*, vol. 20, pp. 421–485, 1988.
- [135] A. A. Adamczyk and L. Rimai, “2-Dimensional particle tracking velocimetry (PTV): Technique and image processing algorithms,” *Exp. Fluids*, vol. 6, pp. 373–380, 1988.
- [136] R. D. Keane and R. J. Adrian, “Optimization of particle image velocimeters. Part I: Double pulsed systems,” *Meas. Sci. Technol.*, vol. 1, pp. 1202–1215, 1990.
- [137] R. Hain, C. J. Kähler, and C. Tropea, “Comparison of CCD, CMOS and intensified cameras,” *Exp. Fluids*, vol. 42, no. 3, pp. 403–411, Jan. 2007.
- [138] A. Upatnieks, K. Laberteaux, and S. L. Ceccio, “A kilohertz frame rate

- cinemagraphic PIV system for laboratory-scale turbulent and unsteady flows,” *Exp. Fluids*, vol. 32, no. 1, pp. 87–98, 2002.
- [139] “LaVision - PIV cameras.” [Online]. Available: [http://www.lavision.de/en/products/cameras/piv\\_cameras.php](http://www.lavision.de/en/products/cameras/piv_cameras.php). [Accessed: 31-Aug-2015].
- [140] “TSI - high frame rate cameras for time resolved measurements.” [Online]. Available: [http://www.tsi.com/Products/\\_Product-Accessories/High-Frame-Rate-Cameras-for-Time-Resolved-Measurements.aspx](http://www.tsi.com/Products/_Product-Accessories/High-Frame-Rate-Cameras-for-Time-Resolved-Measurements.aspx). [Accessed: 31-Aug-2015].
- [141] “PCO - Highspeed Cameras.” [Online]. Available: <http://www.pco.de/highspeed-cameras/>. [Accessed: 31-Aug-2015].
- [142] M. Kobatake, T. Takaki, and I. Ishii, “A real-time micro-PIV system using frame-straddling high-speed vision,” in *Proceedings - IEEE International Conference on Robotics and Automation*, 2012, vol. 397, no. 1, pp. 397–402.
- [143] J. Westerweel, “Fundamentals of digital particle image velocimetry,” *Meas. Sci. Technol.*, vol. 8, no. 12, pp. 1379–1392, 1997.
- [144] K. D. Hinsch, “Particle image velocimetry,” in *Speckle Metrology*, R. S. Sirohi, Ed. New York: Marcel Dekker, Inc., 1993, pp. 235–323.
- [145] C. Willert, “The fully digital evaluation of photographic PIV recordings,” *Appl. Sci. Res.*, vol. 56, no. 2–3, pp. 79–102, 1996.
- [146] J. W. Goodman, *Introduction to Fourier Optics*, 2nd ed. New York: THE MCGRAW-HILL COMPANIES, INC., 1996.
- [147] C. E. Willert and M. Gharib, “Digital particle image velocimetry,” *Exp. Fluids*, vol. 10, pp. 181–193, 1991.
- [148] R. D. Keane and R. J. Adrian, “Theory of cross-correlation analysis of PIV images,” *Appl. Sci. Res.*, vol. 49, pp. 191–215, 1992.
- [149] S. P. McKenna and W. R. McGillis, “Performance of digital image velocimetry processing techniques,” *Exp. Fluids*, vol. 32, no. 1, pp. 106–115, 2002.
- [150] E. O. Brigham and R. E. Morrow, “The fast Fourier transform,” *Spectrum, IEEE*, vol. 4, no. 12, pp. 63–70, 1967.
- [151] W. H. Press, S. A. Teukolsky, W. T. Vetterling, and B. P. Flannery, *Numerical Recipes: The Art of Scientific Computing*, 2nd ed., vol. 29, no. 4. Cambridge: Cambridge University Press, 1992.
- [152] M. Frigo and S. G. Johnson, “FFTW: an adaptive software architecture for the FFT,” *Proc. 1998 IEEE Int. Conf. Acoust. Speech Signal Process. ICASSP '98 (Cat. No.98CH36181)*, vol. 3, pp. 1381–1384, 1998.

- [153] M. Frigo and S. G. Johnson, "The Design and Implementation of FFTW3," *Proc. IEEE*, vol. 93, no. 2, pp. 216–231, 2005.
- [154] J. Nogueira, A. Lecuona, and P. A. Rodríguez, "Data validation, false vectors correction and derived magnitudes calculation on PIV data," *Meas. Sci. Technol.*, vol. 8, pp. 1493–1501, 1997.
- [155] D. Garcia, "A fast all-in-one method for automated post-processing of PIV data," *Exp. Fluids*, vol. 50, no. 5, pp. 1247–1259, 2011.
- [156] J. M. Foucaut, J. Carlier, and M. Stanislas, "Post-processing of PIV records to allow derivative computation," in *Proc. 10th Int. Symp. Appl. Laser Tech. Fluid Mech.*, 2000, vol. 16, pp. 1–9.
- [157] M. R. Cholemani, "Modeling and correction of peak-locking in digital PIV," *Exp. Fluids*, vol. 42, no. 6, pp. 913–922, 2007.
- [158] J. D. Luff, T. Drouillard, A. M. Rompage, M. A. Linne, and J. R. Herzberg, "Experimental uncertainties associated with particle image velocimetry (PIV) based vorticity algorithms," *Exp. Fluids*, vol. 26, no. 1–2, pp. 36–54, 1999.
- [159] M. Musall, P. Oberle, R. C. Baeza, J. F. Fuentes-Perez, J. A. Tuhtan, and F. Nestmann, "Beitrag zu detaillierten Analysen der Hydraulik von Schlitzpässen," *WasserWirtschaft*, vol. 105, no. 7–8, pp. 67–72, 2015.
- [160] M. Miyashita, T. Nakayama, T. Takase, Y. Ohkura, Y. Yoshida, H. Nishiguchi, A. Shima, and T. Nishimura, "High-power red laser diode for recordable DVDs," in *SPIE 5365, Novel In-Plane Semiconductor Lasers III*, 2004, vol. 5365, pp. 148–154.
- [161] K. Shibata, Y. Yoshida, M. Sasaki, K. Ono, J. I. Horie, T. Yagi, and T. Nishimura, "High-power 660-nm laser diodes for recordable dual layer DVDs," *Ieee J. Sel. Top. Quantum Electron.*, vol. 11, no. 5, pp. 1193–1196, 2005.
- [162] J. K. Sveen, "MatPIV - the PIV toolbox for MATLAB," 2004. [Online]. Available: <http://folk.uio.no/jks/matpiv/index2.html>. [Accessed: 04-Nov-2015].
- [163] P. V. y Alvarado, "Design of biomimetic compliant devices for locomotion in liquid environments," Massachusetts Institute of Technology, 2007.
- [164] T. Salumäe, "Design of a Compliant Underwater Propulsion Mechanism by Investigating and Mimicing the Body of a Rainbow Trout (*Oncorhynchus mykiss*)," Tallinn University of Technology, 2010.
- [165] H. El Daou, T. Salumäe, L. D. Chambers, W. M. Megill, and M. Kruusmaa, "Modelling of a biologically inspired robotic fish driven by compliant parts.," *Bioinspir. Biomim.*, vol. 9, no. 1, 2014.

- [166] C. B. Braun and O. Sand, “Functional Overlap and Nonoverlap Between Lateral Line and Auditory Systems,” in *The Lateral Line System*, S. Coombs, H. Bleckmann, R. R. Fay, and A. N. Popper, Eds. New York: Springer New York, 2013, pp. 281–312.
- [167] G. Toming, T. Salumäe, A. Ristolainen, F. Visentin, O. Akanyeti, and M. Kruusmaa, “Fluid dynamics experiments with a passive robot in regular turbulence,” in *Robotics and Biomimetics (ROBIO)*, 2012, pp. 532–537.
- [168] F. Visentin, M. C. Fiazza, O. Akanyeti, R. Venturelli, and P. Fiorini, “Towards flow-sensing robots: Situated analysis for PIV flow imaging,” in *IEEE 15th International Conference on Advanced Robotics: New Boundaries for Robotics, ICAR 2011*, 2011, pp. 606–612.
- [169] T. Salumäe and M. Kruusmaa, “Flow-relative control of an underwater robot,” *Proc. R. Soc. A*, vol. 469, no. 20120671, pp. 1–19, 2013.
- [170] G. Toming, L. D. Chambers, and M. Kruusmaa, “Experimental study of hydrodynamic forces acting on artificial fish in a von Kármán vortex street,” *Underw. Technol.*, vol. 32, no. 2, pp. 81–91, 2014.
- [171] A. I. Lupandin, “Effect of Flow Turbulence on Swimming Speed of Fish,” *Biol. Bull.*, vol. 32, no. 5, pp. 558–565, 2005.
- [172] W. Hanke, C. Brücker, and H. Bleckmann, “The ageing of the low-frequency water disturbances caused by swimming goldfish and its possible relevance to prey detection.,” *J. Exp. Biol.*, vol. 203, no. Pt 7, pp. 1193–1200, Apr. 2000.
- [173] E. Drucker and G. Lauder, “Locomotor forces on a swimming fish: three-dimensional vortex wake dynamics quantified using digital particle image velocimetry.,” *J. Exp. Biol.*, vol. 202, no. Pt 18, pp. 2393–2412, Jan. 1999.
- [174] B. P. Epps, P. Valdivia Y Alvarado, K. Youcef-Toumi, and A. H. Techet, “Swimming performance of a biomimetic compliant fish-like robot,” *Exp. Fluids*, vol. 47, no. 6, pp. 927–939, Jun. 2009.
- [175] F. E. Fish, P. Legac, T. M. Williams, and T. Wei, “Measurement of hydrodynamic force generation by swimming dolphins using bubble DPIV,” *J. Exp. Biol.*, vol. 217, no. 2, pp. 252–260, 2014.
- [176] E. D. Tytell, “Kinematics and hydrodynamics of linear acceleration in eels, *Anguilla rostrata*,” *Proc. Biol. Sci.*, vol. 271, no. 1557, pp. 2535–2540, 2004.
- [177] M. C. Leftwich and A. J. Smits, “Thrust production by a mechanical swimming lamprey,” *Exp. Fluids*, vol. 50, no. 5, pp. 1349–1355, 2011.
- [178] J. A. Tuhtan, G. Toming, T. Ruuben, and M. Kruusmaa, “A method to improve instationary force error estimates for undulatory swimmers,” *Underw. Technol.*, vol. 33, no. 3, pp. 141–151, 2016.

- [179] M. C. Leftwich, E. D. Tytell, a. H. Cohen, and a. J. Smits, “Wake structures behind a swimming robotic lamprey with a passively flexible tail,” *J. Exp. Biol.*, vol. 215, no. 3, pp. 416–425, 2012.
- [180] T. T. Takahashi, “On the decomposition of drag components from wake flow measurements,” in *35th AIAA Aerospace Sciences Meeting & Exhibit*, 1997, no. January, pp. 1–10.
- [181] P. A. Davidson, *Turbulence: And Introduction for Scientist and Engineers*. Oxford: Oxford University Press, 2004.
- [182] W. Hanke and H. Bleckmann, “The hydrodynamic trails of *Lepomis gibbosus* (Centrarchidae), *Colomesus psittacus* (Tetraodontidae) and *Thysochromis ansorgii* (Cichlidae) investigated with scanning particle image velocimetry.,” *J. Exp. Biol.*, vol. 207, no. 1999, pp. 1585–1596, 2004.
- [183] J. A. Tuhtan, J. F. Fuentes-Pérez, N. Strokina, G. Toming, M. Musall, M. Noack, J. K. Kämäräinen, and M. Kruusmaa, “Design and application of a fish-shaped lateral line probe for flow measurement,” *Rev. Sci. Instrum.*, vol. 87, no. 4, 2016.
- [184] A. J. Cotel, P. W. Webb, and H. Tritico, “Do Brown Trout Choose Locations with Reduced Turbulence?,” *Trans. Am. Fish. Soc.*, vol. 135, no. April, pp. 610–619, 2006.
- [185] D. L. Smith, R. A. Goodwin, and J. M. Nestler, “Relating Turbulence and Fish Habitat: A New Approach for Management and Research,” *Rev. Fish. Sci. Aquac.*, vol. 22, no. 2, pp. 123–130, 2014.
- [186] J. F. Fuentes-Perez, J. A. Tuhtan, R. Carbonell-Baeza, M. Musall, G. Toming, N. Muhammad, and M. Kruusmaa, “Current velocity estimation using a lateral line probe,” *Ecol. Eng.*, vol. 85, pp. 296–300, 2015.
- [187] M. Schletterer, G. Senn, M. Menghin, M. Hubmann, R. Schwarzenberger, C. Haas, P. Thumser, and T. Asgeirsson, “Technisches Fischmonitoring: Installation des ersten RiverWatcher Fischzählers in Österreich.” [Online]. Available: <https://www.springerprofessional.de/technisches-fischmonitoring-installation-des-ersten-riverwatcher/6110038>. [Accessed: 17-Aug-2016].
- [188] A. Schletterer, R. Reindl, and S. Thonhauser, “Options for re-establishing river continuity, with an emphasis on the special solution ‘fish lift’: examples from Austria,” *Rev. Eletrônica Gestão e Tecnol. Ambient.*, vol. 4, pp. 109–128, 2016.
- [189] J. A. Tuhtan, M. Schneider, J. F. Fuentes-Pérez, and M. Schletterer, “Research project Robo Fish: Examination of flow signatures in Vertical Slot Fishways using artificial lateral line,” Innsbruck, 2016.
- [190] Á. Rodríguez, M. Bermúdez, J. R. Rabuñal, A. M. Asce, J. Puertas, J.

- Dorado, L. Pena, and L. Balairón, “Optical Fish Trajectory Measurement in Fishways through Computer Vision and Artificial Neural Networks,” *J. Comput. Civ. Eng.*, vol. 25, no. 4, pp. 291–301, 2011.
- [191] J. Tuhtan, M. Kruusmaa, M. Schneider, G. Toming, and I. Kopecki, “FishView: Developing a Hydrodynamic Imaging System Using a Robot Fish with an Artificial Lateral Line,” in *10th International Symposium on Ecohydraulics*, 2014, pp. 1–4.
- [192] J. A. Tuhtan, N. Strokina, G. Toming, N. Muhammad, M. Kruusmaa, and J.-K. Kämäräinen, “Hydrodynamic Classification of Natural Flows using an Artificial Lateral Line and Frequency Domain Features,” in *E-proceedings of the 36th IAHR World Congress: International Association of Hydraulic Research (IAHR) World Congress*, 2015, pp. 1–8.
- [193] J. F. Fuentes-Perez, J. A. Tuhtan, R. Carbonell-Baeza, M. Musall, G. Toming, N. Muhammad, and M. Kruusmaa, “Current velocity estimation using a lateral line probe,” *Ecol. Eng.*, vol. 85, pp. 296–300, 2015.
- [194] N. Strokina, J.-K. Kämäräinen, J. A. Tuhtan, J. F. Fuentes-Perez, and M. Kruusmaa, “Joint Estimation of Bulk Flow Velocity and Angle Using a Lateral Line Probe,” *IEEE Trans. Instrum. Meas.*, vol. 65, no. 3, pp. 601–613, 2016.
- [195] S. Fukuda, J. A. Tuhtan, J. F. Fuentes-Perez, M. Schletterer, and M. Kruusmaa, “Random Forests Hydrodynamic Flow Classification in a Vertical Slot Fishway Using a Bioinspired Artificial Lateral Line Probe,” in *Intelligent Robotics and Applications: 9th International Conference, ICIRA 2016, Tokyo, Japan, August 22-24, 2016, Proceedings, Part II*, N. Kubota, K. Kiguchi, H. Liu, and T. Obo, Eds. Cham: Springer International Publishing, 2016, pp. 297–307.
- [196] N. Muhammad, N. Strokina, G. Toming, and J. Tuhtan, “Flow feature extraction for underwater robot localization: preliminary results,” in *IEEE International Conference on Robotics and Automation (ICRA)*, 2015, pp. 1125–1130.
- [197] N. Muhammad, G. Toming, J. A. Tuhtan, M. Musall, and M. Kruusmaa, “Underwater map-based localization using flow features,” *Auton. Robots*, pp. 1–20, 2016.

## **Appendix A**

G. Toming, T. Salumae, A. Ristolainen, F. Visentin, O. Akanyeti, and M. Kruusmaa, “Fluid dynamics experiments with a passive robot in regular turbulence,” in Conference Proceedings – *Robotics and Biomimetics (ROBIO 2012)*, pp. 532–537, 2012.



# Fluid Dynamics Experiments with a Passive Robot in Regular Turbulence

Gert Toming<sup>1</sup>, Taavi Salumäe<sup>1</sup>, Asko Ristolainen<sup>1</sup>, Francesco Visentin<sup>2</sup>, Otar Akanyeti<sup>2</sup>, Maarja Kruusmaa<sup>1</sup>

**Abstract**—This paper presents force measurements of a passive fish robot in a regularly turbulent flow. We placed the robot into a controlled hydrodynamic environment, in running water behind a cylinder which created alternately shed vortices (von Kármán vortex street). We monitored the flow field using digital particle image velocimetry and recorded the force measurements using a force plate. The measurements taken at different locations in the turbulent flow show that the lateral force (perpendicular to the flow stream) experienced by the robot increased significantly in the turbulent flow. On the other hand the drag (force along the flow stream) was reduced up to 42% with respect to swimming in the uniform flow. The drag reduction was mainly due to the shadowing effect of the cylinder. However robots didn't gain any advantage through their passive interaction with the vortex street. The drag-position relationship had a single minimum along both longitudinal and lateral axis highlighting a favorable location for energy saving. We interpret the results as an evidence that the turbulent flows can provide rewarding opportunities to derive more energy efficient and stable behavioral strategies for underwater robots.

## I. INTRODUCTION

STATE-of-the-art underwater robots do not model or navigate with respect to the flow. Research robots in laboratory conditions are tested in still water. Field robots are exposed to the flow but they treat the current or turbulence as a drift or disturbance to be compensated for. There is no underwater robot that takes advantage of the flow for better localization and navigation.

While robot builders consider flow as an annoying disturbance to be compensated by control algorithms, the biological evidence suggests that aquatic animals know how to turn it into an advantage. For example it is suggested that salmonoids migrating upstream in turbulent rivers spend time behind an object to recover from fatigue [1]. The metabolic consumption of oxygen by the rainbow trout is lower while entraining in the vortex wake [2]. Furthermore it is shown in many occasions that fish can minimize their energy consumption by adjusting their locomotion patterns to the vortex patterns. The best known study is by Liao et al. demonstrating a dead fish floating upstream behind a vortex wake of a bluff object [3]. This study suggests that the vortices encountered by the fish can be beneficial to reduce,

neutralize or even overcome the drag experienced by the fish due to the flow. A similar experiment has been repeated with a high aspect-ratio passive hydrofoil [1].

Today it is not well defined under which circumstances such positive fluid-body interactions can take place. When size of the vortices are too big or too small with respect to the body size or if the body does not interact with the vortices in the "right way", it is expected that vortices can have negative impacts on the interaction such as increasing the drag on the body or obstructing its stability [4]. To gain insight into how to interact with the vortices many studies have investigated the phenomenon of Kármán gaiting, the tendency of fish to synchronize with the periodically shed vortices. Fish adjust their tail beat frequency with the vortex shedding frequency.

There is no conclusive evidence and established consensus about whether the flow-exploiting behaviors, such as entraining and Kármán gaiting are passive or active (whether fish activate their muscles or they are simply actuated by the external forces due to the flow.) Also it is not known if fish need flow sensing to have a control on these behaviors. Moreover it is not possible to directly measure the drag of a swimming fish and the indirect measurements are rather imprecise. It is therefore only possible to indirectly estimate the energy consumption of fish in different flow regimes [2].

In this paper we develop a case for the exploitation of the same energy saving phenomena by an underwater fish robot. In robot applications we see two ways of taking advantage of the flow: i) to seek a position in the flow at which the drag is lower, ii) to interact with the flow "properly" to capture the energy which is readily available in the flow.

We describe experiments with passive underwater fish robots attached to the force plate in a regular turbulence. We record the force measurements both in downstream and lateral directions and we visualize the flow using digital particle image velocimetry. We analyze the relationship between the drag (proportional to the energy consumption of the robot) and flow speed at different locations in the vortex wake. We demonstrate that by choosing a convenient position inside the vortex wake, the robot can decrease the perceived drag. We furthermore propose a method to evaluate if favorable drag conditions arise from choosing the right spots in the flow or additional energy harvesting as a result of passive flow-body interaction also takes place.

This work is supported by European Union 7<sup>th</sup> Framework program under FP7-ICT-2007-3 STREP project FILOSE (Robotic Fish LOcomotion and SEnsing), [www.filose.eu](http://www.filose.eu)

<sup>1</sup>Centre for Biorobotics, Tallinn University of Technology, Estonia

<sup>2</sup>Dept. of Computer Science, University of Verona, Italy

Overall, the “drag well” inside a regular turbulence has a well-defined shape with a single minimum. It makes possible to tracking this minimum using simple gradient decent and, at least theoretically, by using only the proprioceptive sensing.

The rest of the paper is organized as follows. Next we describe the regular turbulence and the method which enables us to evaluate if the passive robot-vortex interactions are advantageous or disadvantageous to reduce the perceived drag. After this we describe the experimental setup and the methods for analyzing the flow. We then present the experimental results of the force measurements. Finally we discuss the results and their possible interpretation from the point of view of underwater robot design and control.

## II. SCOPE OF THE PAPER

### A. Regular turbulence

For this investigation we focus on Kármán vortex streets. Kármán vortex street is a periodic turbulence pattern observed at moderate Reynolds numbers in a wake of bluff objects. It is characterized by the vortex shedding frequency. In nature, regular turbulence often occurs in rivers where steady flow is obstructed by obstacles (stones, pillars, etc.).

In fish locomotion studies, as well as in experimental fluid dynamics, Kármán vortex streets offer benchmark problems in fish behavioral studies, because they are life-like on the one hand, but stable, relatively easy to characterize and repeatable on the other hand.

In laboratory conditions, a Kármán vortex street is created by placing a cylinder or half-cylinder into steady flow. The frequency of vortices of the Kármán flow can then be adjusted by calculating  $f = SV/L$  where  $f$  is the frequency of the vortices,  $L$  is the characteristic length of a shedder bar (cylinder),  $V$  is the velocity of the laminar flow and  $S$  is the Strouhal number for the given shedder bar. The Reynolds number of the Kármán vortex street  $Re = VL/n$ , where  $n$  is the kinematic viscosity of the fluid.

### B. Drag-Flow Relationship in Kármán Vortex Streets

In a Kármán vortex street we consider two components that influence the total drag ( $F_D^{KVS}$ ) experienced by the object. I.) The shadowing effect of the cylinder: The flow speed behind the cylinder is reduced due to the cylinder's shielding effect. We determine the reduced flow drag ( $F_D^U$ ) using the drag-flow relationship employed in uniform flows when  $Re > 1000$ ,

$$F_D^U = \frac{1}{2} \rho C_D A V^2, \quad (1)$$

where  $V$  is the velocity of the object relative to the fluid (for a static object  $V$  is equal to the flow speed),  $\rho$  is the mass density of the fluid,  $A$  is the reference area and  $C_D$  is the drag coefficient [5]. We estimate  $F_D^U$  using the average flow speed obtained from flow visualization.

II.) The turbulence in the flow: The interaction between the body and the turbulence in the flow (mainly periodically shed vortices if it is a stable vortex street) is complex and till today not well understood. We will call this component  $F_D^T$  where  $T$  stands for turbulence. We estimate  $F_D^T$  using the relation,

$$F_D^T = F_D^{KVS} - F_D^U, \quad (2)$$

where we obtain  $F_D^{KVS}$  from the force measurements. In this work, our goal is not to derive a model for  $F_D^T$  but to evaluate if it has a positive or negative value for our passive robot. Having  $F_D^T < 0$  would suggest that the interaction between the robot and the vortices is beneficial as total drag is reduced. On the other hand  $F_D^T > 0$  means additional drag on the robot. The proposed formulation is also useful to analyze biological studies. For instance when dead fish holding station in the vortex street [3],  $F_D^{KVS} = 0$ , therefore  $F_D^U = -F_D^T$ .

## III. MATERIALS AND METHODS

### A. Robots

Used robots are a fish shaped biomimetic robots mimicking a rainbow trout. They consist of a rigid heads and a flexible tails allowing fluid-body interactions. The prototypes and the fabrication methods are described in detail in [6]. The anteroposterior length of the T-prototype is 0.43 m and of the X-prototype is 0.5 m. The maximum size of the T-prototype on the dorsoventral axis is 0.125 m, on the left-right axis 0.06 m and for the X-prototype 0.145 m and 0.084 m respectively.

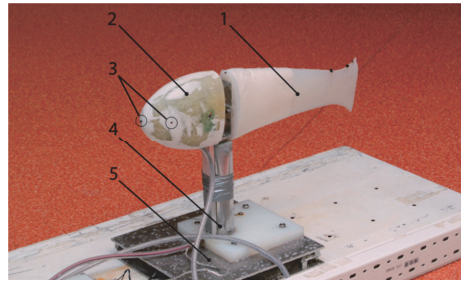


Fig. 1. Robotic fish T-prototype. 1 – Compliant tail; 2 – Head 3 – Pressure sensors mounted on the tip of the head and on the side of the head; 4 – Rotational actuation mechanism (not used in the passive tests); 5 – Force measurement plate with 4 load cells to measure longitudinal and lateral forces.

### B. The force plate

Prototypes were fixed on the force plate's midpoint with a rod (see Figure 1). The distance between the prototypes dorsoventral axis midpoint and force plate was 0.215 m. The force plate delivers the downstream ( $F_x$ ) and lateral force

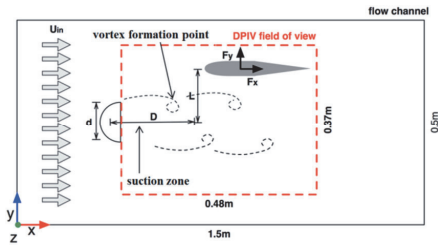


Fig. 2. Experimental setup. Robot fish placed into the flow behind the half-cylinder. Red dotted line shows the DPIV camera field of view.

( $F_y$ ) on the robot. We take  $F_x$  as a measure for the total drag felt by the robot.

( $F_x$ ,  $F_y$ ) were measured using 4 load cells (working range 10 kg). The load cells were assembled in the corner of the horizontal plate. The signals from the load cells were amplified (Texas Instruments Instrumentation Amplifier INA128UA, gain 500) and digitalized (Linear Technology A/D converter LTC 1867 B). Digitalized data from the load cells was transferred to the PC through RS-232 port (Atmel microcontroller ATmega 168).

### C. Flow experiments and measurements

The experiments are conducted in a flow pipe with a working section of 1.5 m x 0.5 m x 0.5 m. The pipe is embedded into a test tank. Uniform flow in the working section is created with the help of a U-shaped flow strengthener and two sequential laminators. An AC motor is used to create the circulation inside the flow tank and permits controlling the uniform flow speed with 0.04 m/s accuracy.

Force measurements were conducted both in uniform flows and in Kármán vortex street. Figure 2 illustrates the setup used in Kármán vortex street experiments. We mainly focused on two flow speeds 0.31 m/s and 0.48 m/s and the cylinder diameter 0.1 m. We placed the robot at different positions from the cylinder both in the downstream ( $D$ ) and lateral directions ( $L$ ).

We visualize the flow with digital particle image velocimetry (DPIV). DPIV provides multipoint velocity measurements within a planar slice of the flow by tracking the movement of particle images. A horizontal laser sheet was positioned at the flow tunnels mid-plane. The UI-5240HE-M camera from IDS Imaging Development Systems imaged from top at 50 frames per second. Image resolution was 1280 x 1024 pixels and the field of view was 48 cm x 38.4 cm giving the resolution of 26.7 pixels per cm. Images were then processed with MatPIV 1.6.1 toolbox in Matlab 7.10. Interrogation window size of 32 x 32 pixels with 50% overlapping was used. The output was a velocity field of 79 x 63 vectors, giving one vector after every 6 mm.

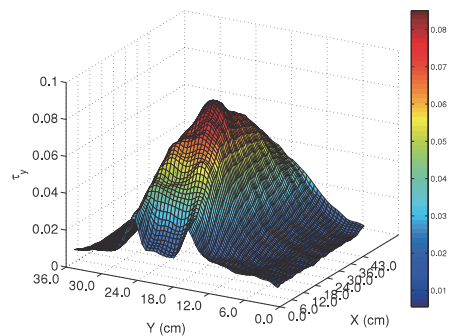
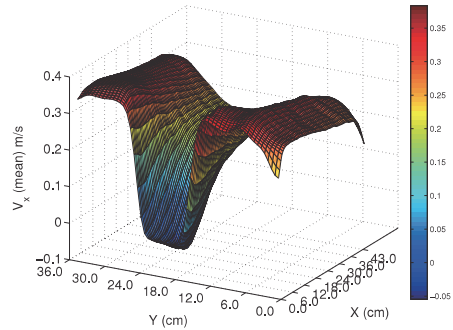


Fig. 3. Time averaged velocity  $V_x$  (above) and the turbulence intensity for the Kármán vortex street (below) generated with 31 cm/s flow speed.

## IV. DPIV FLOW IMAGING

DPIV flow analysis serve for three purposes: i) to validate the presence of a stable vortex street, ii) to evaluate how the flow speed varies with the robot's relative distance to the cylinder (we use these measures to estimate the reduced flow drag and also to correlate flow with the force measurements) and iii) to extract hydrodynamically significant features (such as vortex shedding frequency and vortex shedding point) which can help us to better interpret the force measurements.

Having a flow field  $V_x(x,y,t)$  and  $V_y(x,y,t)$  from DPIV measurements, Figure 3a and b illustrate, respectively, the time averaged  $V_x$  and the turbulence intensity for the vortex street generated with 31cm/s flow speed. The turbulence intensity is computed by  $V_y/\sigma(y)$ , where  $\sigma(y)$  is the standard deviation, and it indicates how steady the flow is [7]. The  $V_x$  in the middle is significantly lower than the two extremities. This is due to the shadowing effect of the cylinder. This middle region corresponds to the Kármán corridor where vortices are generated and shed. This agrees with high turbulence in the middle regions. Outside the Kármán corridor the flow is quasi-uniform therefore we see very low turbulence.

TABLE I  
THE CHARACTERISATION OF THE KÁRMÁN VORTEX STREET

	KVS <sub>1</sub>	KVS <sub>2</sub>
Cylinder diameter (m)	0.10	0.10
Flow speed (m/s)	0.31	0.48
Hydrodynamic features		
Base suction length (m)	0.11±0.01	0.11±0.01
Vortex formation length (m)	0.16±0.01	0.13±0.01
Vortex shedding point (m)	0.21±0.01	0.19±0.01
KS width (m)	0.23±0.02	0.24±0.02
Average flow speed (m/s)		
inside KS	0.18±0.01	0.18±0.01
outside KS	0.30±0.01	0.47±0.01
Average vortex speed ( $V_w$ )(m/s)	0.22±0.03	0.30±0.3
Min/Max mean vorticity	0.40±0.10	0.5±0.10
Vortex shedding frequency ( $f_w$ ) (Hz)	0.68±0.05	1.13±0.05
Wake wavelength ( $\lambda$ ) (m)	0.32±0.05	0.26±0.05
Spacing ratio	0.32±0.10	0.38±0.10
Strouhal number	0.32±0.20	0.44±0.20

We segment the Kármán corridor into regions in which the velocity conditions of the flow field is common. These regions are base suction region where flow recirculates towards the cylinder (negative  $V_x$ ), vortex formation zone where vortices are generated and the vortex street, the region in which vortices are detached from the core and travel with a steady speed. The vortex shedding point is the point that separates the vortex formation zone and the vortex street. For stability we track the shed vortices in time; vortex shedding frequency was around 0.7 Hz and 1.1 Hz, respectively, for flow speeds 0.31 m/s and 0.48 m/s. We analyze their spacing ratio between downstream and lateral directions. The spacing ratio with  $0.38±0.1$  was within the error margin of the theoretical value which is necessary for neutral stability. Table 1 summarizes the complete characterization of the Kármán vortex streets.

## V. FORCE EXPERIMENTS

### A. Uniform flows vs. Kármán vortex streets

We first compared force measurements with and without the cylinder at flow speeds 0.31 m/s and 0.48 m/s. The T-prototype was placed 0.23 cm behind the cylinder (after the vortex shedding point). The results (Figure 4) show that the longitudinal drag force  $F_x$  was lower in the vortex street. The drag reduction was 42% at 0.31 m/s and 38% at 0.48 m/s. Two differential factors were i) the reduced flow behind the cylinder and ii) the passive interaction between the vortices and the robot. In Section V-D we evaluate how each factor contributed the total drag.

On the other hand,  $F_y$  increased in the Kármán vortex street;  $F_y/F_x < 0.2$  (in uniform flows) and  $F_y/F_x > 2$  (in the Kármán street). The increase was related to the vortex effects on the robot and the relative difference between the average flow speed inside and outside of the vortex street. Having larger  $F_y$  provides insights to explain why lateral displacement of a rainbow trout is larger while Kármán gaiting than while steady swimming [3]. It also raises new questions on the control side; for instance how to utilize

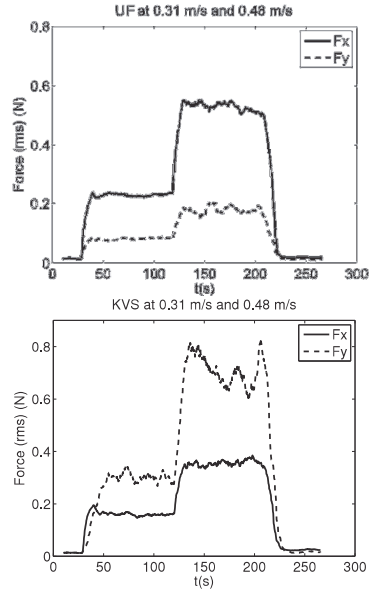


Fig. 4.  $F_x$  and  $F_y$  in uniform flows (above) and Kármán vortex streets (below) at flow speeds 0.31 m/s ( $30 < t < 120$  s) and 0.48 m/s ( $120 < t < 210$  s) for the T-prototype. The first 30 s and the last 60 s of the data set corresponds to still water readings.

these forces to increase the swimming efficiency and stability.

### B. Force-downstream position relations in Kármán streets

To study the force-position relation of the robot, we first placed the T-prototype along the Kármán vortex street centerline at different positions where  $D=[0.05, 0.35]$  m with a step of 0.03 m from the cylinder. At each position we recorded the force measurements for 90 s.

Figure 5a presents the  $F_x$  and the time averaged  $V_x$ ; note the high correlation between  $F_x$  and  $V_x$ . Up to the distance of 0.15 m,  $F_x$  was negative; flow was pushing the robot towards the cylinder.  $D=0.15$  m is relatively in a good agreement with the suction zone length of 0.11 m. The drag increases quickly in the vortex formation zone ( $0.11 \text{ m} < D < 0.19 \text{ m}$ ). After the vortex shedding point ( $D=0.19$  m) the rate of increase slowed down and it stopped at  $D=0.29$  m.

Figure 5b illustrates the  $F_y$  (rms) and  $V_y$  (rms) values. The evaluation has been done in the rms domain as the readings oscillated around zero due to alternately shed vortices. Note that  $F_y$  increased significantly (almost by two times) after the vortex shedding point ( $D=0.19$  m). Again we see high correlation between  $F_y$  and  $V_y$ .

### C. Force-lateral position relations in Kármán streets

Next we check how  $(F_x, F_y)$  varied as the robot moved away from the Kármán vortex street center axis ( $L=[-0.1, 0.1]$  m with a step of 0.025 m). The downstream distance of the robot from the cylinder was fixed at 0.2 m. Figure 6a shows

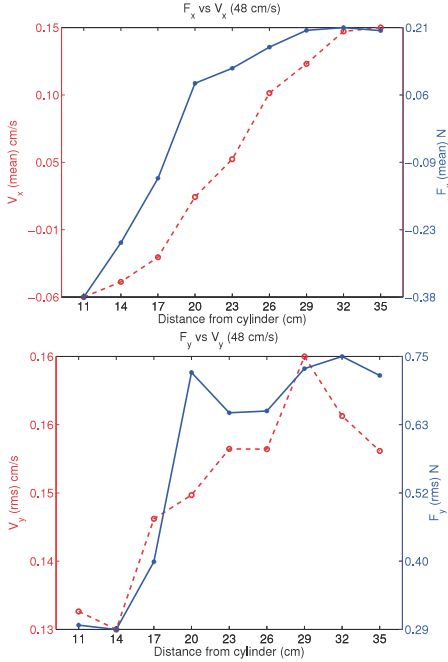


Fig. 5.  $F_x$  computed as an average versus downstream distance from the cylinder. The  $V_x$  measured by DPIV was also plotted (above).  $F_y$  computed as a root mean square versus downstream distance from the cylinder. The rms of  $V_y$  was also shown.

that the drag, together with the flow speed, increased proportionally with the magnitude of  $L$ . The robot was exposed to higher flows.

Both trends of  $(F_y, V_y)$  given in Figure 6b were rather M-shape where they increased towards the two vortex rows ( $L=-0.05$  m and  $L=0.05$  m). After the vortex rows they decreased rapidly. When  $L=-0.1$  m and  $L=0.1$  m the robot was mostly outside of the Kármán corridor which had 0.23 m width.

#### D. Robot fish size vs. cylinder size

To study the relation between the robot fish size and the size of the Kármán vortex street we made comparative experiments also with the X-prototype. Figure 7 shows that for both prototypes  $F_x$  and  $F_y$  followed the same trend, however and the drag felt by the X-prototype was about five times higher than for the T-prototype and lateral forces affecting the X-prototype were about two times higher than for T-prototype. This can be explained with the size of the X-prototype – the robot is more affected by the flow and due to its greater width it's interaction with vortices is stronger.

#### E. The turbulence increased the reduced flow drag

To evaluate the turbulence effect over the experienced drag, we use the relation in Equation 2. We obtain the total drag ( $F_D^{KVS}$ ) from  $F_x$  measurements. To estimate the

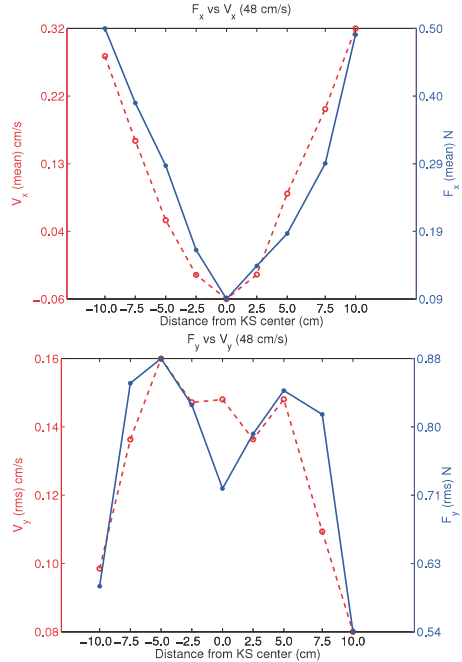


Fig. 6. Forces  $F_x$  (above) and  $F_y$  (below) depending on the lateral distance from the cylinder center axis. Flow velocity components  $V_x$  and  $V_y$  are also plotted respectively.

reduced flow drag ( $F_D^U$ ), we adapted Equation 1 to our setup. We measured  $F_x$  in uniform flows at flow speeds 0.1 m/s, 0.2 m/s, 0.3 m/s, 0.4 m/s and 0.48 m/s.

We identified their relationship,

$$F_D^U = 2.2766V^2 - 0.0093, \quad (3)$$

where the mean error of the model was less than 2%. To estimate  $F_D^U$  for each position of the robot in a Kármán vortex street we used the average flow speed measured by the DPIV at that location. We got the turbulence effect by subtracting the reduced flow drag from the total drag. Figure 8 illustrates  $F_D^T$  at different downstream positions ( $D$ ) in KVS at flow speeds 0.31 m/s and 0.48 m/s.

The results are consistently positive suggesting that the turbulence effect on the robot is negative; meaning vortex-robot interaction adds on the drag experienced by the robot. The higher the flow speed, the bigger the additional drag. This opposes to the previous studies reporting energy harvesting in a Kármán vortex street. During experiments we observed that the tail of the robot was moving passively with the vortex shedding frequency but the amplitude of the oscillation was very small. One possible explanation for the negative effect would be the ratio between the vortex rows spacing and the width of the robot ( $r$ ). When  $r < 0.1$ , such as this one, the major interaction between the robot and vortices

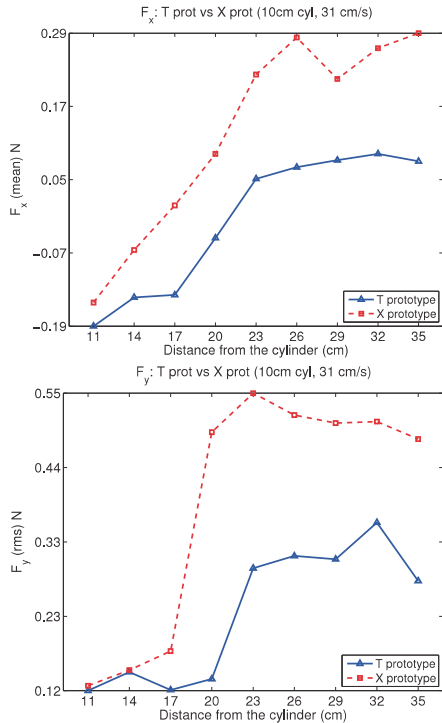


Fig. 7. Forces  $F_x$  (above) and  $F_y$  (below) versus downstream distance from the cylinder for T-prototype and X-prototype.

might take place at the head. In this case, the vortices can be compared to snow balls bombarding the robot and pushing it away from the cylinder. Probably the vortices were also

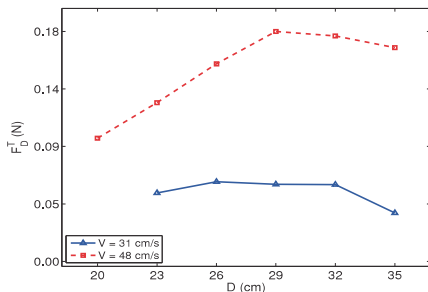


Fig. 8.  $F_D^T$  at different downstream positions ( $D$ ).

dissipated before they reached the anterior part of the robot (flexible tail). Therefore we observed small tail movements. That said, unnatural experimental conditions such as harnessing the robot with a rigid rod and not allowing the head to rotate should be taken into account while interpreting the results.

## VI. CONCLUSIONS

In this paper we conducted experiments with passive fish-shaped underwater robots in a uniform flow and regular

turbulence. We measured the force-position relationship in a Kármán vortex street and compared it with the force measurements in uniform flows. We furthermore present a method to analyze the effect of the turbulence by correlating flow measurements from DPIV with the force measurements.

The results show that both downstream and lateral forces to the robot are changing considerably depending on the position of the robot in the turbulence. In overall the drag is smaller where the reduction was up to 42% with respect to uniform flow conditions. Moreover, when the robot was placed in the suction zone behind the object, the flow pushed the robot towards the object. The lateral force in a Kármán vortex street, after vortex shedding point is considerably higher compared to lateral force in uniform flows.

From the experimental results we draw the following conclusions and guidelines for future work: The drag well in the regular turbulence along both longitudinal and lateral axis has a single local minimum. This point, theoretically, can be used as a control set point. For instance, the energy expenditure of the robot can be determined by monitoring the current consumption and a gradient decent algorithm can be implemented to trace a drag well. In real life situations, positioning in a region, where flow activity is low, is important as it permits hovering and surveillance without spending energy. Also robots on long missions may stay there to recharge the solar batteries and thus survive without human intervention.

There are two ways of turning flow into an advantage: i) to look for stable regions where forces on the robot are small and ii) to exploit vortices in the flow in order to capture the readily available energy. In this work we have demonstrated that the first way is achievable in a straightforward manner. The latter, on the other hand, presents significant challenges as the interplay between flexible bodies and vortices is not well understood. Even for passive interactions the resultant effects can have negative impact on the robot as seen in the presented experiments where the total drag perceived by the robot was bigger than what it should be in the reduced flows.

## REFERENCES

- [1] D. N. Beal, F. S. Hover, M. S. Triantafyllou, J. C. Liao, G. V. Lauder, "Passive propulsion in vortex wakes", *J. Fluid Mech.* (2006), vol. 549, pp. 385–402.
- [2] C. L. Cook and D. J. Coughlin, "Rainbow trout *Oncorhynchus mykiss* consume less energy when swimming near obstructions", *Journal of Fish Biology* (2010) 77, 1716–1723.
- [3] C. J. Liao, D. N. Beal, G. V. Laude, M. S. Triantafyllou, "The Kármán gait: novel body kinematics of rainbow trout swimming in a vortex street", *Journal of Experimental Biology*, vol. 206, 1059 - 1073, 2003.
- [4] P. W. Webb, "Entrainment by river chub *Nocomis micropogon* and smallmouth bass *Micropterus dolomieu* on cylinders", *J. Exp. Biol.*, vol. 201, 2403 – 2412, 1998.
- [5] G. K. Batchelor, "An Introduction to Fluid Dynamics", Cambridge University Press, ISBN 0521663962, 1967.
- [6] T. Salumäe, "Design of a compliant underwater propulsion mechanism by investigating and mimicking the body of a rainbow trout (*Oncorhynchus mykiss*)", MS Thesis, Tallinn University of Technology, 2010.
- [7] R. Michel, D. Arnal, "Laminar-turbulent transition", In IUTAM Symposium, Toulouse, France, 1989.

## **Appendix B**

G. Toming, L. D. Chambers, and M. Kruusmaa, “Experimental study of hydrodynamic forces acting on artificial fish in a von Kármán vortex street,” *Underw. Technol.*, vol. 32, no. 2, pp. 81–91, 2014.



# Experimental study of hydrodynamic forces acting on artificial fish in a von Kármán vortex street

Gert Toming\*<sup>1</sup>, Lily D Chambers<sup>2</sup> and Maarja Kruusmaa<sup>1</sup>

<sup>1</sup>Centre for Biorobotics, Tallinn University of Technology, 12618, Tallinn, Estonia

<sup>2</sup>Department of Mechanical Engineering, University of Bath, BA2 7AY, Bath, UK

Received 12 November 2013; Accepted 25 April 2014

## Abstract

The present paper describes the hydrodynamic forces acting on different sized fish-shaped objects in a von Kármán vortex street, where in a wake of an object a specific locomotion pattern, Kármán gaiting, is observed. The present paper investigates the hydrodynamic forces, both lateral force and torque on a passive fish-shaped body in those hydrodynamic conditions. By using a range of fish length to wake wavelengths, size matters were experimentally tested for balancing the forces on an artificial fish intercepting oncoming vortices, potentially to exploit the lateral and rotational elements in the flow that may facilitate Kármán gaiting in a biological fish. To do this, five artificial fish were manufactured to mimic a rainbow trout (*Oncorhynchus mykiss*), were inserted into the flow tunnel and recorded simultaneously the hydrodynamic forces and DPIV images. The experimental results found that the hydrodynamic forces supporting Kármán gaiting did not stop even if the body length of the fish-like object exceeded the wake wavelength. Overall, the obtained results help to understand fish and fluid interactions when swimming in the Kármán vortex street.

**Keywords:** artificial fish, underwater robotics, biorobotics, DPIV, underwater force measurements, Kármán vortex street, Kármán gaiting

## 1. Introduction

A von Kármán vortex street is a regular vorticity pattern that forms in the wake of bluff objects at moderate flow speeds (Zdravkovich, 1997). Several studies have investigated the interaction of a fish with vortices in periodic flows (Webb, 1998; Triantafyllou et al., 2000; Liao et al., 2003a; Liao et al., 2003b; Liao et al., 2004; Cook and Coughlin, 2010). It is observed that fish prefer such conditions and display a repertoire of distinct behaviours. In

von Kármán vortex street, a rainbow trout prefers to stay in one of the four zones near the object. These zones are the bow wake zone (upstream, in front of the object); the entraining zones (adjacent to the object, on the left and right side); and the Karman gaiting zone (along the midline, behind the object) – see Fig 1 (Przybilla et al., 2010).

Kármán gaiting is the term used to describe the scenario where fish swim in the Kármán vortex street along the midline of the wake with slaloming patterns around the incoming vortices. Studies of fish kinematics show that when Kármán gaiting, a fish synchronises its tail beat frequency to the vortex shedding frequency (Liao et al., 2003a). The body amplitude and curvature are larger than those of a fish swimming in a free stream at the same speed, while the head of the fish exhibits a distinct yaw motion (Liao et al., 2003a; Liao et al., 2003b; Przybilla et al., 2010).

It is also shown numerically that the vortex shedding frequency of artificial objects such as foils free to oscillate in the wake of a cylinder is synchronised with the vortex shedding frequency of the Kármán vortex street in which it is situated (Liao et al., 2004). Recently, fish have been video recorded Kármán gaiting in their natural environments (Liao, 2012).

Despite the larger body amplitude, larger curvature and lateral motion, it is experimentally shown by directly measuring the muscle activity (Liao et al., 2003b; Liao et al., 2004) and oxygen consumption (Cook and Coughlin, 2010) that fish use less energy when Kármán gaiting or entraining, compared to swimming at the same speed in a free stream flow. This suggests that the motion of the fish may be caused by external forces and can benefit from the environmental conditions to reduce energy consumption. In addition, it has been shown that dead fish as well as artificial devices such as high-aspect-ratio

\* Contact author. E-mail address: [gert.toming@ttu.ee](mailto:gert.toming@ttu.ee)

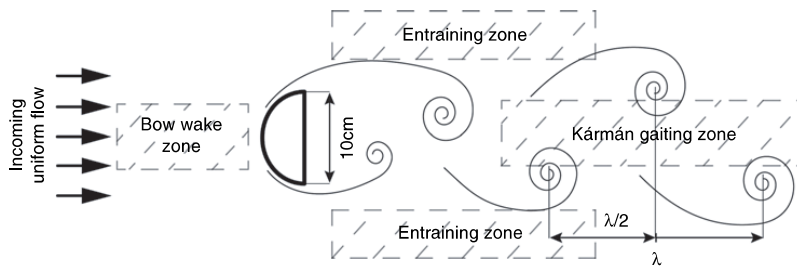


**Fig 1:** von Kármán vortex street. Four zones near the object where the rainbow trout prefers to stay (Przybilla et al., 2010; Liao, 2003a).  $\lambda$  is wake wavelength

hydrofoils, flexible filaments and cylinders are able to move passively upstream in a Kármán vortex street (Beal et al., 2006; Wang et al., 2009; Phillips et al., 2010).

Fish use muscles to stabilise and remain in the vortex street, with a measurable alteration to their free swimming gait, including increased body amplitude and head angle (Liao et al., 2003a; Liao et al., 2004). When a fish prefers the Kármán gaiting zone varies greatly; for example, while in the experiments conducted by Przybilla et al. (2010), trout were able to Kármán gait only 7.9% of the total time, whereas in the experiments conducted by Liao (2006) it was about 80%. The reason for this is still unknown, but it is proposed that it depends mostly on the cylinder diameter to fish length ratio (Liao et al., 2003a; Liao, 2006; Taguchi and Liao, 2011). When size of the vortices are too big (Lupandin, 2005) or too small with respect to the body size, or if the body does not constructively interact with the vortices, it is expected that vortices can have negative effects on the interaction, such as increasing the drag on the body or obstructing its stability (Webb, 1998).

Passive fish-shaped robots can gain advantages from the Kármán vortex street. The drag and lateral force affecting them depends on their positions in the vortex street and is related to the flow speed. By adjusting the position of the passive fish-shaped object in the turbulent flow, it is possible to reduce the drag up to 42% with respect to swimming in the uniform flow (Toming et al., 2012). An actively swimming fish robot is also shown to improve its swimming efficiency up to 23% by synchronising its tail beat with oncoming vortices with a particular phase lag (Ježov et al., 2012).

Despite passive motion not being a stable phenomenon (as objects moving upstream will eventually reach the suction zone behind the object and become destabilised), there are conditions in the flow for energy harvesting and energy reduction. Understanding those flow conditions and their interaction with a fish-like body further would help to explain to what extent fish behaviour could be

caused by its geometry, and what the scale of the environmental forces are. So far there is no study that experiments with different body to wavelength ratios of fish or hydrofoils to understand how general the Kármán gaiting phenomenon is.

The present study experimentally investigates the hydrodynamic forces in a von Kármán vortex street exerted on a range of fish-shaped body lengths. Forces acting on live swimming fish cannot be directly measured easily. Therefore, the present paper describes a series of experiments with different sized artificial fish made from silicone. These artificial fish were fixed to a force plate at their centre of mass and inserted into the flow channel. Forces and torques applied to the fish dummies were recorded simultaneously with digital particle image velocimetry (DPIV) images to correlate the force readings to hydrodynamic effects. By measuring the fluid forces at scales relevant to a swimming fish, with an object that embodies the natural fish geometry, the present paper investigates how a specific flow condition can be exploited by the fish or fish-like robots of different sizes.

The relative wake wavelength to artificial fish length ratio is expected to play a significant role in controlling the forces exerted on the form. Kármán gaiting described in its simplest form is a combination of the increased lateral sway, head angle and decreased tail beat frequency. The aim is to see if there is a specific range for the ratio of fish to cylinder size, where the two aspects of lateral sway and head angle will be maximised for a fixed object in the central Kármán vortex street. For this purpose, the hydrodynamic force measurements are correlated with the DPIV data to understand how the hydrodynamic forces from the surroundings create the lateral and rotational motion of the fish-shaped object.

## 2. Materials and methods

### 2.1. Artificial fish

In order to conduct force and torque measurements, five different sized fish dummies were built

**Table 1:** Dimensions of the fish dummies

Prototype number	Length (cm)	Normalised length	Height (cm)	Width (cm)	Transverse projected area (cm <sup>2</sup> )	Mass (kg)	Lzz* (kg × m <sup>2</sup> )
1	16.2	0.405	4.4	2.0	47.7	0.0591	$7.37 \times 10^{-5}$
2	20.5	0.513	5.2	2.3	67.4	0.992	$1.66 \times 10^{-4}$
3	29.2	0.730	6.7	3.4	151.2	0.336	$1.38 \times 10^{-3}$
4	31.4	0.785	7.0	3.8	166.1	0.454	$2.31 \times 10^{-3}$
5	46.7	1.168	13.5	6.9	422.2	1.72	$1.39 \times 10^{-2}$

\* Fish's moment of inertia with respect to the axis of the measured momentum

(Table 1). To mimic the body shape of a real rainbow trout (*Oncorhynchus mykiss*), five freshly dead trout were brought from a local fish breeder and used for making gypsum molds. Real fish morphological characteristics and geometry parameters can be seen in Lythgoe and Lythgoe (1991) and Nelson (1976).

Fish dummies (Fig 2a) were casted using a platinum cure silicon rubber Dragon Skin R10 with the Young's modulus of 181 kPa (Salumäe, 2010) from SMOOTH-ON Inc (Easton, Pennsylvania, USA). The width and height of fish dummies were measured with the step of 1cm, and bending stiffness was calculated by approximating cross-sections to ellipses. Bending stiffness profiles of rubber fish can be seen in Fig 2b. Despite the flexible material used, the hydrodynamic forces in the test environment were too small to bend fish bodies, and during force measurement they acted as rigid bodies. To obtain the moment of inertia, DAVID-Laserscanner Software (DAVID Vision Systems GmbH) was used to 3D scan the fish dummies and SolidWorks 2013 (Dassault Systèmes SolidWorks Corporation) was used for calculations.

## 2.2. Flow tunnel

The experiments were conducted in a flow pipe with a working section of 0.5m × 0.5m × 1.5m

embedded into a test tank (Fig 3). Uniform flow in the working section was created with the help of a U-shaped flow straightener and two sequential collimators. An AC motor was used to create the circulation inside the flow pipe, and the flow speed was calibrated using a digital particle image velocimetry (DPIV) system.

## 2.3. Custom-made force plate

A custom-made force plate was used to measure the hydrodynamic forces acting on the body. The prototypes were fixed to the force plate's midpoint with a rod (Fig 4), which was shielded from the flow by covering it with a sheath pipe. The force plate delivered the downstream force ( $F_x$ ), lateral force ( $F_y$ ) and rotational torque ( $\tau$ ) acting on the fish dummies. Eight load cells were placed at the corners of a horizontal plate, and their readings were combined to express  $F_x$ ,  $F_y$  and  $\tau$ . All signals were amplified with instrumentation amplifier (Texas Instruments INA128), digitalised with a 16-bit analogue to digital converter (Linear Technology LTC1867) and sent to a PC via RS-232, using an Atmel ATmega328 microcontroller.

## 2.4. Digital particle image velocimetry system

The custom-made DPIV system was used for flow visualisation and quantitative measurements. The

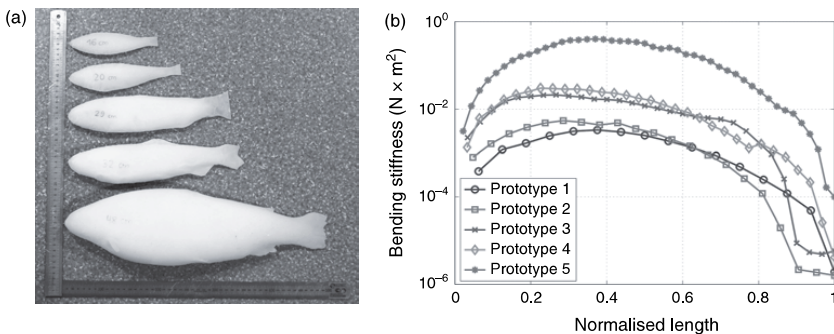


**Fig 2:** (a) Silicone-made fish dummies mimicking rainbow trout with the body lengths from 16.2–46.7cm; and (b) stiffness profile of the fish dummies (body lengths have been normalised)

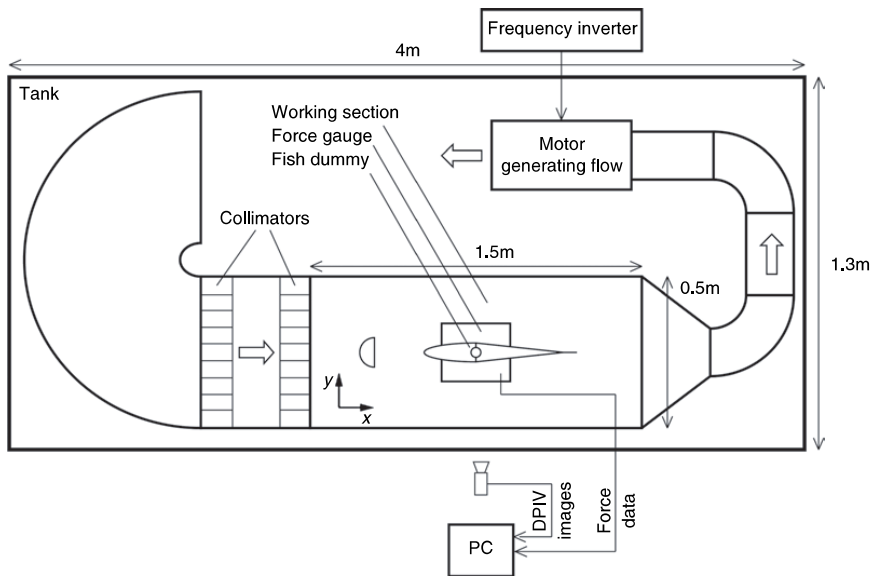


**Fig 3:** Schematic of the test tank, illustrating the experimental setup – position of cylinder and fish dummies in the working section

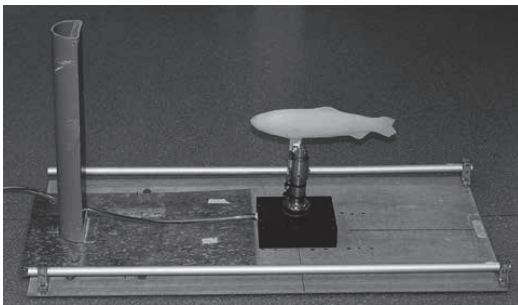


**Fig 4:** A photo of experimental setup. Rubber fish is fixed with a rigid rod to the force plate, at a distance of three diameters downstream from the D-shaped cylinder

flow was seeded with EPS-5 raw material granules (purchased from Polyston LLC), and the light sheet was created using a laser diode from the 22x DVD-writer (LG Corporation) with the help of a cylindrical lens. The particle motion was recorded with the resolution of  $1,280 \times 1,024$  pixels at 50 FPS using the UI-5240HE-M camera from IDS Imaging Development Systems.

To control the camera and record images, National Instruments LabVIEW 10.0.1 (National Instruments Corporation) was used. Recorded images were processed offline using MatPIV 1.6.1 (Sveen, 2004) toolbox in MATLAB 7.10 (the MathWorks, Inc.) with an interrogation window size of  $32 \times 32$  pixels with 50% overlapping, giving a velocity vector field with the maximum dimensions of  $79 \times 63$  vectors.

### 2.5. Experimental setup

To generate the Kármán vortex street, a D-shaped cylinder with a diameter of 10cm and the flow speed of 30cm/s was used, giving a Reynolds number of 30,000. A rigid rod was used to fix each fish model to the force plate. The rod was attached to the body at the centre of mass. The whole setup was then inserted into the flow tunnel. The rubber fish nose was always kept 35cm away from the semi cylinder's edge.

For each experiment, a rest period of 60s was given after switching on the flow to allow the Kármán vortex street to fully develop. Then force signals (at 100Hz) and DPIV images (at 50Hz) were simultaneously recorded for 60s using custom-made LabVIEW Vis running in parallel. Force data was saved into LabVIEW measurement files (\*.lvm). Data and video files were later processed offline in MATLAB. For clearer signal representation, all acquired signals were filtered using the 10<sup>th</sup> order Butterworth low pass filter with the cut-off frequency of 1Hz.

## 3. Results

### 3.1. Flow analysis

The Kármán vortex street generated in the flow tank was analysed with DPIV in two steps. First, the area directly downstream from the cylinder was measured to determine the vortex shedding point and the vortex shedding frequency. The experimental window was  $45 \times 42$ cm, with the left edge aligned with the downstream edge of the cylinder.

**Table 2:** Parameters of hydrodynamic test environment of a 10cm D-shaped cylinder in 30cm/s flow

	0–42cm from the cylinder	35–77cm from the cylinder
Vortex street bounds	Width: 13,8cm (±1,45) Expansion rate: 0,14	Width: 22,6cm (±1,29) Expansion rate: 0,10
Suction point	8,0cm (±0,73)	–
Vortex formation length	15,2cm (±0,73)	–
Vortex shedding point	14,52cm (±0,73)	–
Mean velocity (downstream)	Inside vortex street: 18,9cm/s Outside vortex street: 33,5cm/s	Inside vortex street: 24,5cm/s Outside vortex street: 30,1cm/s
Vortex shedding frequency	0,7Hz (±0,098)	0,7Hz (±0,098)
Wake wavelength	40cm	40cm
Strouhal number	0,2	0,23

In the second step, the vortex street was measured, starting from the position where the fish dummies were later inserted. In this case, the experimental window was 40 × 42cm, and covered the distance from 35cm to 77cm downstream from the cylinder. Recorded DPIV images were studied using a post-DPIV analysis toolbox (Visentin et al., 2011) developed for MATLAB. The same toolbox was used to calculate the expected vortex street parameters prior to experiments. Using a 10cm cylinder at the flow speed of 30cm/s, the theoretical vortex shedding frequency was 0.74Hz and Strouhal number was 0.2.

Five-hundred frames of data that correspond to 10s were analysed, and the results are presented in Table 2. Within the vortex street, the expansion rate expresses the rate of change of width of the street with downstream distance. The suction point, vortex formation length and vortex shedding point were measured downstream from the cylinder’s edge.

From Table 2, it can be seen that the measured vortex shedding frequency and Strouhal number match well with the theoretically calculated ones. The experimentally generated vortex street directly downstream from the cylinder edge is shown in Figs 5 and 6. In Fig 5 there is a raw, low frame rate

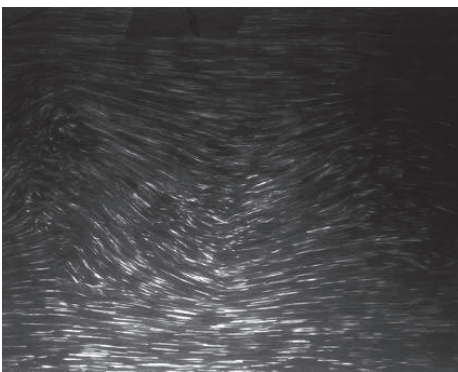


**Fig 5:** Flow visualisation using low frame rate (10Hz) and the shutter speed of about 99ms

DPIV image, and the velocity vectors after processing with MatPIV toolbox are shown in Fig 6.

### 3.2. Force measurements

First, the force plate was used to measure the  $F_y$  for the unit area (1cm<sup>2</sup>) in the vortex street at the flow speed of 30cm/s. This experiment was done separately, having only the force plate and 4cm<sup>2</sup> metal plate attached to it in the flow tunnel. The data were used to generate idealised force signal in MATLAB with the same amplitude and wavelength. Then the surface area of fish dummies was measured by dividing the area into 1cm-wide sectors perpendicular to the backbone (see Table 1), and a model was generated to understand the fluid-body interactions. To simplify the model, the fish-like body is assumed to be stiff in order to measure the external forces, body length is rounded to nearest integer, body is considered to be flat and the drag force generated by the incoming flow is ignored. Equation 1 describes the torque that is affecting the fish:

$$\tau = \sum_{i=1}^n F_{y_i} * A_i * (l_i - l_{com}) \tag{1}$$

where  $\tau$  is the torque;  $F_y$  is the lateral force applied on the unit area;  $A$  is the surface area of the fish body at given position;  $l$  is the calculation point’s distance from fish nose;  $l_{com}$  is the centre of mass (distance from the nose);  $i$  is the current position on the fish body; and  $n$  is the number of subdivisions (length of each subdivision is 1cm, so  $n$  = fish body length).

Using the surface area and idealised force signal as inputs to Equation 1, the torque was calculated at the centre of mass – the distance from the nose where the same sized real prototype’s centre of mass was located.

Secondly, the lateral force and torque signals were directly measured for all artificial fish in the Kármán vortex street and in the uniform flow to verify if they would generate any self-oscillations. Results are plotted in Fig 8, which shows that torque

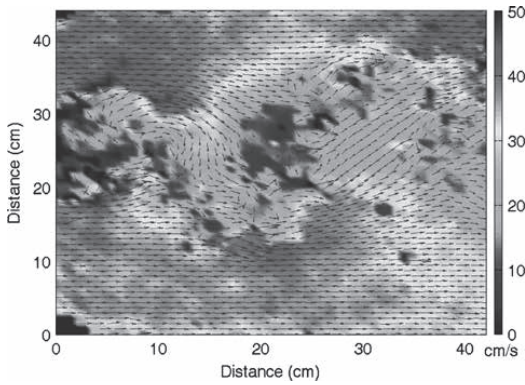


**Fig 6:** Velocity field of the experimentally generated Kármán vortex street behind the cylinder. Shades of grey indicate the velocity magnitude; the darkest grey represents maximum

fluctuations in uniform flow are not periodic. These fluctuations were caused by the irregularities in the hydrodynamic test environment and by the small asymmetries of casted fish bodies.

The results of calculations and measurements are shown in Figs 7 and 8. Fig 7 shows that the root-mean-square (RMS) values of torque and lateral force are increasing as the fish size increases, however, for the fourth prototype, there is a drop in the  $F_y$  strength. Increase of  $\tau$  and  $F_y$  can be explained with the larger surface area of the larger fish. The larger the surface is the more it is exposed to hydrodynamic forces. However, because of the increasing body mass and moment of inertia, the resultant yaw and sway motions are decreasing.

From Fig 8 it can be seen that the torque signal is minimal (both the calculated and measured one) for the two smallest fish-like dummies. It shows that the rotational motion is created with two vortices on the opposite sides, which suggests there is a minimal body length (equal to half of the

wavelength of the wake) that permits the fish to exploit those forces.

The first body is smaller than half of the wake wavelength of the vortex street. The second body has exactly the length of half of the wake wavelength. In this case, some energy from the vortices is still lost because the last vortex affects only the tip of the fish tail. The small difference in the torque signal amplitude values can be caused by the fact that fish bodies are not flat as the model assumed but are three dimensional. In the case of the hydrodynamic measurements, the amplitude and phase of the vortices are also not constant as in simulations. This could be the result of some irregularities in the hydrodynamic test environment.

From Figs 7 and 8, it can be seen that the RMS value of torque for all measured fish bodies increases as the body length increases, although the third vortex, near the tail of the fish, is counterbalancing the torque of the first two vortices and therefore the resultant torque, causing the rotational motion of the fish head in Kármán gaiting, should be minimal. However, Fig 9 shows that for the fifth prototype, the phase shift between  $F_y$  and  $\tau$  is almost  $180^\circ$  ( $168.8^\circ$ ). Therefore, after every half period, the  $\tau$  and  $F_y$  were simultaneously reaching the zero point (see also Fig 10b). For the smaller fish dummies, the phase shift was considerably lower – in these cases there is always lateral force or torque present (see also Fig 11b).

Forces and torques were measured with instrumentation uncertainties of  $u(F_y) = F_y \times 8.27 \times 10^{-5}$  and  $u(\tau) = \tau \times 4.83 \times 10^{-4}$  at 95% confidence level. These are negligible compared to the effects of the measurement noises, whose maximum standard deviations in forces and torque were identified experimentally as  $\sigma_{F_y} = 0.0377\text{N}$  and  $\sigma_\tau = 0.0025\text{Nm}$ . The measured amplitudes of the forces were clearly larger than the (zero-mean) noise's standard deviation.

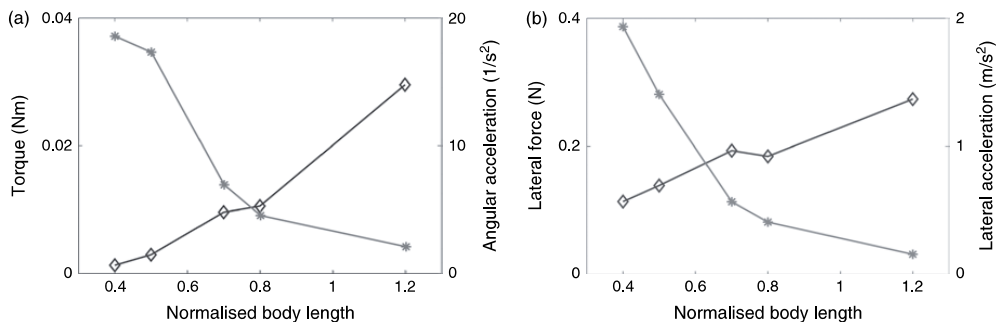


**Fig 7:** (a) Torque (RMS) and angular acceleration dependent on the body length to wake wavelength ratio that would act on a free swimming fish; and (b) lateral force (RMS) and lateral acceleration dependent on the body length to wake wavelength ratio that would act on a free swimming fish

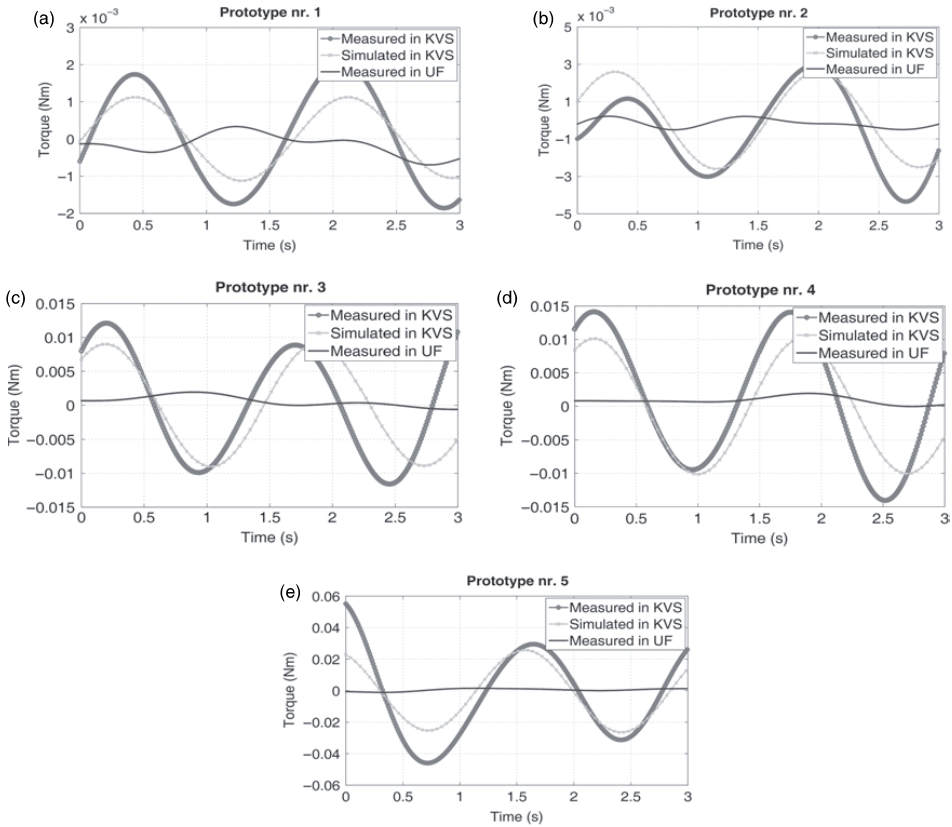


**Fig 8:** Measured and simulated torque signals. KVS is Kármán vortex street and UF is uniform flow

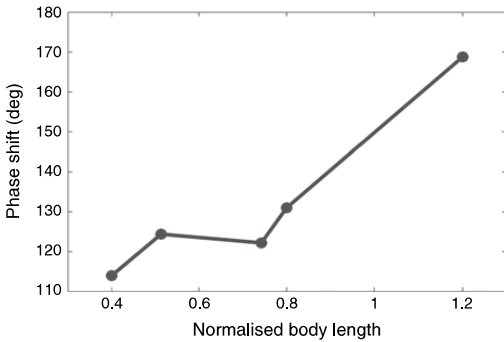


**Fig 9:** Phase shift between torque and lateral force depending on the body length to wake wavelength ratio. The maximum  $F_y$  signal was taken as the starting point, and the delay to the torque signal maximum was calculated for all prototypes

**3.3. Force signal and digital particle image velocimetry correlation**

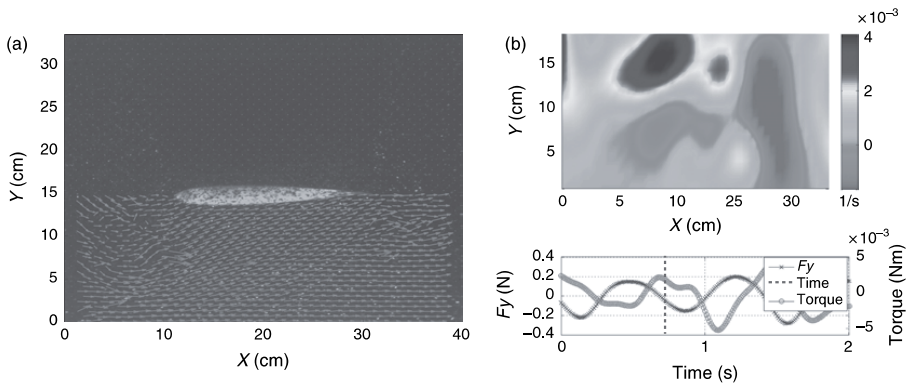
DPIV images were recorded simultaneously with  $F_y$  and torque measurements. The post-processing toolbox was used to plot torque and  $F_y$  signals and the corresponding vorticity images.

Fig 10 shows the second prototype in the Kármán vortex street. It is clearly seen that when the first vortex hits the fish head, the maximum torque is generated. Fig 11 shows the fifth body between the vortices; here, the fish body is affected by two same signed counter clockwise (CCW) vortices at the same side (while one opposite signed vortex is on the other side of the fish dummy). In this case, the torque was minimal but the fish body still experienced some lateral force.

Although the vortices get distorted and dissipated when travelling along the body because of the surface friction and viscous forces, they can still significantly influence a fish body, as seen from force measurements. At the moment where two same signed vortices are on the same side of the body, the torque and the lateral force were minimal and the fish-shaped object experienced loss of performance and instability.

**4. Discussion**

The present paper studied the hydrodynamic forces acting on an artificial fish rigidly held in a



**Fig 10:** (a) DPIV image of a 20.5cm-long fish body in the vortex street, with velocity vectors marking the experimental window used for post processing; and (b) vorticity calculated from Fig 10a, the darkest grey indicates CCW vorticity. Simultaneously recorded torque and  $F_y$  are shown on the lower graph. The dotted marker indicates the time step when DPIV image was taken

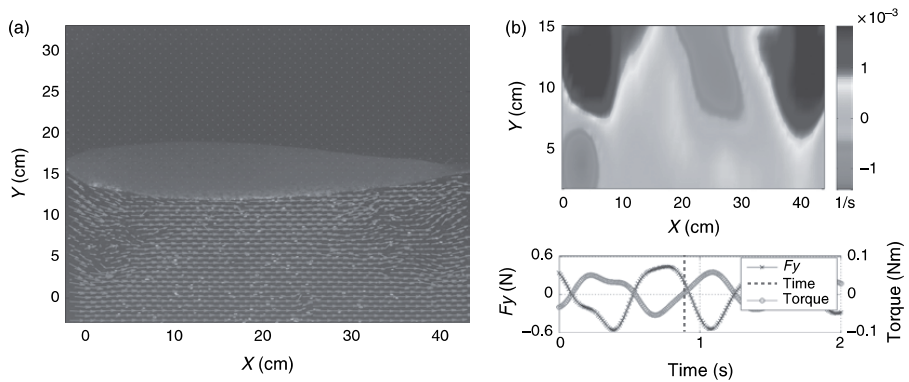


**Fig 11:** (a) DPIV image of a 46.7cm-long body in the vortex street. Velocity vectors mark the experimental window used for post-processing; and (b) vorticity calculated from Fig 11a; the darkest grey indicates CCW vorticity. Simultaneously recorded torque and  $F_y$  are shown on the lower graph; the dotted marker indicates the time step when DPIV image was taken

von Kármán vortex street. The fluid oscillations from the shed paired vortices were analysed along the artificial fish lengths, and different cylinder to body length ratios were tested, using five different sized artificial fish with the shape of a rainbow trout.

Furthermore, a model was used to calculate the idealised theoretical torque that could affect the shapes, and the hydrodynamic forces exerted on the artificial fish between the vortices were directly measured. Finally, these measurements were correlated with the DPIV readings. The present paper showed experimentally how the vortices are travelling along the fish body and how they would generate rotational (yaw) and lateral (sway) motions. From this, a better understanding was gained of the fluid forces affecting a fish when swimming in von Kármán vortex street.

The present work has certain limitations. First, the artificial fish used are stiff compared to real fish. Second, they are not allowed to swim freely and adopt the motion of Kármán gaiting, but instead were rigidly fixed to the force plate and therefore subject to any additional hydrodynamics generated by the rig. This, however, allowed for direct measurement of hydrodynamic forces applying to fish-shaped objects in the Kármán vortex street.

Kármán gaiting fish have a characteristic motion which can be described as slaloming between eddies. Liao (2003) measured the mechanism of Kármán gaiting in a video clip combining fish motion with the DPIV measurements of the surrounding fluid.

One possible mechanism for the interaction of vortices and varying size of artificial fish, in terms of

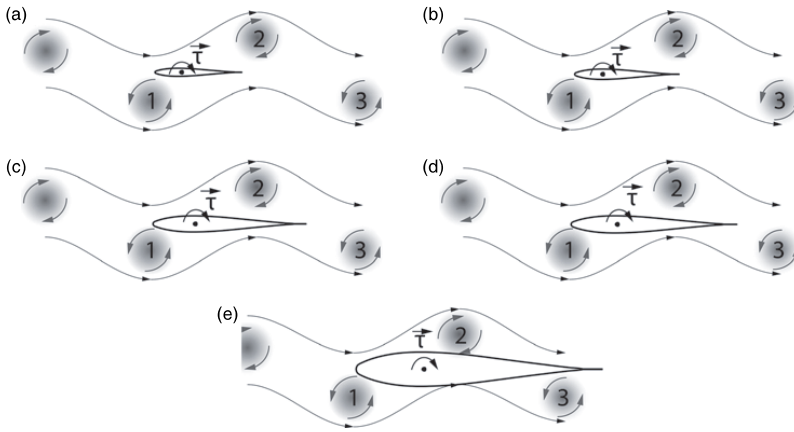


**Fig 12:** Scaled representations of fish bodies with respect to the vortex street for all tested cases (adapted from Liao, 2003): (a) fish body length is smaller than half of the wake wavelength and fish is affected by only one vortex; (b) normalised body length is 0.5, and vortices 1 and 2 are affecting the fish from the opposite sides, resulting in the maximum rotational torque  $\tau$  and minimal lateral force; (c)–(d) normalised body length is from 0.5 to 0.8 and bodies are affected simultaneously by two vortices; and (e) normalised body length is 1.2, two opposite signed vortices (1 and 2) are generating the torque  $\tau$ , while the third vortex is counterbalancing this effect

the torque, is depicted in Fig 12 using simple schematics. A vortex, intercepting the side of a fish, exerts a hydrodynamic force on the fish body that could result in a lateral and rotational motion. If the fish itself is passive, these forces could be responsible for the characteristic lateral motion, as well as rotation of the fish head while Kármán gaiting.

When two or more vortices are acting on the body at the same time, the resultant force may depend on their combined strength and location. Fig 12b shows the ventral outline of a model fish, centrally located in a Kármán vortex street, with a total body length that is half of the wake wavelength, like fish body 2. In this case two opposite signed vortices (1 and 2) are affecting the fish at its head and tail.

In this case, the moment arm of the lateral forces is at a maximum and the fish with a stiff body should experience the highest torque. At the same time, a fish form, with a body length less than half a wake wavelength (Fig 12a) would have only one vortex exerting force on it, and therefore the fish should experience lateral motion but less torque. It has been previously shown that when the vortex size exceeds two-thirds of the fish body length, the vortex can unbalance the fish and the swimming performance will decrease (Lupandin, 2005). Therefore it seems reasonable to assume that there is a minimal fish size to wavelength ratio where the fish is long enough to take advantage of the environment for Kármán gaiting. This is also supported

by the experimental data shown in Fig 8. It can be seen that for the fish bodies with the body length of more than half of the wake wavelength, the torque increases 10 times more in comparison with the shorter dummies.

In Fig 12e, there is a fish with a body length of approximately the wake wavelength, like fish body 5. In this situation, the torque should be minimal. Although the first and second vortices that are opposite signed are trying to rotate the fish, the third vortex (same signed as the first vortex) is cancelling out this effect by inducing the torque in the opposite direction. It is suggested that this balancing of fluid forces would limit the lateral forces of the oscillating fluid, thereby reducing the ability to slalom. Therefore, it seems reasonable to assume that there is also a maximum fish size to wavelength ratio at which this periodic flow characteristic can be used beneficially.

The aim of the present paper is to study whether there is a specific range of fish sizes when the forces available to use Kármán gaiting is most effective and whether this effect disappears once the fish body length exceeds the wake wavelength of the travelling vortices. In previous experimental studies, the body length of artificial devices such as hydrofoil (Beal et al., 2006) and flexible cylinders (Phillips et al., 2010) was less than half of the wake wavelength. However, in the experiments presented in the present paper, the body length of fish-shaped objects exceeded the wake wavelength of travelling

vortices, giving a situation when the object was simultaneously affected by three vortices.

Experimental results showed that the lateral and rotational forces did not stop when the fish body length reached or exceeded the wake wavelength as expected. These forces instead shifted too close to antiphase. However, lateral and angular accelerations caused by these forces were decreasing when the body mass was increasing, thus suggesting that larger fish would need larger and stronger vortex street.

It has been previously shown that the maximum energy is harvested when the phase shift is  $90^\circ$  (Beal et al., 2006). The present paper shows that when the fish length increases compared to the wake wavelength, the phase shift between lateral force and torque also increases. Active control of body length or body stiffness may help control the phase angle of the hydrodynamic forces affecting the robot fish in reference to centre of mass and thus use the energy of the vortex street.

Kármán gaiting is thought to be, to a great extent, a passive behaviour (Beal et al., 2006; Wang et al., 2009; Phillips et al., 2010). The present paper supports this view by showing that there are significant hydrodynamic forces in the flow affecting fish-shaped objects to sway and yaw.

The environmental effects studied here can also have an implication on the design of underwater vehicles. Several soft-bodied underwater vehicles (similar to the material properties of living fish) have previously been demonstrated in laboratory conditions (Epps et al., 2009; EL Daou et al., 2011). In Ježov et al. (2012), interaction with flow is shown to decrease the robot's energy expenditure in von Kármán vortex street, and it suggests that soft-bodied robots and fin propulsors may potentially be used for energy harvesting. Previous studies on energy harvesting have only experimented with hydrofoils shorter than the wavelength.

The present study also shows the effect of the environment when the fish (or a flexible hull vehicle) is longer. The third vortex near the end of the tail seems to have enough strength to create local counterbalancing force. Therefore, exploiting flexible rudders, whose bending radius is adjustable to the wavelength, might allow the fish-shaped object to take advantage of the energy in the flow.

## Acknowledgements

The authors are grateful to Otar Akanyeti and William Megill for their support. The present work is carried out under the FILOSE project, supported by the European Union, seventh framework programme (FP7-ICT-2007-3).

## References

- Beal DN, Hover FS, Triantafyllou MS, Liao JC and Lauder GV. (2006). Passive propulsion in vortex wakes. *Journal of Fluid Mechanics* **549**: 385–402.
- Cook CL and Coughlin DJ. (2010). Rainbow trout *Oncorhynchus mykiss* consume less energy when swimming near obstructions. *Journal of Fish Biology* **77**: 1716–1723.
- EL Daou H, Salumäe T, Ristolainen A, Toming G, Listak M and Kruusmaa M. (2011). A bio-mimetic design and control of a fish-like robot using compliant structures. In: Proceedings of IEEE 15th International Conference on Advanced Robotics (ICAR), 563–568.
- Epps BP, Alvarado PV, Tounsi KY and Techet AH. (2009). Swimming performance of a biomimetic compliant fish-like robot. *Journal of Experiments in Fluids* **47**: 927–939.
- Ježov J, Akanyeti O, Chambers LD and Kruusmaa M. (2012). Sensing oscillations in unsteady flow for better robotic swimming efficiency. In: Proceedings of IEEE International Conference on Systems, Man, and Cybernetics (SMC), 91–96.
- Liao JC. (2003). Trout Karman Gait PIV Movie. Available at [www.people.fas.harvard.edu/~glauder/Videos\\_Trout\\_Swimming.html](http://www.people.fas.harvard.edu/~glauder/Videos_Trout_Swimming.html), last accessed <28 April 2014>.
- Liao JC. (2006). The role of the lateral line and vision on body kinematics and hydrodynamic preference of rainbow trout in turbulent flow. *Journal of Experimental Biology* **209**: 4077–4090.
- Liao JC. (2012). Wild brown trout holding station behind a rock. Available at <http://liaolab.com/field/>, last accessed <28 April 2014>.
- Liao JC, Beal DN, Lauder GV and Triantafyllou MS. (2003a). The Karman gait: novel body kinematics of rainbow trout swimming in a vortex street. *Journal of Experimental Biology* **206**: 1059–1073.
- Liao JC, Beal DN, Lauder GV and Triantafyllou MS. (2003b). Fish exploiting vortices decrease muscle activity. *Science* **302**: 1566–1569.
- Liao JC, Beal DN, Lauder GV and Triantafyllou MS. (2004). Neuromuscular control of trout swimming in a vortex street: implications for energy economy during the Karman gait. *Journal of Experimental Biology* **207**: 3495–3506.
- Liao Q, Dong G-J and Lu X-Y. (2004). Vortex formation and force characteristics of a foil in the wake of a circular cylinder. *Journal of Fluids and Structures* **19-4**: 491–510.
- Lupandin AI. (2005). Effect of flow turbulence on swimming speed of fish. *Biology Bulletin* **3-5**: 461–466.
- Lythgoe J and Lythgoe G. (1991). *Fishes of the Sea: The North Atlantic and Mediterranean*. Cambridge: Massachusetts Institute of Technology Press, 256pp.
- Nelson J. (1976). *Fishes of the World*. New Jersey: John Wiley & Sons, 416pp.
- Phillips AB, Blake JL, Smith B, Boyd SW and Griffiths G. (2010). Nature in engineering for monitoring the oceans: towards a bio-inspired flexible autonomous underwater vehicle operating in an unsteady flow. In: Proceedings of IMechE Part M: *Journal of Engineering for the Maritime Environment* **224**: 267–278.
- Przybylla A, Kunze S, Rudert A, Bleckmann H and Brücker C. (2010). Entraining in trout: a behavioural and hydrodynamic analysis. *Journal of Experimental Biology* **213**: 2976–2986.
- Salumäe T. (2010). Design of a compliant underwater propulsion mechanism by investigating and mimicking the

- body of a rainbow trout (*Oncorhynchus mykiss*), MS Thesis, Tallinn University of Technology. Available at [www.ttu.ee/public/i/infotehnoloogia-teaduskond/Instituudid/biorobootika/teadus/projektid/tudengite\\_projektid/paindlik\\_uim/Taavi\\_Salumae\\_-\\_MSc\\_Thesis\\_2010.pdf](http://www.ttu.ee/public/i/infotehnoloogia-teaduskond/Instituudid/biorobootika/teadus/projektid/tudengite_projektid/paindlik_uim/Taavi_Salumae_-_MSc_Thesis_2010.pdf), last accessed <28 April 2014>.
- Sveen JK. (2004). MatPIV – the PIV toolbox for MATLAB®. Available at <http://folk.uio.no/jks/matpiv/index2.html> last accessed <28 April 2014>.
- Taguchi M and Liao JC. (2011). Rainbow trout consume less oxygen in turbulence: the energetics of swimming behaviors at different speeds. *Journal of Experimental Biology* **214**: 1428–1436.
- Toming G, Salumäe T, Ristolainen A, Visentin F, Akanyeti O and Kruusmaa M. (2012). Fluid dynamics experiments with a passive robot in regular turbulence. In: Proceedings of IEEE International Conference on Robotics and Biomimetics (ROBIO), 532–537.
- Triantafyllou MS, Triantafyllou GS and Yue DKP. (2000). Hydrodynamics of fishlike swimming. *Annual Review of Fluid Mechanics* **32**: 33–53.
- Visentin F, Fiazza MC, Akanyeti O, Venturelli R and Fiorini P. (2011). Towards flow-sensing robots: situated analysis for PIV flow imaging. In: Proceedings of IEEE 15th International Conference on Advanced Robotics (ICRA), 606–612.
- Wang SY, Jia LB and Yin XZ. (2009). Kinematics and forces of a flexible body in Karman vortex street. *Chinese Science Bulletin* **54**: 556–561.
- Webb PW. (1998). Entrainment by river chub *Nocomis Micropogon* and smallmouth bass *Micropterus Dolomieu* on cylinders. *Journal of Experimental Biology* **201**: 2403–2412.
- Zdravkovich MM. (1997). *Flow Around Circular Cylinders: a Comprehensive Guide Through Flow Phenomena, Experiments, Applications, Mathematical Models, and Computer Simulations*. Oxford Science Publications. Oxford: Oxford University Press, 672pp.
-



## **Appendix C**

J. A. Tuhtan, G. Toming, T. Ruuben, and M. Kruusmaa, “A method to improve instationary force error estimates for undulatory swimmers,” *Underw. Technol.*, vol. 33, no. 3, pp. 141–151, 2016.



# A method to improve instationary force error estimates for undulatory swimmers

Jeffrey A. Tuhtan\*<sup>1,2</sup>, Gert Toming<sup>2</sup>, Toomas Ruuben<sup>3</sup> and Maarja Kruusmaa<sup>2</sup>

<sup>1</sup>SJE Ecohydraulic Engineering, GmbH, 70569 Stuttgart, Germany

<sup>2</sup>Centre for Biorobotics, Tallinn University of Technology, 12618, Tallinn, Estonia

<sup>3</sup>Department of Radio and Communication Engineering, Tallinn University of Technology, 12618, Tallinn, Estonia

Received 2 October 2015; Accepted 6 January 2016

## Abstract

Our aim is to improve the analysis of the force dynamics common to experimental investigations of oscillatory locomotion in underwater research. This paper proposes a new method for instationary force error modelling and correction, calibrating on a passive body at laboratory scale. The calibration function is applied to instantaneous force estimates during undulatory swimming under turbulent flow conditions. The main advantage of this method is automated phase shift correction. This study uses a force plate to directly obtain the instantaneous streamwise and lateral forces on a passive and actuated fish robot under turbulent flow conditions. Force estimates are simultaneously obtained using the momentum deficit method, coupled for the passive case using a linear transfer function. The resulting instantaneous error model is evaluated in three turbulent flow experiments, during which the robot is actuated to mimic a swimming fish. Mean, median and modulo general linear transfer functions are evaluated to determine the best performing general function. Actuated instantaneous force estimate errors are reduced by 64%–93% in the streamwise and 75%–91% in the transverse directions. It was found that all three transfer functions had similar performance, considering the instationary force estimates during actuation. The modulo function performed best for the passive case.

**Keywords:** undulatory swimming, underwater robotics, biorobotics, force measurement, momentum deficit, particle image velocimetry

## 1. Introduction

Capturing the dynamics of undulatory swimmers such as fish requires accurate estimates of time-dependent forces. Fluid field measurements using

particle image velocimetry (PIV) provide data with high temporal and spatial resolution, allowing for the detailed analysis of fluid-body interactions (Drucker and Lauder, 1999). Direct measurements under turbulent flow conditions are extremely difficult and impractical; however, it is possible to estimate the instantaneous forces by extracting information from their wake (Brücker and Bleckmann, 2010; Shelton et al., 2014).

In order to carry out instantaneous force estimates for undulatory swimmers, it is necessary to apply a non-invasive measurement method. Previous studies have successfully applied the momentum deficit method to estimate the forces acting on swimming and flying insects, fish and biorobots. These works have evaluated alternate calculation methods for time-dependent dynamic forces and have applied the method in conjunction with numerical simulations to study drag, thrust and power requirements of swimming fish (Schultz and Webb, 2002). A similar work using the wake momentum flux approach has also been applied to study the linear acceleration of eels (*Anguilla rostrata*; Tytell, 2004). The study of an idealised hawkmoth (*Manduca sexta*) wake indicates that the onset of turbulence may place an upper limit on estimation accuracy using the momentum deficit approach, as optimal accuracy was achieved when the circulation and impulse were still laminar (Tytell and Ellington, 2003).

Depending on the experimental setup and flow conditions, the method is capable of delivering highly accurate force estimates. Aerodynamic force estimates using a 3D PIV setup whose control volume enclosed a pair of sinusoidal flapping wings achieved errors as low as 6% for instantaneous streamwise forces (Sällström and Ukeiley, 2014).

\* Contact author. Email address: [tuhtan@sjeweb.de](mailto:tuhtan@sjeweb.de)

The estimated error of the mean thrust per cycle of a mechanical lamprey using the momentum deficit approach was found to be 27% (Leftwich and Smits, 2011). Direct measurements of instantaneous forces under turbulent flow conditions and their role on fish swimming performance require further investigation, especially when studying rheophilic families such as salmonids (Lacey et al., 2012; Smith et al., 2014).

Undulatory locomotion is driven by complex fluid-body interactions that result in the production of a convectively unstable jet-like wake (Triantafyllou et al., 1993). The average flow properties of the swimmer's wake include semi-regular vortices whose shedding frequency closely matches that of the tailbeat. Due to the oscillatory body motion, the wake of the swimmer is not the only point of interest. It has been demonstrated that some fish (Liao et al., 2003), and more recently autonomous underwater vehicles, may be capable of exploiting the alternating vortices directly downstream of a fixed obstruction, reducing the cost of transport (Phillips et al., 2015). Whether using live specimens or robots, a methodology that accurately measures the instantaneous forces experienced by oscillatory swimmers is required.

In this work, instantaneous estimates of the body force magnitudes are obtained using a detailed accounting of the momentum deficit in a control volume surrounding the swimmer. By defining the control volume as a rectangular region around the body and extending it into the wake, the forces can be estimated by relating the rate of change of momentum to the sum of the forces. The noninvasive approach is based on Newton's second law, which equates the sum of forces to the time rate of change of momentum using a control volume enveloping the swimming fish and a portion of its wake.

The use of an ideal control volume requires several assumptions: uniform freestream velocity and pressure conditions; negligible viscous dissipation along the boundaries; incompressibility; and uniform fluid density. When these conditions are held, then the loss of linear momentum is equal to the difference in static pressure and linear momentum within and through the control volume surface. However, it is not possible to simultaneously satisfy all of these conditions, and an exact estimation of the forces is limited by the boundary conditions, the enforcement of continuity, and the neglected pressure and angular momentum terms (Takahashi, 1997). As the control volume approach can never achieve ideal conditions, there will always be an error associated with the momentum deficit force estimates, which are based on the balance of linear momentum.

Because of the exchange between linear and angular momentum, the linear momentum should be considered as inherently non-conservative, especially for complex turbulent flows (Davidson, 2004). Additionally, the assumption of strict conservation is incorrect owing to the 2D approximation of the 3D control volume. This can be observed directly by creating visualisations of planar velocity field divergence, which illustrate the degree to which complex out-of-plane fluxes occur within a control volume containing a swimming fish's wake (Hanke and Bleckmann, 2004).

In turbulent flows, random fluctuations, vorticity, stretching and shearing are the physical mechanisms behind the complexity of the fluid field (Okubo, 1970). Ultimately, the exact measurement of turbulent flows and their resulting interactions is an impossible task. The primary sources of error using the proposed approach are: the phase-shift between measured and estimated forces; the use of an idealised control volume covering only the tail and wake regions; and the use of a single 2D plane to recover the velocity field. Given the wide variety of possible experimental setups for which this method may be suitable, it is necessary to develop laboratory methods that allow for error correction which can be applied independently of a particular setup. Through the use of a calibrated transfer function between measured and estimated forces, this study shows that it is possible to consistently reduce the errors of a typical setup using a flow tunnel, undulatory swimmer and 2D PIV. The method is shown to work under turbulent flow conditions.

In this study, PIV is used to noninvasively monitor the wake of a robotic fish mounted to a force plate under both passive and actuated conditions in a turbulent flow. Instantaneous force estimates using the momentum deficit method were directly compared to measured values using a submerged force plate. A general linear transfer function was calibrated using a passive body for a range of freestream velocities and subsequently applied to correct the momentum deficit estimate errors during undulatory actuation of the same body. Our motivation in developing this method was to improve instantaneous force estimates using a calibrated transfer function for a given experimental setup.

## 2. Materials and methods

---

### 2.1. Flow tunnel and particle image velocimetry setup

All experiments were conducted in a closed, fully submerged flow tunnel with a working section of

0.5 m × 0.5 m × 1.5 m. An AC motor and frequency converter were used to generate flow speeds from 7.5 cm/s–50 cm/s. The digital PIV system is from Dantec Dynamics (Dantec Dynamics A/S, Skovlunde, Denmark). It consists of a SpeedSense M310 camera with a resolution of 1280 × 800 pixels and has a maximum frame rate of 3260 Hz. The light source used was a continuous 5 W, 532 nm laser Ray Power 5000. DynamicStudio 3.41 was used for data acquisition and pre-processing. Polyamide particles from Vestosint 1101 (Evonik Industries AG, Essen, Germany) with an average diameter of 100 μm were used for flow seeding. The camera was placed above the flow tunnel, and the laser and light sheet optics were placed lateral to the flow at the height of the fish's midline, creating a light sheet perpendicular to the camera's field of view (Fig 1).

Including fully turbulent flow in the analysis was of particular interest, as the study of fluid-body interactions between the undulatory swimmer and a turbulent flow field allows for more complete coverage of conditions *in natura*. In this work, the experimental fish robot was actuated at constant frequency, while being exposed to grid turbulence in a close rectangular channel (Fig 1). The turbulent properties of the flow were kept constant via the motor controller and passing the flow through

two collimators immediately before the flow tunnel entrance. The fish robot was mounted on a platform and placed in the geometric centre of the flow tunnel, with the body oriented parallel to the streamwise walls. It is worth noting that during the experiments, the water surface elevation in the tank is subject to centimetre-scale variations in depth, which cause variation in the pressure distribution within the closed tunnel. Thus the total instantaneous force experienced by the undulatory swimmer is also expected to vary with the pressure fluctuations in the flow tunnel.

## 2.2. Experimental fish biorobot

In the study, a 50 cm long fish robot was used (Fig 2) with 30 cm compliant tail that mimics the swimming and geometry of a rainbow trout (*Oncorhynchus mykiss*; Kruusmaa et al., 2014). The robotic fish is self-actuated using an internal servo motor with a fixed actuation (resonance) frequency of 2 Hz and variable tail actuation envelope. As the fish was designed for optimal control using a linear relation between the swimming speed and actuation envelope, the Strouhal number is much higher than that found in live fish and flapping foils, which have a typical range of 0.2–0.4 (Nudds et al., 2014; Triantafyllou et al., 1991, Triantafyllou et al., 1993).

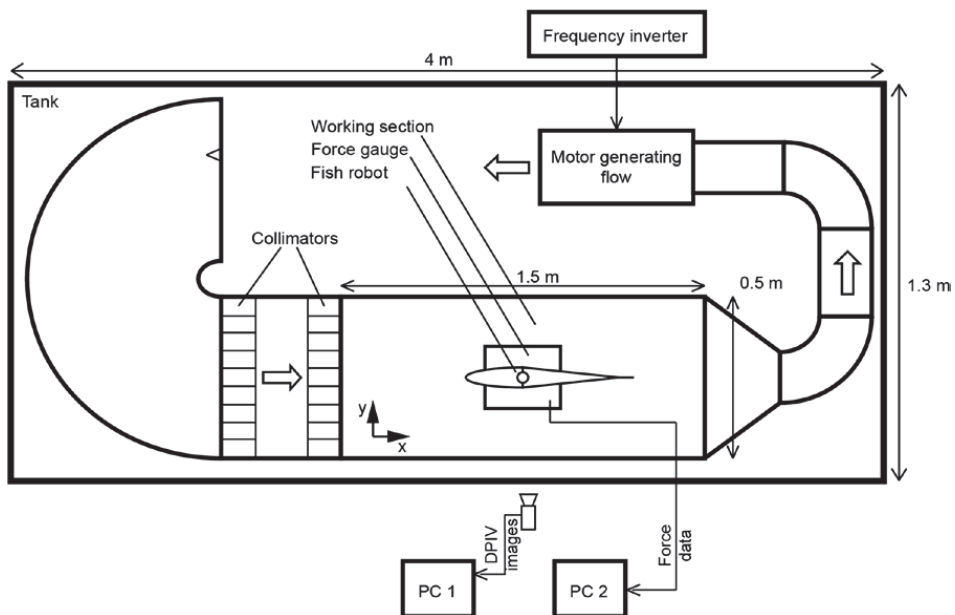


**Fig 1:** Experimental setup in the flow tunnel. View from above. The fish robot was placed in the centre of the flow tunnel working section and subjected to a uniform freestream velocity field (flow from left to right). Homogeneous turbulence in the upstream flow is produced by discharging the water through two collimators placed directly upstream of the working section.

### 2.3. Force plate

A custom-built submerged force plate was used to measure the hydrodynamic forces affecting the fish robot and forces created by the robot. The force plate consists of four load cells placed at the corners of a horizontal plane, making it possible to measure the instantaneous streamwise force ( $F_x$ ) and lateral force ( $F_y$ ) (Fig 3). All signals from the load cells are amplified using a Texas Instruments INA128 (Texas Instruments, Dallas, Texas, USA) and digitised with a 16-bit analogue-to-digital converter LTC1867 (Linear Technology, Milpitas, California, USA). The signals are collected with an Atmel Atmega328 microcontroller (Atmel Corporation, San Jose, California, USA) and transferred

to a desktop PC via RS-232 connection. The force plate was calibrated using a Lutron FG-5000A force gauge (Lutron Electronic Enterprise CO., Taipei, Taiwan) and its performance was characterised using five fixed loads from 0.9913 N to 4.8761 N. Each measurement was performed ten times, resulting in standard error ranges of 0.1% to 0.39% of the mean for  $F_x$ , and 0.08% to 0.43% of the mean for  $F_y$  (Toming et al., 2014).

### 2.4. Experimental setup and procedure

All experiments were conducted within the flow range of 0 cm/s to 20 cm/s. After switching on the AC motor, a minimum of 60 s was allowed to pass in order to let the flow in the working section to fully

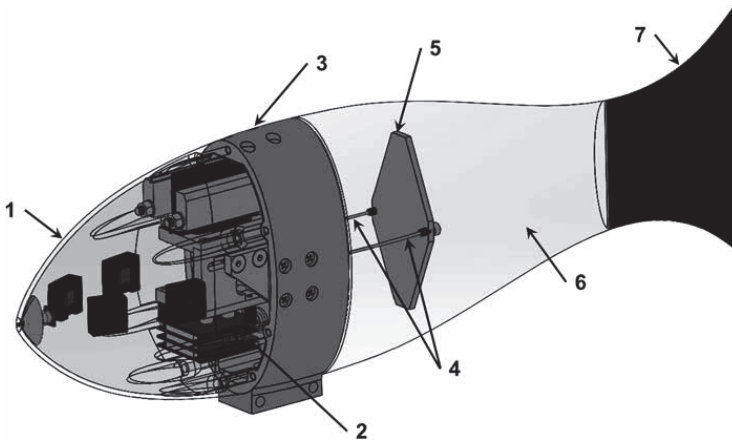


**Fig 2:** Computer-aided design (CAD) drawing of the actuated robotic fish: (1) rigid head, (2) servo motor, (3) machined body cavity, (4) steel connectors, (5) actuation plate, (6) compliant tail and (7) rigid fin.

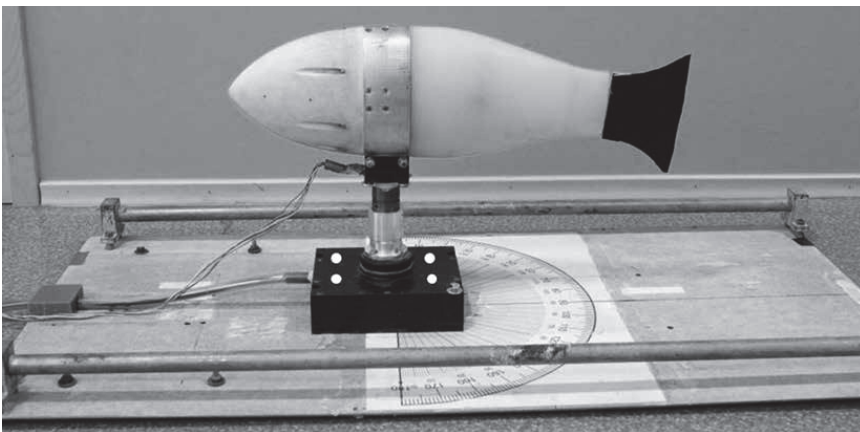


**Fig 3:** Fish robot affixed to force plate. The location of the eight load cells located within the housing are indicated as white dots. Two sets of four cells were stacked on top of each other; one set was used to record the instantaneous lateral and streamwise forces, and the other for measuring the torque.

develop and stabilise. Two desktop PCs were used to capture the data. The first PC was used to record the PIV imagery from the camera placed on top of the flow tunnel. On the second PC, LabVIEW 10.0.1 (National Instruments, Austin, Texas, USA) was used to control the fish robot and record the data from the pressure sensors and force plate. The computers were synchronised using Dantec Timer Box and the NI PCIe-6363 data acquisition device. All experiments were performed over a 10 s sampling interval. The PIV measurements were taken at 400 Hz, and the force plate measurements were taken at 80 Hz for all flow experiments. Comparison between the measured and estimated forces was performed for all datasets over 10 continuous tailbeats within a 5 s window, excluding the first two tailbeats.

2.5. Passive experiments

In order to compare the effects of different freestream flows on the error estimation method, it was necessary to use identical flow conditions for both passive and actuated experiments. During all passive experiments, the robotic fish was fixed to the force plate and inserted into the flow tunnel directly in the PIV field of view (Fig 4). Once placed in the flow tunnel, constant flow conditions were set and the force plate data were recorded simultaneously with the PIV imagery. The passive experiments were performed to generate momentum deficit estimates without any body motion. These data were used to create the linear transfer functions. Thus the proposed methodology requires only that a geometrically similar static body be placed in the experimental setup for PIV and force analysis prior to the consideration of a swimming body. This allows for calibration of a given experimental setup based on a passive body for actuated (swimming) body.

2.6. Actuated experiments

Using the identical setup for the passive experiments, three additional experiments with constant flow conditions were carried out using the actuated robot. The robot body and actuation parameters of tailbeat frequency and amplitude envelope have been optimised for steady swimming over a fixed range of flow speeds from 0 cm/s to 20 cm/s (Salumäe and Kruusmaa, 2013). The chosen flow speeds were 10 cm/s, 15 cm/s and 20 cm/s, as they are within the fixed range and within the rheotactic thresholds for many migrating fish (Pavlov, 1989).

3. Data processing

3.1. Momentum deficit formulation

The instantaneous forces are estimated by relating the rate of change of momentum to the sum of the forces using the integral form of the momentum equation. As an example, the integral formulation of the momentum balance in the streamwise direction assuming only horizontal flow ( $v = 0$ ), taken within the control volume ( $\forall$ ) over surfaces 3 and 1 (Fig 4, up and downstream of the submerged body, respectively) can be expressed as:

$$F = -\rho \int \frac{du}{dt} d\forall + \rho \int (u_3^2 - u_1^2) dz_1 + \int (p_3 - p_1) dz_1 \tag{1}$$

where  $F$  is the streamwise force,  $\rho$  is the fluid density,  $u$  the streamwise velocity vector component,  $t$  is the time,  $z_1$  is the vertical elevation with constant reference and  $p$  is the pressure at the boundaries.

In this paper, the same formulation is applied as that in previous works for a swimming robotic lamprey, which makes use of a planar, discreet

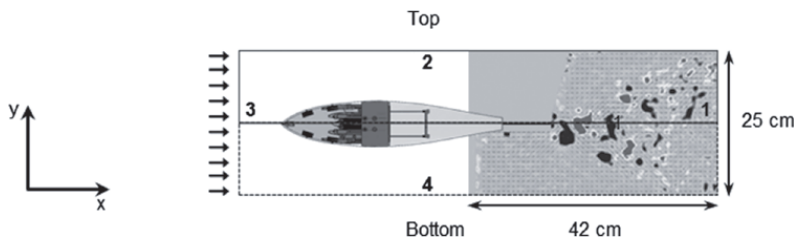


**Fig 4:** Placement of the control volume surfaces 1–4 for the measured (black dashed) and mirrored, phase-shifted (solid black) regions. Surface 3 is approximated as having a constant freestream velocity, Surfaces 2 and 4 extend only partially along the body, Surface 1 is extended as far in the streamwise direction as possible. The majority of the control volume surface was located downstream of the swimming body. The outer grey line indicates the boundary of the flow tunnel walls.

approximation of the integral formulation, including streamwise and lateral velocity components (Leftwich and Smits, 2011; Leftwich et al., 2012):

$$\begin{aligned} \Delta M_x(t) = & \sum_1 \rho u^2 \Delta L + \sum_2 \rho uv \Delta L - \sum_3 \rho u^2 \Delta L \\ & - \sum_4 \rho uv \Delta L + \frac{1}{2\Delta t} \left[ \left( \sum_x \sum_y \rho u \Delta L^2 \right)_{i+1} \right. \\ & \left. - \left( \sum_x \sum_y \rho u \Delta L^2 \right)_{i-1} \right] \end{aligned} \quad (2)$$

where  $\Delta M_x(t)$  is the instantaneous streamwise momentum flux,  $u$  is the streamwise velocity,  $v$  is the lateral velocity,  $\Delta L$  is the pixel size and  $\Delta t$  is the PIV recording frequency.

The corresponding equation in the lateral direction can also be applied to estimate the lateral momentum flux ( $\Delta M_y(t)$ ). Note that due to the pixels having the same dimensions in both the streamwise and lateral directions, the equation simplifies to  $\Delta L_x = \Delta L_y = \Delta L$ . This study also followed Leftwich et al. (2012) by assuming symmetry; the right side of the control volume was not measured directly but simulated using the mirrored, phase-shifted PIV results from the left half (Fig 4). It is also worth noting that the discrete formulation does not include the contribution of the pressure difference over the control volume, thus introducing a systematic error in the dynamic force estimate.

### 3.2. Transfer function design for instantaneous force estimate error

The first step in error estimation is to find a set of transfer functions between the time-dependent measured streamwise and lateral forces ( $F_x(t)$  and  $F_y(t)$ ), and the momentum deficit force estimates ( $\Delta M_x(t)$  and  $\Delta M_y(t)$ ). The error between the measured and estimated values can range from a few percentage points in the streamwise direction to well over 50% in the lateral (Table 1). The objective is to determine a general transfer function, which permits robust estimations of  $F_C(t)$  based on  $\Delta M(t)$  for experiments without direct force measurements.

The relationship between  $F(t)$  and  $\Delta M(t)$  is calculated using the convolution theorem with the impulse response  $h(t)$ :

$$F(t) = \int_{-\infty}^{\infty} \Delta M(v)h(t-v)dv \quad (3)$$

The Fourier transform (*FFT*) is used to generate the transfer function ( $H(f) = FFT[h(t)]$ ) in the frequency domain between the measured force plate signal ( $F(f)$ ) and the momentum deficit estimate ( $\Delta M(f)$ ). The Fourier transform allows for the complete description of periodic and nonperiodic discrete signals as sums of sine and cosine functions (Burger and Burge, 2011). The difference between force measurements and estimates can thus be converted and recovered with almost perfect accuracy. This formulation also provides for a direct transformation of the signals from the frequency domain to the time domain using the inverse Fourier transform:

$$F(t) = FFT^{-1}[F(f)] \quad (4)$$

In case the relationship between the signals  $F(t)$  and  $\Delta M(t)$  is linear, it should be possible to find the transfer function  $H(f)$  such that:

$$H(f) = \frac{F(f)}{\Delta M(f)} \quad (5)$$

In this work, transfer functions are created individually for all flow experiments and separately for both the streamwise and lateral forces. As an example, for the turbulent flow experiments, separate calculations are first performed for all three flow velocities, and the set of transfer functions  $H_{10}(f)$ ,  $H_{15}(f)$  and  $H_{20}(f)$  are calculated. The successful conversion of both the lateral and streamwise components confirms the linear relationship between measured and estimated forces. The final step is to find a general transfer function for each set of experiments  $H(H_{10}, H_{15}, H_{20})$ , such that the estimates of  $F(t)$  from  $\Delta M_x(t)$  are as accurate as possible, independent of the flow speed chosen in the experimental setup.

**Table 1:** Phase 1, passive force experiment results comparing the measured mean forces and momentum deficit estimates. Errors are expressed as a percentage of the mean force over 5 s (2000 force estimates).

Freestream velocity (cm/s)	Mean streamwise force, $F_x$ (mN)	Mean lateral force, $F_y$ (mN)	Standard error $F_x$ (%)	Standard error $F_y$ (%)
10	60	20	6	14
15	90	20	6	17
20	140	30	9	40
25	210	40	7	46
30	300	50	9	61
35	380	40	7	69

This study tested three possible functions based on the mean, medium and modulo of the individual transfer functions. It can be seen that the transform from momentum deficit to force plate readings is substantially improved using the general functions (Fig 5), with the modulo transfer function performing the best for both the passive

and actuated flow experiments (Tables 2 and 3). The modulo transfer function had the largest reduction in error for half of the trials and was only significantly outperformed by the median in one case ( $F_x$ , 15 cm/s). The manual phase-shift correction was done using a constant offset of 0.25 s, 0.225 s and 0.1625 s for 10 cm/s, 15 cm/s and

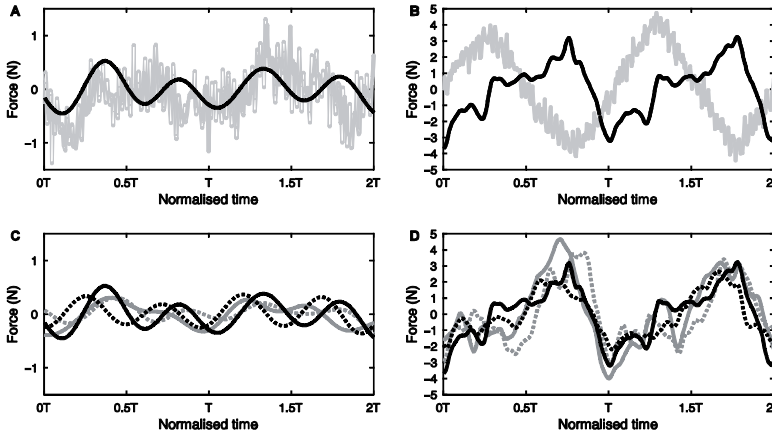


**Fig 5:** Comparison of instantaneous force measurements, momentum flux estimates and general transfer functions for the turbulent flow experiment at 15 cm/s: (a) measured streamwise forces ( $F_x$ , black) and the momentum deficit estimates  $\Delta M_x$ , grey) for two tail beat cycles; (b) measured lateral forces ( $F_y$ ) and the momentum deficit estimates ( $\Delta M_y$ ); (c) measured (solid black) streamwise forces compared with the mean (solid grey), modulo (dashed black) and median (dashed grey) general transfer functions; and (d) comparison of measured and lateral general transfer function results for the instantaneous lateral forces. The time scale is normalised to the tailbeat period ( $T$ ).

**Table 2:** Error reductions for phase 1, passive flow experiments after applying the transfer functions. Results are expressed as the percentage reduction of the phase-averaged momentum deficit error over 10 tailbeat cycles. Values in bold have the lowest error of all three general transfer functions tested. The modulo transfer function outperformed the median and mean in all but two cases.

Freestream velocity (cm/s)	Median standard error reduction (%)		Mean standard error reduction (%)		Modulo standard error reduction (%)	
	$F_x$	$F_y$	$F_x$	$F_y$	$F_x$	$F_y$
10	36	47	18	42	22	53
15	20	49	20	31	47	61
20	18	59	14	50	26	68
25	45	77	16	70	63	83
30	33	75	42	42	41	83
35	49	77	24	69	69	81

**Table 3:** Error reductions for phase 2, actuated experiments. Results are expressed as the percentage reduction of the phase-averaged error. Values in bold have the lowest error of all three general transfer functions tested.

Freestream velocity (cm/s)	Median standard error reduction (%)		Mean standard error reduction (%)		Modulo standard error reduction (%)		Manual phase-shift correction (%)	
	$F_x$	$F_y$	$F_x$	$F_y$	$F_x$	$F_y$	$F_x$	$F_y$
10	79	89	73	88	81	89	88	41
15	88	87	64	91	79	91	98	59
20	68	75	93	87	68	78	93	54

20 cm/s, respectively. The offset was determined by manually matching the peak-to-peak amplitudes of 10 consecutive tailbeat cycles of the estimated and measured lateral forces.

This study shows that the use of the general linear transfer function has two advantages over using the momentum deficit estimates directly. The first advantage is that the function can be applied to model force estimate errors for experiments where direct measurements cannot be performed. The second is that the transfer function itself provides a dynamic mapping of the error between estimated and measured forces in the frequency domain, which when converted back into the time domain automatically corrects any phase shift in the original signals.

#### 4. Results

The experiments were carried out in two phases. In the first phase, the fish was fixed to the force plate in the flow tank and was passively (zero body motion) exposed to a range of velocities from 10 cm/s to 35 cm/s in 5 cm/s intervals. The second phase included a set of three actuated experiments in the flow tank at 10 cm/s, 15 cm/s, and 20 cm/s at Reynolds numbers of  $5 \times 10^4$ ,  $7.5 \times 10^4$  and  $10 \times 10^4$ , respectively (Table 4). The signals from the passive phase were used to create calibrated, general linear transfer functions for use in the actuated phase.

In both sets of experiments the fish body remained at the same location in the tank. The streamwise and lateral force errors were compared with the momentum deficit estimates for both datasets (Tables 2 and 3). Principally, the errors between signals occur as a result of the simplifying assumptions and due to the phase shift and distortion of the momentum deficit estimate signal. As the method relies on the analysis of a control volume, including the flow around the body as well as portion of the wake, the instantaneous force estimates cannot perfectly reproduce the forces. Phase shifting is required in order to correct for time lag and signal stretching between the measured forces as experienced by the undulating swimmer. In cases

where both direct measurements and estimates exist, the phase shift for each experiment can be calculated empirically using the phase-averaged lag between measured and estimated force peaks. In cases where a test subject is swimming and direct forces are unknown, the phase shift is removed automatically using a calibrated linear transfer function.

The time-averaged error over a 5 s period as a percentage of the mean force was determined for all passive flow experiments. Additionally, the percent reduction in the standard error as compared to the momentum deficit estimate was calculated. Time-averaged errors for the passive flow experiments ranged from 6% to 9% in the streamwise direction, and from 14% to 69% in the lateral direction (Table 1).

After calibration of the individual transfer functions was carried out for each individual experiment (10 cm/s – 35 cm/s), the general mean, median and modulo transfer functions were applied to all passive experiments. Using the general transfer functions resulted in a reduction of the time-averaged error for all experiments, considering both the streamwise and lateral forces. In 10 out of 12 experiments (Table 2), the modulo general transfer function resulted in the largest error reduction. The streamwise force error was reduced by 22%–69% and the lateral by 53–83% using the modulo function. Mean and median functions lead to error reduction in all cases, but generally exhibited lower performance than the modulo function. Thus, the use of a modulo general transfer function for passive flow experiments is recommended in future work.

The actuated experiments had phase-averaged errors from 100% to 106% in the streamwise direction, and from 90% to 108% in the lateral direction (Table 3). The large difference in errors for the passive and actuated cases is a result of the phase shift between the measured and estimated forces. After applying the calibrated, general transfer functions based on the passive flow experiments, the percent reduction in force estimate errors were calculated for the three actuated experiments. In contrast to the passive flow experiments where the

**Table 4:** Experimental parameters for turbulent flow experiments, passive and actuated. The turbulence properties for the active and passive cases are identical for the three actuated cases.

Freestream velocity (cm/s)	Tailbeat frequency (Hz)	Tail actuation envelope (cm)	Strouhal number (-)	Turbulence intensity (-)	Turbulence kinetic energy (J/kg)	Reynolds number (-)
10	2	6.5	1.30	0.59	5.4 E-03	5 E+04
15	2	14.3	1.91	0.61	11 E-03	7.5 E+04
20	2	22.1	2.21	0.62	19 E-03	10 E+04
25	–	–	–	0.58	23 E-03	12.5 E+04
30	–	–	–	0.58	36 E-03	15 E+04
35	–	–	–	0.58	49 E-03	17.5 E+04

modulo general transfer function exhibited superior performance, the error reduction observed for the actuated experiments was generally similar for the mean, median and modulo general transfer functions. Considering all transfer functions, the errors were reduced by 64%–93% for streamwise and 75%–91% for lateral forces. As no clear trend could be observed, any of the three functions may be chosen for error modelling and correction of undulatory experiments.

## 5. Discussion

In order to estimate the momentum deficit, a predictive filter transformation was applied to each experiment individually. The individual transformations were then combined and compared to the measured forces to create mean, median and modulo general transformation functions which could be applied independently of the freestream velocity.

The time-averaged mean of instantaneous force estimates for the passive flow experiments in the streamwise direction remained less than 10% over the full range of freestream velocities. In contrast, the lateral force errors increased steadily with increasing velocity. Lateral force estimates had response signals that often appeared vertically stretched (scaled) relative to the measured values. Although the body was fixed to the force plate, it did possess a limited ability (mm) to surge in the streamwise direction and sway in the lateral direction. The local motions of the body translate to an acceleration of the surrounding fluid, increasing the apparent mass of the body (Tytell, 2004). Thus, a possible cause of larger lateral errors for the passive instantaneous forces is the added mass effect caused by the robotic fish's body motion, which is not completely inside the control volume (Figs 4 and 6). The added mass effect is partially considered in the unsteady, inertial term of the idealised momentum deficit formulation used in this work. Thus, the missing PIV data along the ventral portion of the control volume can be reasonably expected to contribute to the instantaneous force estimate error.

The actuated flow trials had larger errors than the passive experiments and correspondingly larger error reductions after the transfer functions were applied. Considering the identical experimental setup, this study proposes that the phase shift caused by the moving water may be one reason why the results were significantly different between the passive and actuated cases.

In the passive flow case, the wake signal remained relatively constant over time and was advected and dispersed into the downstream flow at a speed slightly lower than the freestream velocity. A strong

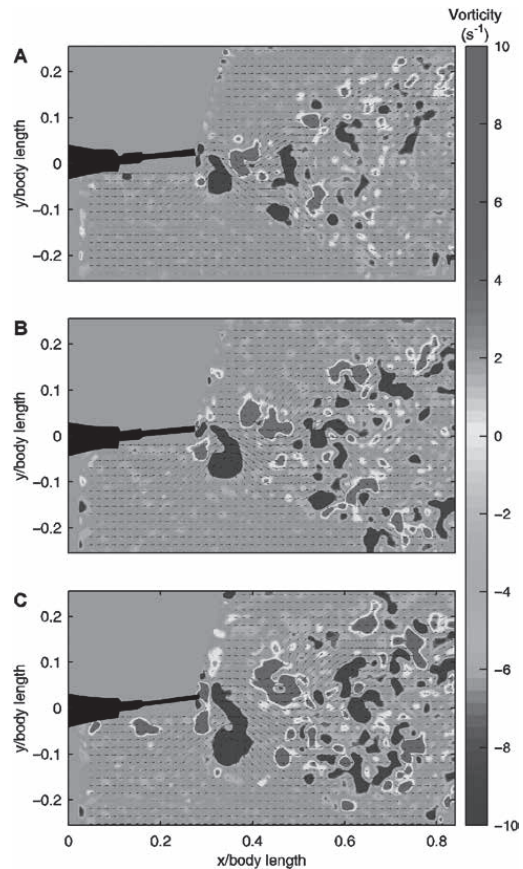


**Fig 6:** Wake of the actuated robotic fish under turbulent flow conditions for (a) 10 cm/s, (b) 15 cm/s, and (c) 20 cm/s. The tail in each image is at the end of its upward beat, and has been traced from the PIV imagery as a black silhouette. Flow direction is from left to right. Arrows indicate the direction of flow and are unscaled. The vorticity contours are shown using the same range.

phase-shift was observed for all turbulent flow experiments, and must be corrected when performing the comparison between measured and estimated instantaneous forces (Fig 7). Thus, an additional component of the calibration procedure for undulatory swimming experiments is to determine the phase-shift required to correct the momentum deficit force estimates along the time axis. Such a correction can be especially critical for the interpretation of instantaneous force estimates of biological specimens, since their behaviour is much more unpredictable than that of the highly controlled fish robot body motion used in this study (Fig 8). An additional benefit of using the transformation functions is their automated correction of the phase-shift between measured and estimated force signals.

Results for the passive flow experiments after applying the three transfer functions clearly show that the modulo filter performed the best in 10 of

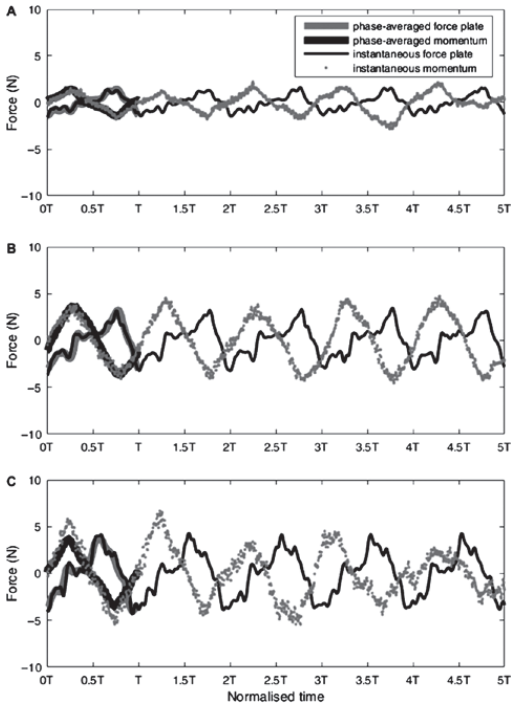


**Fig 7:** Comparison of instantaneous and phase-averaged lateral forces ( $F_y$ ) for the three actuated experiments: (a) 10 cm/s, (b) 15 cm/s, and (c) 20 cm/s. The time scale is normalised to the tailbeat period ( $T$ ). Phase-averaging was carried out over 10 tailbeat cycles for all datasets. The phase-averaged results are superimposed on the instantaneous force traces for the first tailbeat cycle.

the 12 experiments, with the mean and median filters in one case each (Table 2). Across all passive water experiments, the modulo filter also exhibited the most robust performance, with standard errors within 50% of the measured force amplitude, and resulted in an average reduction of 28% in the streamwise force error and 30% in the lateral force error.

Error calculations for the three filters tested under actuated, turbulent flow conditions showed similar improvement to the passive experiments, with the modulo filter exhibiting the best performance (Table 3). Considering all actuated experiments, the modulo filter performed the best in three out of six force estimates – the mean twice and the median once. Considering the actuated experiments, a manual phase shift resulted in similar, and slightly better, force estimates in the streamwise force, but did not perform as well in the lateral forces. General linear transfer functions are able to correct for more than the phase shift, and thus the improved performance in the lateral direction is not unexpected.

### Acknowledgments

The research leading to these results has received funding from BONUS, the joint Baltic Sea research and development programme (Art 185), funded jointly by the European Union’s Seventh Programme for research, technological development and demonstration, and by the Academy of Finland (under the grant 280715), the German Federal Ministry for Education and Research (BMBF FKZ:03F0687A), and the Estonian Environmental Investment Centre (KIK P.7254 C.3255).

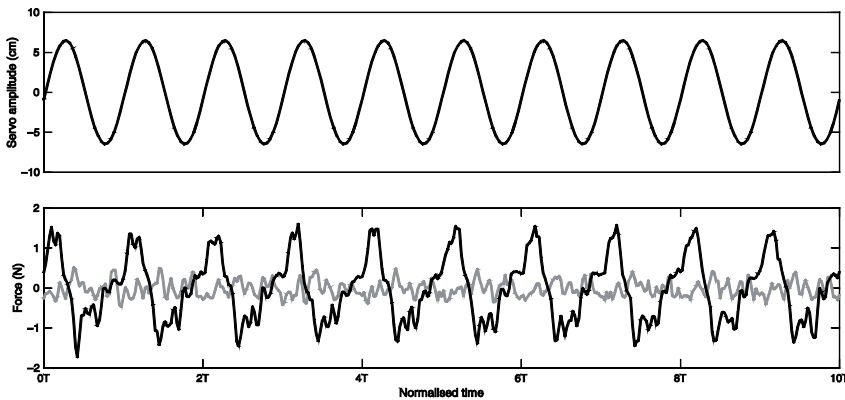


**Fig 8:** Comparison of servo motion (top) and instantaneous forces measured with the force plate (bottom) for the actuated experiment at 10 cm/s.  $F_x$  (grey) and  $F_y$  (black) over each cycle exhibited close similarity for the study owing to the use of a robotic fish, which moves in a highly repeatable manner.

## References

- Brücker C and Bleckmann H. (2010). Vortex dynamics in the wake of a mechanical fish. In: Taylor GK, Triantafyllou MS and Tropea C. (eds.) *Animal Locomotion*. Berlin Heidelberg: Springer, 61–172.
- Burger W and Burge MJ. (2011). *Principles of Digital Image Processing: Fundamental Techniques*. London: Springer, 327pp.
- Davidson PA. (2004). *Turbulence: An Introduction for Scientists and Engineers*. Oxford: Oxford University Press, 656pp.
- Drucker EG and Lauder GV. (1999). Locomotor forces on a swimming fish: three-dimensional vortex wake dynamics quantified using digital particle image velocimetry. *Journal of Experimental Biology* **202**: 2393–2412.
- Hanke W and Bleckmann H. (2004). The hydrodynamic trails of *Lepomis gibbosus* (Centrarchidae), *Colomesus psittacus* (Tetraodontidae) and *Thysochromis ansorgii* (Cichlidae) investigated with scanning particle image velocimetry. *The Journal of Experimental Biology* **207**: 1585–1596.
- Kruusmaa M, Fiorini P, Megill W, De Vittorio M, Akanyeti O, Visentin F, Chambers L, El Daou H, Fiazza M-C, Jezov J, Listak M, Rossi L, Salumae T, Toming G, Venturelli R, Jung DS, Brown J, Rizzi F, Qualtieri A, Maud JL and Liszewski A. (2014). FILOSE for Svenning: A Flow Sensing Bio-inspired Robot. *IEEE Robotics Automation Magazine* **21**: 51–62.
- Lacey RWJ, Neary VS, Liao JC, Enders EC and Triticco HM. (2012). The Ipos Framework: Linking Fish Swimming Performance in Altered Flows from Laboratory Experiments to Rivers. *River Research and Applications* **28**: 429–443.
- Leftwich MC and Smits AJ. (2011). Thrust production by a mechanical swimming lamprey. *Experiments in Fluids* **50**: 1349–1355.
- Leftwich MC, Tytell ED, Cohen AH and Smits AJ. (2012). Wake structures behind a swimming robotic lamprey with a passively flexible tail. *The Journal of Experimental Biology* **215**: 416–425.
- Liao JC, Beal DN, Lauder GV and Triantafyllou MS. (2003). Fish Exploiting Vortices Decrease Muscle Activity. *Science* **302**: 1566–1569.
- Nudds RL, John EL, Keen AN and Shiels HA. (2014). Rainbow trout provide the first experimental evidence for adherence to a distinct Strouhal number during animal oscillatory propulsion. *Journal of Experimental Biology* **217**: 2244–2249.
- Okubo A. (1970). Horizontal dispersion of floatable particles in the vicinity of velocity singularities such as convergences. *Deep Sea Research and Oceanographic Abstracts* **17**: 445–454.
- Pavlov DS. (1989). Structures Assisting the Migrations of Non-Salmonid Fish: USSR. Food and Agriculture Organization (FAO) Technical Paper No. 308. Rome: FAO, 97pp.
- Phillips AB, Blake JIR, Boyd SW and Griffiths G. (2015). Towards passive station holding of autonomous underwater vehicles inspired by fish behaviour in unsteady flows. *Proceedings of the Institution of Mechanical Engineers Part M Journal of Engineering for the Maritime Environment*.
- Sällström E and Ukeiley L. (2014). Force estimation from incompressible flow field data using a momentum balance approach. *Experiments in Fluids* **55**: 1–14.
- Salumäe T and Kruusmaa M. (2013). Flow-relative control of an underwater robot. *Proceedings of the Royal Society A: Mathematical, Physical and Engineering Science*. **469**: 20120671.
- Schultz WW and Webb PW. (2002). Power Requirements of Swimming: Do New Methods Resolve Old Questions? *Integrative and Comparative Biology* **42**: 1018–1025.
- Shelton RM, Thornycroft PJM and Lauder GV. (2014). Undulatory locomotion of flexible foils as biomimetic models for understanding fish propulsion. *Journal of Experimental Biology* **217**: 2110–2120.
- Smith DL, Goodwin RA and Nestler JM. (2014). Relating Turbulence and Fish Habitat: A New Approach for Management and Research. *Reviews in Fisheries Science and Aquaculture* **22**: 123–130.
- Takahashi T. (1997). On the decomposition of drag components from wake flow measurements. In: Proceedings of the American Institute of Aeronautics and Astronautics 35th Aerospace Sciences Meeting and Exhibit, 6–9 January, Reno, Nevada.
- Toming G, Chambers LD and Kruusmaa M. (2014). Experimental study of hydrodynamic forces acting on artificial fish in a von Kármán vortex street. *Underwater Technology* **32**: 81–91.
- Triantafyllou GS, Triantafyllou MS and Grosenbaugh MA. (1993). Optimal Thrust Development in Oscillating Foils with Application to Fish Propulsion. *Journal of Fluids and Structures* **7**: 205–224.
- Triantafyllou MS, Triantafyllou GS and Gopalkrishnan R. (1991). Wake mechanics for thrust generation in oscillating foils. *Physics of Fluids A: Fluid Dynamics (1989–1993)* **3**: 2835–2837.
- Tytell ED. (2004). Kinematics and hydrodynamics of linear acceleration in eels, *Anguilla rostrata*. *Proceedings of the Royal Society of London. Series B: Biological Sciences* **271**: 2535–2540.
- Tytell ED and Ellington CP. (2003). How to perform measurements in a hovering animal's wake: physical modeling of the vortex wake of the hawkmoth, *Manduca sexta*. *Philosophical Transactions of the Royal Society of London. Series B: Biological Sciences* **358**: 1559–1566.



## **Appendix D**

J. A. Tuhtan, J. F. Fuentes-Pérez, N. Strokina, G. Toming, M. Musall, M. Noack, J. K. Kämäräinen, and M. Kruusmaa, “Design and application of a fish-shaped lateral line probe for flow measurement”, *Review of Scientific Instruments*, vol. 87, no. 045110, pp.1–8, 2016.



## Design and application of a fish-shaped lateral line probe for flow measurement

J. A. Tuhtan, J. F. Fuentes-Pérez, N. Strokina, G. Toming, M. Musall, M. Noack, J. K. Kämäräinen, and M. Kruusmaa

Citation: *Review of Scientific Instruments* **87**, 045110 (2016); doi: 10.1063/1.4946765

View online: <http://dx.doi.org/10.1063/1.4946765>

View Table of Contents: <http://scitation.aip.org/content/aip/journal/rsi/87/4?ver=pdfcov>

Published by the AIP Publishing

---

### Articles you may be interested in

Using direct numerical simulation to analyze and improve hot-wire probe sensor and array configurations for simultaneous measurement of the velocity vector and the velocity gradient tensor

*Phys. Fluids* **25**, 110820 (2013); 10.1063/1.4821783

Experimental research of gas flows through isothermal and non-isothermal membranes

*AIP Conf. Proc.* **1501**, 824 (2012); 10.1063/1.4769627

Measurements and simulations of a channel flow powered by plasma actuators

*J. Appl. Phys.* **112**, 053303 (2012); 10.1063/1.4749250

Velocity measurement of flow through a model three-dimensional porous medium

*Phys. Fluids* **18**, 017105 (2006); 10.1063/1.2164847

Cyclic flow oscillations in a system of repeatedly branching channels

*Phys. Fluids* **10**, 877 (1998); 10.1063/1.869611

---



**JANIS** Does your research require low temperatures? Contact Janis today.  
Our engineers will assist you in choosing the best system for your application.



10 mK to 800 K      LHe/LN<sub>2</sub> Cryostats  
Cryocoolers      Magnet Systems  
Dilution Refrigerator Systems  
Micro-manipulated Probe Stations

[sales@janis.com](mailto:sales@janis.com)      [www.janis.com](http://www.janis.com)  
Click to view our product web page.

## Design and application of a fish-shaped lateral line probe for flow measurement

J. A. Tuhtan,<sup>1,2,a)</sup> J. F. Fuentes-Pérez,<sup>2</sup> N. Strokina,<sup>3</sup> G. Toming,<sup>2</sup> M. Musall,<sup>4</sup>  
M. Noack,<sup>5</sup> J. K. Kämäräinen,<sup>3</sup> and M. Kruusmaa<sup>2</sup>

<sup>1</sup>SJE Ecohydraulic Engineering GmbH, Viereichenweg 12, Stuttgart 70569, Germany

<sup>2</sup>Centre for Biorobotics, Tallinn University of Technology, Akadeemia tee 15A-111, Tallinn 12618, Estonia

<sup>3</sup>Department of Signal Processing, Tampere University of Technology, P.O. Box 553,  
Tampere FI-33101, Finland

<sup>4</sup>Institute of Water and River Basin Management, Karlsruhe Institute of Technology, Kaiserstraße 12,  
Karlsruhe 76131, Germany

<sup>5</sup>Institute for Modelling Hydraulic and Environmental Systems, University of Stuttgart, Pfaffenwaldring 61,  
Stuttgart 70569, Germany

(Received 20 October 2015; accepted 30 March 2016; published online 15 April 2016)

We introduce the lateral line probe (LLP) as a measurement device for natural flows. Hydraulic surveys in rivers and hydraulic structures are currently based on time-averaged velocity measurements using propellers or acoustic Doppler devices. The long-term goal is thus to develop a sensor system, which includes spatial gradients of the flow field along a fish-shaped sensor body. Interpreting the biological relevance of a collection of point velocity measurements is complicated by the fact that fish and other aquatic vertebrates experience the flow field through highly dynamic fluid-body interactions. To collect body-centric flow data, a bioinspired fish-shaped probe is equipped with a lateral line pressure sensing array, which can be applied both in the laboratory and in the field. Our objective is to introduce a new type of measurement device for body-centric data and compare its output to estimates of conventional point-based technologies. We first provide the calibration workflow for laboratory investigations. We then provide a review of two velocity estimation workflows, independent of calibration. Such workflows are required as existing field investigations consist of measurements in environments where calibration is not feasible. The mean difference for uncalibrated LLP velocity estimates from 0 to 50 cm/s under in a closed flow tunnel and open channel flume was within 4 cm/s when compared to conventional measurement techniques. Finally, spatial flow maps in a scale vertical slot fishway are compared for the LLP, direct measurements, and 3D numerical models where it was found that the LLP provided a slight overestimation of the current velocity in the jet and underestimated the velocity in the recirculation zone. *Published by AIP Publishing.* [<http://dx.doi.org/10.1063/1.4946765>]

### I. INTRODUCTION

Understanding the behavior of fish and other aquatic vertebrates requires data collection under controlled laboratory conditions as well as in the field. Even when data are available, the physical interpretation of hydrodynamic parameters and their relevance to observed fish behavior remains a major challenge to fluid mechanics researchers and aquatic biologists alike.<sup>1–4</sup> A significant problem is that current measurement techniques acquire flow field data neglecting the perceptive capabilities and fluid-body interaction experienced by the target organism.

The physical properties of the lateral line and its significance in flow sensing have been an active research topic for several decades.<sup>5,6</sup> Fisheries researchers began experimenting with electromechanical lateral line probes (LLPs) to study the acoustic and hydrodynamic properties of attracting and repelling flow conditions in the 1990s.<sup>7,8</sup> In addition, research on barotrauma experienced by fish

has resulted in the development of a second generation fish-sized device and has been successfully implemented in studies of the extreme hydrodynamic conditions experienced by fish passing through hydroelectric plants.<sup>9</sup> Contemporary lateral line sensing research focuses on the development and testing of devices capable of determining the hydromechanical properties of near-laminar flows. Most investigations have therefore focused on the recreation of the stimulus response of biological sensing modalities under laboratory conditions. Various types of LLPs have been developed and tested; thermal hotwire anemometry,<sup>10</sup> illuminated silicon bars embedded in machined polyvinyl chloride canals,<sup>11</sup> parylene coated micro-mechanical cantilevers,<sup>12</sup> a surficial array of piezoresistive pressure sensors,<sup>13</sup> and most recently, a multimodal platform using ionic polymer metal composites in conjunction with embedded pressure sensors.<sup>14</sup> Current work by others using a fish-shaped platform outfitted with lateral piezoelectric arrays has shown the utility of using fish-shaped probes, providing the first physical evidence correlating LLP measurements with the physiological distribution of a real fish's sensory network.<sup>15</sup>

The focus of the LLP introduced in this work is the acquisition and processing of laboratory and field data under

<sup>a)</sup>Author to whom correspondence should be addressed. Electronic mail: tuhtan@sjeweb.de.

the spectrum of natural flow conditions found in creeks, rivers, and fish passage structures. Our main research objective is to design a device, which can be used for comparative studies using both laboratory and field data. In this work, it is shown how the LLP can accurately sample laboratory flows while remaining robust enough for the wide spectrum of flow conditions found in a vertical slot fishway (VSF). Specifically, we (1) provide a calibration workflow for laboratory investigations of the pressure field surrounding the LLP body, (2) show how LLP pressure signals can be used to estimate flow time averaged velocity magnitude independent of device calibration, and (3) recreate a flow map comparable with computational fluid dynamics (CFD) models using large eddy simulation (LES), Reynolds-averaged Navier Stokes (RANS), and acoustic Doppler velocimeter (ADV) based flow measurements obtained in a scale vertical slot fishway model. The LLP is thus capable of covering at minimum, the standard tasks of conventional measurement devices. In addition, it delivers high-frequency estimates of the pressure field fluctuations, which will allow for the development of new metrics for both laboratory and field investigations of fish and other aquatic organisms.

## II. DESIGN

The LLP used in this work consists of 16 piezoresistive pressure sensors (SM5420C-030-A-P-S, Silicon Microstructures) mounted within an ABS plastic fish-shaped body. A stainless steel tube inserted through the top of the body provides a watertight data and power cable connection and is also used to fix the location of the probe during experiments (Figure 1). The geometry is based on a 3D scan of an adult rainbow trout (*Oncorhynchus mykiss*) with a body length of 45 cm (Figure 1). The pressure sensors with a span of 0–207 kPa are supplied with 4.096 V providing a full range sensitivity of 81.92 mV. The signals undergo a first stage amplification of factor 20.84 with instrumentation amplifiers (AD8421ARMZ, Analog Devices) and a second stage amplification of factor 16.43 with operational

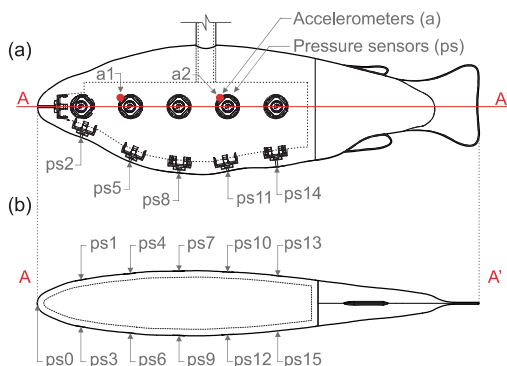


FIG. 1. Schematic of the fish-shaped lateral line probe. (a) Side view showing bottom and 5 of the 10 lateral pressure sensors and inline accelerometers. (b) Top view showing all 16 pressure sensor locations. In this work, only the nose sensor ps0 in conjunction with the 10 lateral sensors was used.

amplifiers (AD8656ARMZ, Analog Devices) resulting in a total amplification factor of 342.46. Due to the two stage amplification, it is possible to amplify a 396 nV/Pa signal to 136  $\mu$ V/Pa signal. The first and second stage amplified signals are then digitized with a 16-bit analog to digital converter (AD7682BSPZ, Analog Devices) with the reference voltage 4.096 V, providing a resolution of 7.6 Pa/LSB for the first stage amplified signals and 0.46 Pa/LSB for the second stage amplified pressure signals.

## III. EXPERIMENTS

Three distinct sets of experiments were performed using the LLP.<sup>16–18</sup> In this work, a review and comparison of the results are presented. The first set of laboratory experiments were carried out in a closed flow tunnel (experiment 1). The second set of experiments were carried out in an open channel flume (experiment 2). After establishing velocity estimation workflows, flow maps were generated for a scale fish pass model (experiment 3), providing a spatial visualization of the current velocity relative to a given fish pass geometry and mass flow rate.

### A. Experiment 1: Closed flow tunnel

Experiment 1 was carried out in a flow tunnel with a fixed top in order to minimize the variation of the hydrostatic pressure across the probe body. The closed flume had a working section of 0.5 m in width and height, and a length of 1.5 m (Figure 2). A calibrated digital motor controller was used to set the time-averaged flow velocity in the working section from 0.05 to 0.5 m/s in 0.05 increments, calibrated to an accuracy of 0.04 m/s.<sup>19</sup> Homogeneous turbulence (random motions of the fluid are independent of their location)<sup>20</sup> is induced by means of two collimators with a 9 mm grid spacing placed immediately upstream of the working section. The LLP was fixed at the center of the working section, facing the flow. A total of three replicates (R1, R2, R3) were recorded at 250 Hz with a sampling duration of 30 s each; with 30 s of

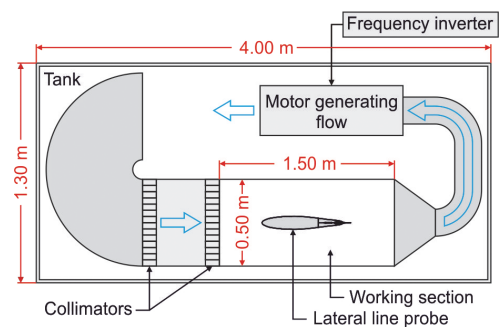


FIG. 2. Experimental setup in the closed flow tunnel (experiment 1), view from above. The LLP was placed in the center of the flow tunnel working section and subjected to a uniform freestream velocity field (flow is from left to right). Homogeneous turbulence in the upstream flow is produced by passing the water through two collimators placed directly upstream of the working section.

run-up time between measurements to ensure the velocity had stabilized.

## B. Experiment 2: Open channel flume

The second series of LLP measurements (experiment 2) were taken in an open channel flume of 1 m width, 0.6 m height, and 27 m length. Ten consecutive replicates of each measurement were taken at 25%, 40%, and 60% of the flow depth, fixed for all flow rates at 35 cm. Ensemble averaging was then performed for all velocity measurements. Each LLP measurement was taken at 250 Hz with a sampling duration of 60 s, and the velocity was simultaneously recorded using a 1 Hz ADV (Flowtracker, Sontek) directly upstream of the LLP (Figure 3). The slopes of the flume and discharge were varied in order to obtain a range of current velocities (taken as the time-averaged velocity at 40% of depth) from 0.1 to 0.5 m/s in 0.1 m/s increments. In contrast with the closed flow tunnel, the open channel flows experienced by the LLP are subject to non-uniform turbulence as well as larger temporal and spatial pressure fluctuations due to the free water surface. The open channel conditions are therefore more representative of natural hydrodynamic flows, and a comparison of both laboratory settings for the same time-averaged velocities is thus of interest when considering future field applications.

## C. Experiment 3: Vertical slot fishway model

In order to investigate the range of hydraulic conditions, which more closely match those found in the field, LLP measurements (250 Hz for 30 s) were carried out in a 1:1.6 scale model of the VSF installed in Koblenz, Germany. The model consists of three basins with a fixed bed at constant elevation and adjustable discharge and upstream and downstream water surface elevations.<sup>16</sup> Two flow scenarios were investigated:  $Q_1 = 0.130 \text{ m}^3/\text{s}$  with a mean water depth  $h_0 = 0.52 \text{ m}$  and  $Q_2 = 0.170 \text{ m}^3/\text{s}$ ,  $h_0 = 0.56 \text{ m}$ . For both flow scenarios, the LLP was mounted on Cartesian robot at three reference depths:  $0.25h_0$ ,  $0.4h_0$ , and  $0.6h_0$ . At each depth,



FIG. 3. Setup in the open channel flume (experiment 2), flow direction is given by the arrow. The view is from above facing downstream where the LLP is placed in the center of the flume and adjusted only in the vertical direction. The ADV is positioned such that the sampling volume is located 10 cm in front of the LLP nose sensor,  $P_0$  (Figure 1).

24 measurement locations were chosen, providing a planar estimation of the time-averaged velocity magnitude. Point velocity measurements at  $0.25h_0$  and  $0.4h_0$  were taken using a laser Doppler anemometer (LDA) (2D FlowExplorer System, Dantec Dynamics) at 1 Hz for 60 s, and at  $0.6h_0$  with an ADV (Vectrino, Nortek) at 25 Hz for 60 s.

## IV. CALIBRATION

The current velocity ( $U$ ) is the most commonly used hydraulic parameter in studies of fish swimming<sup>21</sup> and behavior<sup>22</sup> and is defined as the magnitude of the three Cartesian velocity components ( $u_x$ ,  $u_y$ , and  $u_z$ )

$$U = \sqrt{u_x^2 + u_y^2 + u_z^2}. \quad (1)$$

Estimation of the current velocity is performed using the Bernoulli approach, which invokes the conservation of energy to relate the pressure difference between a stagnation point (here taken as the nose sensor  $P_0$ ) and the free stream static pressure. Using an LLP for calibrated current velocity estimation requires the nose and at least one of the 10 lateral sensors, ( $P_L$ )<sup>23,24</sup>

$$\frac{\rho \cdot U^2}{2} = (P_0 - P_L) = \Delta P_{0,1}, \quad (2)$$

where  $\rho$  is the density of water. As the lateral sensors are non-ideal and experience both static and dynamic pressure (Figure 4), it is necessary to apply a semi-empirical correction factor ( $\beta_{U,1}$ ) to the velocity estimation<sup>25</sup>

$$U = \sqrt{\frac{2 \cdot \beta_{U,1} \cdot \Delta P_{0,1}}{\rho}}. \quad (3)$$

The value of the correction factor depends on the probe geometry and choice of pressure sensors. In general, LLP calibration involves three factors: temperature-dependent power consumption, relative pressure, and atmospheric pressure.

The temperature ( $T$ ) is linearly related with the pressure sensor readings ( $P$ ) and their individual current consumption ( $CC$ ), thus, taking into account the  $CC$  (measured by the shunt resistors), it is possible to translate the readings of all pressure sensors to a current consumption level at reference temperature, here taken as  $CC_{T=20^\circ\text{C}}$ . This leaves the following expression for the linear calibration relation between  $P$  and  $CC$ :

$$P_{T=20^\circ\text{C},N} = P_{T,N} + (CC_{T,N} - CC_{T=20^\circ\text{C},N}) \cdot \beta_{T,N}, \quad (4)$$

where  $P_{T=20^\circ\text{C},N}$  is the recorded pressure of sensor  $N$  translated to a reference temperature of  $20^\circ\text{C}$ ,  $P_{T,N}$  is the recorded pressure of sensor  $N$  at the temperature for that measurement,  $CC_{T,N}$  is the recorded current consumption of sensor  $N$ ,  $CC_{T=20^\circ\text{C},N}$  is the current consumption of sensor  $N$  at the reference temperature of  $20^\circ\text{C}$ , and  $\beta_{T,N}$  is the slope of the linear regression relation between  $CC$  and  $T$ . The relation for each sensor was obtained by submerging the LLP into a 54 l tank with fixed vertical position to ensure constant hydrostatic pressure, starting at  $0^\circ\text{C}$  and increasing up to a maximum of  $30^\circ\text{C}$  using two immersion heaters (Rommelsbacher RT 350).

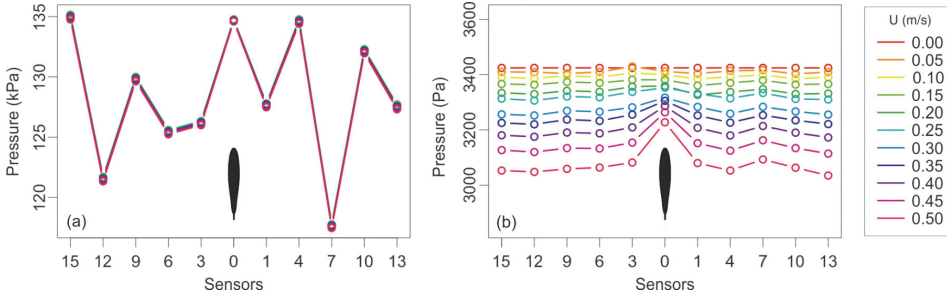


FIG. 4. Comparison of time-averaged uncalibrated and calibrated sensor readings for 0-0.5 m/s flows in the closed test tank. (a) Uncalibrated pressure readings for the nose (0) and lateral sensors (1-15). (b) Calibrated readings showing the decrease in pressure magnitude with increasing pressure gradient around the body as a function of increasing current velocity,  $U$  (m/s).

After temperature calibration, pressure readings in each sensor will still have relative values, i.e., the same hydrodynamic stimulus will produce values with different offsets. Thus, each sensor has to be calibrated to produce the same hydrodynamic signal response. To achieve this, the LLP was submerged progressively in a glass walled tank (from 0 to 0.7 m in 0.05 m increments), while the hydrostatic pressure response was monitored for each vertical position in the water column. The water column above the probe was translated to Pa, and the relation between the hydrostatic and measured pressure was adjusted by means of a linear fit for each sensor individually

$$P_N = \beta_{0,R,N} + P_{T=20^\circ C, N} \cdot \beta_{1,R,N}, \quad (5)$$

where  $P_N$  is the fitted output for sensor  $N$  and  $\beta_{0,R,N}$  and  $\beta_{1,R,N}$  are the empirical parameters of the relation.

## V. METHODOLOGY

In order to make use of the LLP under field conditions, it is necessary to develop velocity estimation workflows independent of calibration. Here, we compare two workflows developed for uncalibrated velocity estimation using the fish-shaped LLP.<sup>17,18</sup> In this section, we provide a brief overview of each workflow (Figure 5) and conclude with a comparison and discussion of the two methods for experiment 1 in the closed tank and experiment 2 in the open flume (Figure 6).

### A. Kernel ridge regression

The first method for estimating the time averaged velocity magnitude uses median normalized pressure sensor readings and kernel ridge regression.<sup>18</sup> In a first step, the LLP results

are expressed as the measurement vector  $s(t)$  for  $N$  sensors

$$s(t) = \begin{pmatrix} s_0(t) \\ s_1(t) \\ \vdots \\ s_N(t) \end{pmatrix}. \quad (6)$$

From which samples are selected to form the sample matrix,  $T$  for further analysis and processing

$$\begin{aligned} S_{t_0} &= s(t_0 + 0) s(t_0 + 1) \cdots s(t_0 + T - 1) \\ &= \begin{pmatrix} s_0(t_0 + 0) & s_0(t_0 + 1) & \cdots & s_0(t_0 + T - 1) \\ s_1(t_0 + 0) & s_1(t_0 + 1) & \cdots & s_1(t_0 + T - 1) \\ \vdots & \vdots & \ddots & \vdots \\ s_D(t_0 + 0) & s_D(t_0 + 1) & \cdots & s_D(t_0 + T - 1) \end{pmatrix}. \end{aligned} \quad (7)$$

It is worth noting that the sample matrix Eq. (6) represents the raw measurement data available for analysis.

In the next step, we evaluate the second order statistic for each sensor signal

$$\mathbf{x} = \frac{1}{T-1} \sum_{i=0}^{T-1} (s(i) - \mu_x)^2, \quad (8)$$

where  $\mu_x$  is the median of a single sensor time series.

This workflow makes use of kernel ridge regression, which we have chosen instead of classical ordinary least squares (OLS), which minimizes the squared losses. We have done so due to the limited number of training examples which using OLS can cause a large variance of the linear regression weights  $w$ , leading to overfitting between the covariates  $x_i$  and the response variable  $y_i$  (velocity magnitude). Instead of minimizing the squared errors, ridge regression minimizes

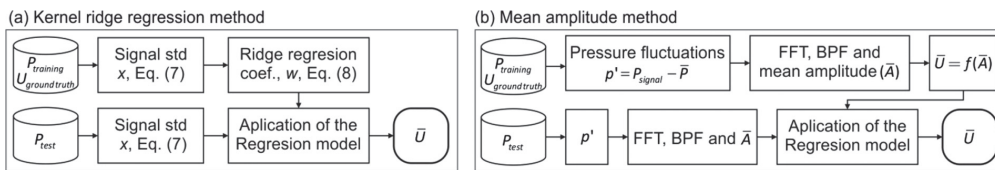


FIG. 5. Workflows used for velocity estimation. (a) Kernel ridge regression (b) mean amplitude estimation.

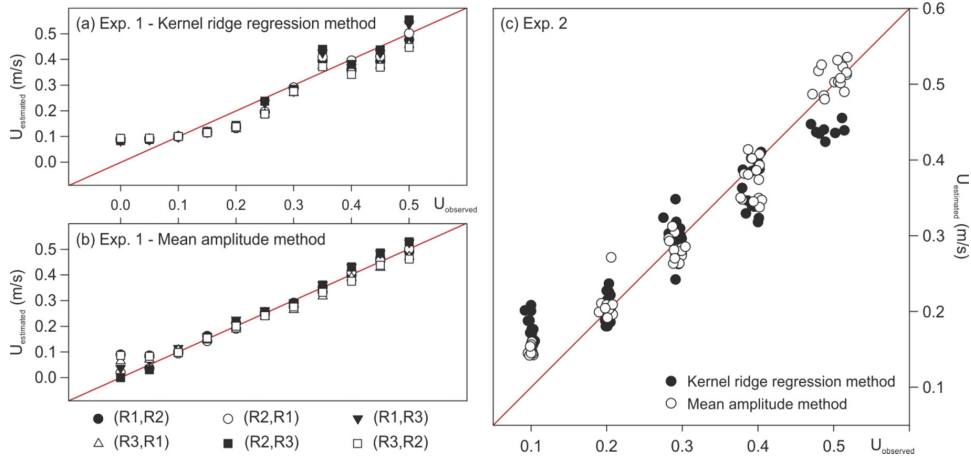


FIG. 6. Results of current velocity estimation from the ((a) and (b)) closed flow tunnel (experiment 1) and (c) the open channel flume (experiment 2) using both signal processing methods.

the cost

$$J(w) = \sum (y_i - w^T x_i)^2 + \lambda \|w\|, \quad (9)$$

where  $\lambda$  is a positive regularization parameter, which reduces the estimate  $w$  variance, at the expense of increasing the training errors (trade-off between the bias and the variance). Cross-validation can be used to determine the optimal regularization parameter, which minimizes cross-validation errors. Kernel ridge regression makes use of the kernel trick, replacing the original features  $x$  with the kernel feature transformation  $x_i \rightarrow \Phi(x_i)$ .<sup>26</sup> In this work, we used second-order polynomial kernels  $k(x_i, x_j) = (x_i^T x_j + 1)^d$  and three-fold cross-validation. In the flow tunnel experiments, a total of three replicate experiments were performed (R1, R2, R3), and the average error of the velocity estimate was determined using the six possible combinations of training and testing (Figure 7). In the open channel flume experiments, ten replicate experiments were carried out, where five were used for training and the remaining five for testing. Previous work in a closed channel flume using this workflow has shown that the LLP is capable of current velocity estimation under extreme angular deviations ( $\pm 90^\circ$ ) with 4-8 cm/s error and can provide joint estimates

of the angular deviation and velocity for free stream currents  $> 45$  cm/s.<sup>18</sup>

## B. Mean amplitude estimation

The second method used in this work uses a bandpass filter in conjunction with the frequency domain mean amplitude to create a regression fit for velocity estimation.<sup>17</sup> This method utilizes a two-stage signal processing workflow. In the first stage, Reynolds decomposition is performed separating the pressure signal into the time average,  $\bar{P}$ , which includes the atmospheric pressure, hydrostatic pressure, and pressure changes due to near-field fluctuations about the time average,  $p'$ ,

$$P = \bar{P} + p'. \quad (10)$$

In the second stage, the discrete Fourier transform (DFT) is applied to convert the time domain fluctuation signal  $p'(t)$  consisting of  $M$  points of the spectrum from  $T$  discrete points in the signal. The result is the corresponding frequency domain representation,  $X(m \cdot v)$  of the time domain pressure fluctuation signal,  $p'(t)$

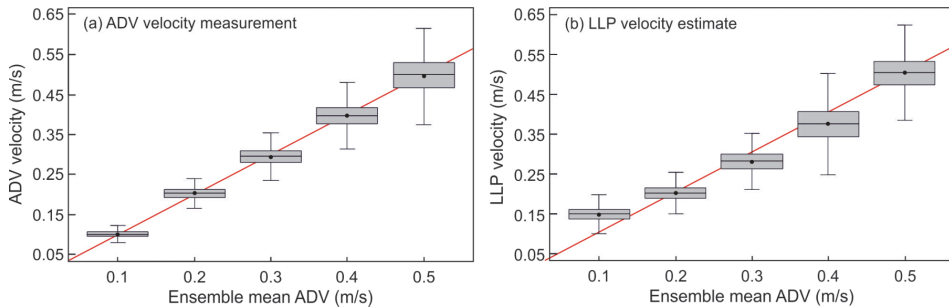


FIG. 7. Comparison of the (a) ADV measurements and (b) LLP velocity estimates using the mean amplitude method. The sample sizes for the ADV measurements (0.1, 0.2, 0.3, 0.4, 0.5) m/s were (2100, 2100, 2160, 1560, 1320) and 56 251 for each LLP velocity estimate.

$$X(m \cdot v) = \int_{t=0}^{T-1} p'(t) e^{-j2\pi \frac{tm}{M}} dt, \quad (11)$$

where  $m \in [0, M)$ ,  $t \in [0, T)$  and  $v = F_s/M$  is the frequency resolution and  $F_s$  is the sampling frequency. After conversion to the frequency domain, a bandpass filter is applied. Regression using OLS is then used to obtain the best fit between the mean amplitude for each measurement interval against the ground truth velocity magnitude (Figure 4).

There are two parameters, which must be determined in order to apply this workflow, the sample length of the fluctuation signal, and the filter cutoff frequencies. One drawback of this approach is that the choice of both parameters depends not only on the local flow conditions but is also dependent on the body shape. In this work, the optimized cutoff frequencies were at 0 and 30 Hz for experiment 1 and 0 and 4 Hz for experiments 2 and 3, respectively. Filtering can be omitted from the workflow; however, the performance has been found to increase with increasing turbulence when filtering is applied.<sup>17</sup> The sample length for all experiments was 30 s, training and testing for experiment 1 was performed using combinations (R1 training, R2 testing, etc.) of three replicates to evaluate differences in estimation performance based on the individual experiments. Experiment 2 used half of the data for training and the remaining half for testing (Figure 6).

An additional step can also be included to both time-averaged velocity estimation workflows, allowing for a resampling of the velocity estimates using Eq. (3). Resampling data can then be compared to PIV or other high frequency velocity measurement data in order to develop LLP signal processing workflows for turbulence metrics TI and TKE.

## VI. RESULTS

### A. Velocity estimation workflows

A comparison of the kernel ridge regression and mean amplitude methods between the closed tunnel (experiment 1) shows that the mean amplitude method provided more consistent results across the range of current velocities tested (Figures 6(a) and 6(b)). Specifically, the use of a low-pass filter and reliance on the mean amplitude for estimating the current velocity simplifies the LLP signal processing. It should be noted that the mean amplitude method cannot be used in cases where the joint estimation of the angular deviation and current velocity is of interest. Both methods systematically overestimated velocities  $<10$  cm/s. Results for the open channel (experiment 2) show similar results when compared to the closed flow tunnel, as both methods consistently overestimate the low velocities as well (Figure 6(c)), indicating that the device as it is currently configured may not be capable of current velocity estimation in the lower range.

As the ADV is the most commonly applied field measurement device for point measurements of turbulent flows in rivers, we were also interested not only in the overall fit of the LLP to ADV measurements but also their distributions. A comparison of the LLP mean amplitude method with ADV ensemble averages (Figure 7) shows that for the range of flow

velocities investigated the distributions are very similar, with a general increase in the interquartile range with increasing current velocity and consistent overestimation of the lowest flow velocity. In general, it was found that the LLP can be a suitable replacement for the ADV when the current velocity is expected to be  $>10$  cm/s.

### B. Flow map analysis

After establishing the calibration coefficients and error estimates for open channel flow measurements, the LLP was tested in a more complex hydraulic geometry that of a 1:1.6 scale vertical slot fishway (experiment 3). The objective was to investigate a larger spectrum of local hydraulic conditions under fully turbulent flow within a laboratory environment. Due to their international application, VSFs have been the subject of hydraulic research for over 70 years,<sup>27,28</sup> and the general flow pattern within individual basins is well-known<sup>29</sup> and can be assessed based on known swimming capabilities of fish using CFD models or interpolated flow maps from direct point measurements.<sup>30</sup> In this experiment, we compared the spatial distributions of the current velocity from LES and RANS models to direct measurement from an ADV and the LLP estimates (Figure 8). It can be seen that the predicted flow map resulting from the LLP estimates more closely match the ADV measurements than either of the CFD models. In general, the LLP was found to be in good agreement with both measured and modelled results, where the LLP velocity estimates were found to be systematically higher in the central jet region.

In contrast to the open and closed channel experiments, the effects of noise caused by body self-motion are expected to be greater in the VSF due to the wider range of flow conditions and the need to reposition the sensor body for each measurement. In order to assess the potential impact of body self-motion on the velocity estimation, the signal to noise ratio of the two inline accelerometers was estimated for each measurement (Figure 9) by using the anterior accelerometer a1 as the root mean square (RMS) of the input signal,  $RMS_{a1}$  and the noise was estimated by the lateral body motion as the difference between accelerometers,  $RMS_{a1-a2}$

$$SNR = 10 \log_{10} \left( \frac{RMS_{a1}}{RMS_{a1-a2}} \right). \quad (12)$$

A comparison of the noise map with the observed errors between ADV and LLP indicates that the body self-motion is likely to increase the current velocity estimates for regions of higher flow velocity, possibly caused by the overall higher pressure magnitudes experienced by the transducers when the body experiences lateral oscillation. Conversely, the velocity is underestimated in the top and bottom recirculation regions close to the walls where the pressure magnitudes experienced by the LLP are likely to decrease due to the local flow acceleration around the body. A correction model based on the local gradients of the velocity field experienced by the LLP may aid in further improvement of the LLP current velocity estimates for measurements in geometrically confined regions such as in a VSF.

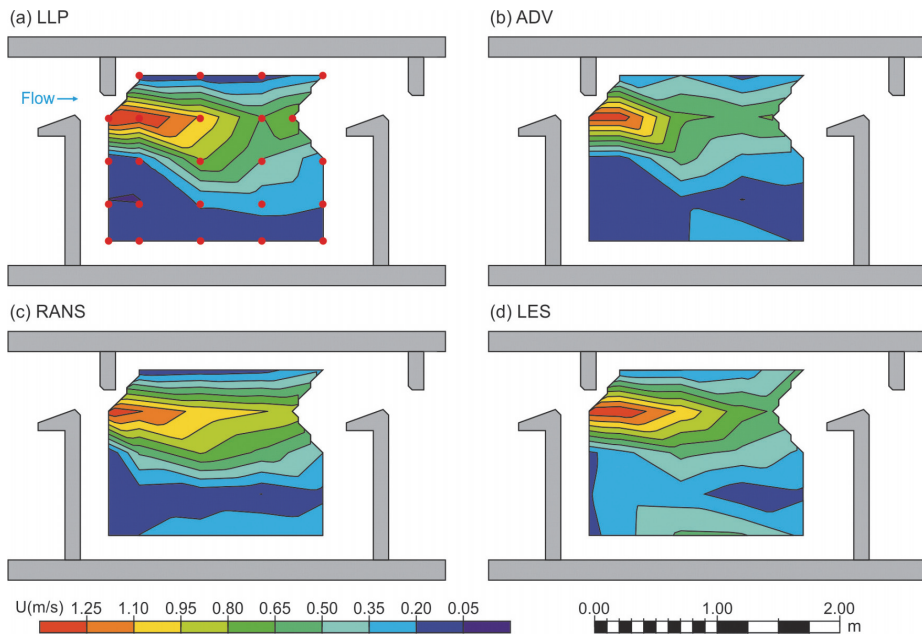


FIG. 8. Flow map results for LLP, ADV measurements, and CFD models, measurement locations are shown as red dots (experiment 3). (a) LLP flow map, (b) ADV measurements, (c) RANS CFD model, (d) LES (30 s averaged). The largest differences occur between the RANS and LES flow maps, primarily due to the difference in the time-averaging of the results. Isocontour values on all maps were created comparing identical sampling locations to the velocity probe measurements taken at 60% of depth (m/s).

**VII. DISCUSSION**

In this work, we presented the design, calibration, and implementation of a fish-shaped LLP for three experiments. We demonstrated how the device may be used for current velocity estimation under laboratory conditions both in a closed tunnel and in an open channel. It was found that the device had an expected accuracy of 0.03-0.04 m/s under ideal conditions with homogeneous turbulence in a closed tunnel (experiment 1) and was able to maintain similar performance of 0.02–0.04 m/s under the more challenging conditions created by the open channel experiments (experiment 2). Furthermore, it was shown that the spatial flow map generated by the LLP was in general agreement with maps produced

by ADV measurements and both RANS and LES CFD simulations.

A notable deviation of the mean accuracy across the 0-0.5 m/s span of investigated velocities was found for the lowest velocities 0.1 and 0.2 m/s (Figure 6). Here, the LLP provided a systematic overestimation of the bulk time-averaged velocity considering both methods and for the closed flume and open channel experiments. The cause of the deviation is possibly the chosen transducer sensitivity, where both velocity estimation methods rely on the deviations from a baseline pressure signal. In the case of low velocities, the sensitivity of the LLP may therefore not be high enough to register significant differences in the deviations for bulk flow velocities lower than 0.2 m/s. Further investigations will

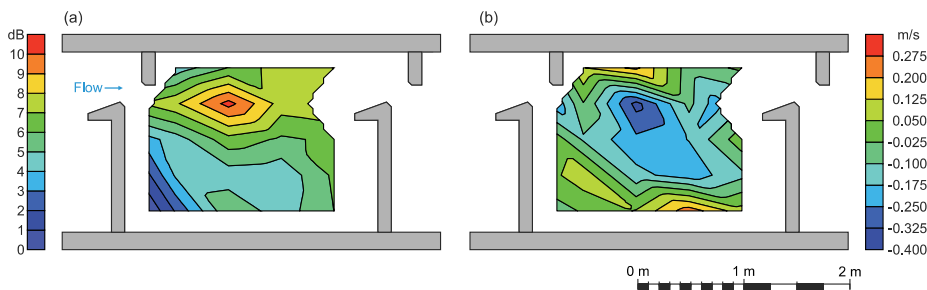


FIG. 9. Comparison of noise estimate due to body self-motion and the observed error between the ADV and LLP. (a) Noise map showing the spatial distribution of the accelerometer-based estimates (dB), (b) error distribution taken as the difference between ADV and LLP (m/s).

be carried out with increased amplification of the pressure transducers in order to test this hypothesis.

In general, a comparison of the open channel ADV measurements and mean amplitude method revealed similar statistics, namely, that lower velocities can be obtained with a higher precision (Figure 7). This is not surprising considering the nature of turbulent flows, where an increase in the variance of the bulk flow velocity is often directly related to increasing levels of turbulent fluctuations.

The comparison of the VSF flow map between ADV measurements as well as the RANS and LES CFD models shows that the LLP is capable of reproducing spatial estimates of flows similar to those occurring under field conditions. Due to the physical size of the LLP body, one limitation of the device is the resulting spatial resolution of measurements. However, the simultaneous measurement of the flow field with the larger LLP body does open new avenues of investigation. Future research will investigate the two point correlations between pressure readings and their possible relationship to the characteristic time and length scales of the largest energy containing eddies. Thus, it may be possible to exploit the geometry of the LLP in order to obtain flow property metrics which have thus far only been possible in detailed laboratory investigations.

## VIII. CONCLUSION

It was found that for closed tunnel and open channel experiments, the mean amplitude velocity estimation workflow provided the most consistent results. Both the kernel ridge regression and mean amplitude workflows consistently overestimated low velocities (<10 cm/s), indicating that transducers with higher sensitivity are likely needed for lower range measurements to deliver results comparable with an ADV. The spatial distribution of the noise level caused by body self-motion using the difference between two inline accelerometers was found to correspond with the observed measurement error. Future work to improve the performance of the LLP for flow measurement should focus on instantaneous velocity estimation in order to provide estimates of turbulence, improving device sensitivity for low flow conditions, and investigating adaptive noise cancellation for real-time correction of current velocity estimates in geometrically confined regions.

## ACKNOWLEDGMENTS

The research leading to these results has received funding from BONUS, the joint Baltic Sea research and development programme (Art 185), funded jointly from the European Union's Seventh Programme for research, technological development and demonstration and from the

Academy of Finland (under the Grant No. 280715), the German Federal Ministry for Education and Research (BMBF FKZ:03F0687A), and the Estonian Environmental Investment Centre (KIK P.7254 C.3255). The work has also been partly financed by the EU FP7 project ROBOCADEMY (No. 608096).

- <sup>1</sup>R. W. J. Lacey, V. S. Neary, J. C. Liao, E. C. Enders, and H. M. Tritico, *River Res. Appl.* **28**, 429 (2012).
- <sup>2</sup>G. Wu, Y. Yang, and L. Zeng, *Rev. Sci. Instrum.* **77**, 114302 (2006).
- <sup>3</sup>Z. Deng, G. R. Guensch, C. A. McKinstry, R. P. Mueller, D. D. Dauble, and M. C. Richmond, *Can. J. Fish. Aquat. Sci.* **62**, 1513 (2005).
- <sup>4</sup>Z. Deng, R. P. Mueller, M. C. Richmond, and G. E. Johnson, *North Am. J. Fish. Manage.* **30**, 623 (2010).
- <sup>5</sup>S. Dijkgraaf, *Biol. Rev.* **38**, 51 (1963).
- <sup>6</sup>E. J. Denton and J. A. B. Gray, in *Sensory Biology of Aquatic Animals*, edited by J. Atema, R. R. Fay, A. N. Popper, and W. N. Tavolga (Springer, New York, 1988), pp. 595–617.
- <sup>7</sup>J. Evans, F. Ahmad, and J. M. Nestler, U.S. patent US5675555 A (7 October 1997).
- <sup>8</sup>J. M. Nestler, J. L. Pickens, J. Evans, and R. W. Haskins, U.S. patent US5517465 A (14 May 1996).
- <sup>9</sup>Z. D. Deng, J. Lu, M. J. Myjak, J. J. Martinez, C. Tian, S. J. Morris, T. J. Carlson, D. Zhou, and H. Hou, *Rev. Sci. Instrum.* **85**, 115001 (2014).
- <sup>10</sup>Y. Yang, J. Chen, J. Engel, S. Pandya, N. Chen, C. Tucker, S. Coombs, D. L. Jones, and C. Liu, *Proc. Natl. Acad. Sci. U. S. A.* **103**, 18891 (2006).
- <sup>11</sup>A. Klein and H. Bleckmann, *Beilstein J. Nanotechnol.* **2**, 276 (2011).
- <sup>12</sup>A. Qualtieri, F. Rizzi, G. Epifani, A. Ernits, M. Kruusmaa, and M. De Vittorio, *Microelectron. Eng.* **98**, 516 (2012).
- <sup>13</sup>R. Venturelli, O. Akanyeti, F. Visentin, J. Ježov, L. D. Chambers, G. Toming, J. Brown, M. Kruusmaa, W. M. Megill, and P. Fiorini, *Bioinspiration Biomimetics* **7**, 036004 (2012).
- <sup>14</sup>L. DeVries, F. D. Lagor, H. Lei, X. Tan, and D. A. Paley, *Bioinspiration Biomimetics* **10**, 025002 (2015).
- <sup>15</sup>L. Ristroph, J. C. Liao, and J. Zhang, *Phys. Rev. Lett.* **114**, 018102 (2015).
- <sup>16</sup>M. Musall, P. Oberle, R. Carbonell-Baeza, F. Nestmann, J. F. Francisco Fuentes-Perez, and J. A. Tuhtan, *Wasserwirtschaft* **7/8**, 67 (2015).
- <sup>17</sup>J. F. Fuentes-Perez, J. A. Tuhtan, R. Carbonell-Baeza, M. Musall, G. Toming, N. Muhammed, and M. Kruusmaa, *Ecol. Eng.* **85**, 296 (2015).
- <sup>18</sup>N. Strokina, J.-K. Kämäräinen, J. A. Tuhtan, J. F. Fuentes-Perez, and M. Kruusmaa, *IEEE Trans. Instrum. Meas.* **65**, 601 (2016).
- <sup>19</sup>G. Toming, T. Salumäe, A. Ristolainen, F. Visentin, O. Akanyeti, and M. Kruusmaa, in *2012 IEEE International Conference on Robotics and Biomimetics (ROBIO)* (IEEE, 2012), pp. 532–537.
- <sup>20</sup>G. K. Batchelor, *The Theory of Homogeneous Turbulence, Reprint* (Cambridge University Press, Cambridge, New York, 1982).
- <sup>21</sup>J. J. Videler, *Fish Swimming* (Springer Science & Business Media, 2012).
- <sup>22</sup>B. Adam and B. Lehmann, *Ethohydraulik* (Springer, Berlin, Heidelberg, 2011).
- <sup>23</sup>A. B. Dubois, G. A. Cavagna, and R. S. Fox, *J. Exp. Biol.* **60**, 581 (1974).
- <sup>24</sup>M. Kruusmaa, G. Toming, T. Salumäe, J. Jezov, and A. Ernits, in *2011 IEEE International Conference on Robotics and Biomimetics (ICRA)* (IEEE, 2011), pp. 1791–1796.
- <sup>25</sup>T. Salumäe and M. Kruusmaa, *Proc. R. Soc. London, Ser. A* **469**, 20120671 (2013).
- <sup>26</sup>C. Saunders, A. Gammernan, and V. Vovk, in *Proceedings of Fifteenth International Conference on Machine Learning* (Morgan Kaufmann Publishers, Inc., San Francisco, CA, 1998), pp. 515–521.
- <sup>27</sup>N. Rajaratnam, G. V. der Vinne, and C. Katopodis, *J. Hydraul. Eng.* **112**, 909 (1986).
- <sup>28</sup>C. H. Clay, *Design of Fishways and Other Fish Facilities* (CRC Press, 1994).
- <sup>29</sup>J. F. Fuentes-Perez, F. J. Sanz-Ronda, A. Martinez de Azagra Paredes, and A. Garcia-Vega, *J. Hydraul. Eng.* **140**, 06014016 (2014).
- <sup>30</sup>L. A. Khan, *North Am. J. Fish. Manage.* **26**, 255 (2006).



# CURRICULUM VITAE

## Personal data

Name: Gert Toming  
Date of birth: 15.09.1984  
Place of birth: Vändra, Estonia  
Citizenship: Estonian

## Contact data

Address: Tammepõllu tee 23-8, 74001 Haabneeme, Harjumaa, Estonia  
Phone: +372 5349 4320  
E-mail: gert.toming@gmail.com

## Education

2010 – 2017	Tallinn University of Technology	PhD
2007 – 2010	University of Tartu	MSc
2004 – 2007	University of Tartu	BSc
2001 – 2004	Pärnu Koidula Gymnasium	Highschool

## Language competence

Estonian	Native
English	Fluent
German	Basic
Russian	Basic

## Professional employment

2015 - ...	Tallinn University of Technology	Engineer
2012 – 2015	Tallinn University of Technology	Junior researcher
2012 – 2012	Tallinn University of Technology	Engineer
2010 – 2012	Tallinn University of Technology	Researcher
2010 – 2010	Tallinn University of Technology	Engineer
2007 – 2008	Trinamic Motion Control GmbH	Engineer
2006 – 2007	PT Mikro AS	Technician

# ELULOOKIRJELDUS

## Isikuandmed

Nimi: Gert Toming  
Sünniaeg: 15.09.1984  
Sünnikoht: Vändra, Eesti  
Kodakondsus: Eesti

## Kontaktandmed

Aadress: Tammepõllu tee 23-8, 74001 Haabneeme, Harjumaa  
Telefon: +372 5349 4320  
E-mail: gert.toming@gmail.com

## Hariduskäik

2010 – 2017	Tallinna Tehnikaülikool	PhD
2007 – 2010	Tartu Ülikool	MSc
2004 – 2007	Tartu Ülikool	BSc
2001 – 2004	Pärnu Koidula Gümnaasium	Keskharidus

## Keelteoskus

Eesti keel	Emakeel
Inglise keel	Kõrgtase
Saksa keel	algtase
Vene keel	algtase

## Teenistuskäik

2015 - ...	Tallinna Tehnikaülikool	Insener
2012 – 2015	Tallinna Tehnikaülikool	Nooremteadur
2012 – 2012	Tallinna Tehnikaülikool	Insener
2010 – 2012	Tallinna Tehnikaülikool	Teadur
2010 – 2010	Tallinna Tehnikaülikool	Insener
2007 – 2008	Trinamic Motion Control GmbH	Insener
2006 – 2007	PT Mikro AS	Tehnik

**DISSERTATIONS DEFENDED AT  
TALLINN UNIVERSITY OF TECHNOLOGY ON  
INFORMATICS AND SYSTEM ENGINEERING**

1. **Lea Elmik**. Informational Modelling of a Communication Office. 1992.
2. **Kalle Tammemäe**. Control Intensive Digital System Synthesis. 1997.
3. **Eerik Lossmann**. Complex Signal Classification Algorithms, Based on the Third-Order Statistical Models. 1999.
4. **Kaido Kikkas**. Using the Internet in Rehabilitation of People with Mobility Impairments – Case Studies and Views from Estonia. 1999.
5. **Nazmun Nahar**. Global Electronic Commerce Process: Business-to-Business. 1999.
6. **Jevgeni Riipulk**. Microwave Radiometry for Medical Applications. 2000.
7. **Alar Kuusik**. Compact Smart Home Systems: Design and Verification of Cost Effective Hardware Solutions. 2001.
8. **Jaan Raik**. Hierarchical Test Generation for Digital Circuits Represented by Decision Diagrams. 2001.
9. **Andri Riid**. Transparent Fuzzy Systems: Model and Control. 2002.
10. **Marina Briik**. Investigation and Development of Test Generation Methods for Control Part of Digital Systems. 2002.
11. **Raul Land**. Synchronous Approximation and Processing of Sampled Data Signals. 2002.
12. **Ants Ronk**. An Extended Block-Adaptive Fourier Analyser for Analysis and Reproduction of Periodic Components of Band-Limited Discrete-Time Signals. 2002.
13. **Toivo Paavle**. System Level Modeling of the Phase Locked Loops: Behavioral Analysis and Parameterization. 2003.
14. **Irina Astrova**. On Integration of Object-Oriented Applications with Relational Databases. 2003.
15. **Kuldar Taveter**. A Multi-Perspective Methodology for Agent-Oriented Business Modelling and Simulation. 2004.
16. **Taivo Kangilaski**. Eesti Energia käiduhaldussüsteem. 2004.
17. **Artur Jutman**. Selected Issues of Modeling, Verification and Testing of Digital Systems. 2004.
18. **Ander Tenno**. Simulation and Estimation of Electro-Chemical Processes in Maintenance-Free Batteries with Fixed Electrolyte. 2004.

19. **Oleg Korolkov.** Formation of Diffusion Welded Al Contacts to Semiconductor Silicon. 2004.
20. **Risto Vaarandi.** Tools and Techniques for Event Log Analysis. 2005.
21. **Marko Koort.** Transmitter Power Control in Wireless Communication Systems. 2005.
22. **Raul Savimaa.** Modelling Emergent Behaviour of Organizations. Time-Aware, UML and Agent Based Approach. 2005.
23. **Raido Kurel.** Investigation of Electrical Characteristics of SiC Based Complementary JBS Structures. 2005.
24. **Rainer Taniloo.** Ökonoomsete negatiivse diferentsiaaltakistusega astmete ja elementide disainimine ja optimeerimine. 2005.
25. **Pauli Lallo.** Adaptive Secure Data Transmission Method for OSI Level I. 2005.
26. **Deniss Kumlander.** Some Practical Algorithms to Solve the Maximum Clique Problem. 2005.
27. **Tarmo Veskioja.** Stable Marriage Problem and College Admission. 2005.
28. **Elena Fomina.** Low Power Finite State Machine Synthesis. 2005.
29. **Eero Ivask.** Digital Test in WEB-Based Environment 2006.
30. **Виктор Войтович.** Разработка технологий выращивания из жидкой фазы эпитаксиальных структур арсенида галлия с высоковольтным р-п переходом и изготовления диодов на их основе. 2006.
31. **Tanel Alumäe.** Methods for Estonian Large Vocabulary Speech Recognition. 2006.
32. **Erki Eessaar.** Relational and Object-Relational Database Management Systems as Platforms for Managing Softwareengineering Artefacts. 2006.
33. **Rauno Gordon.** Modelling of Cardiac Dynamics and Intracardiac Bio-impedance. 2007.
34. **Madis Listak.** A Task-Oriented Design of a Biologically Inspired Underwater Robot. 2007.
35. **Elmet Orasson.** Hybrid Built-in Self-Test. Methods and Tools for Analysis and Optimization of BIST. 2007.
36. **Eduard Petlenkov.** Neural Networks Based Identification and Control of Nonlinear Systems: ANARX Model Based Approach. 2007.
37. **Toomas Kirt.** Concept Formation in Exploratory Data Analysis: Case Studies of Linguistic and Banking Data. 2007.
38. **Juhan-Peep Ernits.** Two State Space Reduction Techniques for Explicit State Model Checking. 2007.

39. **Innar Liiv**. Pattern Discovery Using Seriation and Matrix Reordering: A Unified View, Extensions and an Application to Inventory Management. 2008.
40. **Andrei Pokatilov**. Development of National Standard for Voltage Unit Based on Solid-State References. 2008.
41. **Karin Lindroos**. Mapping Social Structures by Formal Non-Linear Information Processing Methods: Case Studies of Estonian Islands Environments. 2008.
42. **Maksim Jenihhin**. Simulation-Based Hardware Verification with High-Level Decision Diagrams. 2008.
43. **Ando Saabas**. Logics for Low-Level Code and Proof-Preserving Program Transformations. 2008.
44. **Ilja Tšahhirov**. Security Protocols Analysis in the Computational Model – Dependency Flow Graphs-Based Approach. 2008.
45. **Toomas Ruuben**. Wideband Digital Beamforming in Sonar Systems. 2009.
46. **Sergei Devadze**. Fault Simulation of Digital Systems. 2009.
47. **Andrei Krivošei**. Model Based Method for Adaptive Decomposition of the Thoracic Bio-Impedance Variations into Cardiac and Respiratory Components. 2009.
48. **Vineeth Govind**. DfT-Based External Test and Diagnosis of Mesh-like Networks on Chips. 2009.
49. **Andres Kull**. Model-Based Testing of Reactive Systems. 2009.
50. **Ants Torim**. Formal Concepts in the Theory of Monotone Systems. 2009.
51. **Erika Matsak**. Discovering Logical Constructs from Estonian Children Language. 2009.
52. **Paul Annus**. Multichannel Bioimpedance Spectroscopy: Instrumentation Methods and Design Principles. 2009.
53. **Maris Tõnso**. Computer Algebra Tools for Modelling, Analysis and Synthesis for Nonlinear Control Systems. 2010.
54. **Aivo Jürgenson**. Efficient Semantics of Parallel and Serial Models of Attack Trees. 2010.
55. **Erkki Joason**. The Tactile Feedback Device for Multi-Touch User Interfaces. 2010.
56. **Jürgo-Sören Preden**. Enhancing Situation – Awareness Cognition and Reasoning of Ad-Hoc Network Agents. 2010.
57. **Pavel Grigorenko**. Higher-Order Attribute Semantics of Flat Languages. 2010.

58. **Anna Rannaste.** Hierarcical Test Pattern Generation and Untestability Identification Techniques for Synchronous Sequential Circuits. 2010.
59. **Sergei Strik.** Battery Charging and Full-Featured Battery Charger Integrated Circuit for Portable Applications. 2011.
60. **Rain Ottis.** A Systematic Approach to Offensive Volunteer Cyber Militia. 2011.
61. **Natalja Sleptšuk.** Investigation of the Intermediate Layer in the Metal-Silicon Carbide Contact Obtained by Diffusion Welding. 2011.
62. **Martin Jaanus.** The Interactive Learning Environment for Mobile Laboratories. 2011.
63. **Argo Kasemaa.** Analog Front End Components for Bio-Impedance Measurement: Current Source Design and Implementation. 2011.
64. **Kenneth Geers.** Strategic Cyber Security: Evaluating Nation-State Cyber Attack Mitigation Strategies. 2011.
65. **Riina Maigre.** Composition of Web Services on Large Service Models. 2011.
66. **Helena Kruus.** Optimization of Built-in Self-Test in Digital Systems. 2011.
67. **Gunnar Piho.** Archetypes Based Techniques for Development of Domains, Requirements and Software. 2011.
68. **Juri Gavšin.** Intrinsic Robot Safety Through Reversibility of Actions. 2011.
69. **Dmitri Mihhailov.** Hardware Implementation of Recursive Sorting Algorithms Using Tree-like Structures and HFSM Models. 2012.
70. **Anton Tšertov.** System Modeling for Processor-Centric Test Automation. 2012.
71. **Sergei Kostin.** Self-Diagnosis in Digital Systems. 2012.
72. **Mihkel Tagel.** System-Level Design of Timing-Sensitive Network-on-Chip Based Dependable Systems. 2012.
73. **Juri Belikov.** Polynomial Methods for Nonlinear Control Systems. 2012.
74. **Kristina Vassiljeva.** Restricted Connectivity Neural Networks based Identification for Control. 2012.
75. **Tarmo Robal.** Towards Adaptive Web – Analysing and Recommending Web Users` Behaviour. 2012.
76. **Anton Karputkin.** Formal Verification and Error Correction on High-Level Decision Diagrams. 2012.
77. **Vadim Kimlaychuk.** Simulations in Multi-Agent Communication System. 2012.
78. **Taavi Viilukas.** Constraints Solving Based Hierarchical Test Generation for Synchronous Sequential Circuits. 2012.

79. **Marko Kääramees.** A Symbolic Approach to Model-based Online Testing. 2012.
80. **Enar Reilent.** Whiteboard Architecture for the Multi-agent Sensor Systems. 2012.
81. **Jaan Ojarand.** Wideband Excitation Signals for Fast Impedance Spectroscopy of Biological Objects. 2012.
82. **Igor Aleksejev.** FPGA-based Embedded Virtual Instrumentation. 2013.
83. **Juri Mihhailov.** Accurate Flexible Current Measurement Method and its Realization in Power and Battery Management Integrated Circuits for Portable Applications. 2013.
84. **Tõnis Saar.** The Piezo-Electric Impedance Spectroscopy: Solutions and Applications. 2013.
85. **Ermo Täks.** An Automated Legal Content Capture and Visualisation Method. 2013.
86. **Uljana Reinsalu.** Fault Simulation and Code Coverage Analysis of RTL Designs Using High-Level Decision Diagrams. 2013.
87. **Anton Tšepurov.** Hardware Modeling for Design Verification and Debug. 2013.
88. **Ivo Müürsepp.** Robust Detectors for Cognitive Radio. 2013.
89. **Jaas Ježov.** Pressure sensitive lateral line for underwater robot. 2013.
90. **Vadim Kaparin.** Transformation of Nonlinear State Equations into Observer Form. 2013.
92. **Reeno Reeder.** Development and Optimisation of Modelling Methods and Algorithms for Terahertz Range Radiation Sources Based on Quantum Well Heterostructures. 2014.
93. **Ants Koel.** GaAs and SiC Semiconductor Materials Based Power Structures: Static and Dynamic Behavior Analysis. 2014.
94. **Jaan Übi.** Methods for Coopetition and Retention Analysis: An Application to University Management. 2014.
95. **Innokenti Sobolev.** Hyperspectral Data Processing and Interpretation in Remote Sensing Based on Laser-Induced Fluorescence Method. 2014.
96. **Jana Toompuu.** Investigation of the Specific Deep Levels in  $p$ -,  $i$ - and  $n$ -Regions of GaAs  $p^+pin-n^+$  Structures. 2014.
97. **Taavi Salumäe.** Flow-Sensitive Robotic Fish: From Concept to Experiments. 2015.
98. **Yar Muhammad.** A Parametric Framework for Modelling of Bioelectrical Signals. 2015.
99. **Ago Mõlder.** Image Processing Solutions for Precise Road Profile Measurement Systems. 2015.

100. **Kairit Sirts**. Non-Parametric Bayesian Models for Computational Morphology. 2015.
101. **Alina Gavrijaševa**. Coin Validation by Electromagnetic, Acoustic and Visual Features. 2015.
102. **Emiliano Pastorelli**. Analysis and 3D Visualisation of Microstructured Materials on Custom-Built Virtual Reality Environment. 2015.
103. **Asko Ristolainen**. Phantom Organs and their Applications in Robotic Surgery and Radiology Training. 2015.
104. **Aleksei Tepljakov**. Fractional-order Modeling and Control of Dynamic Systems. 2015.
105. **Ahti Lohk**. A System of Test Patterns to Check and Validate the Semantic Hierarchies of Wordnet-type Dictionaries. 2015.
106. **Hanno Hantson**. Mutation-Based Verification and Error Correction in High-Level Designs. 2015.
107. **Lin Li**. Statistical Methods for Ultrasound Image Segmentation. 2015.
108. **Aleksandr Lenin**. Reliable and Efficient Determination of the Likelihood of Rational Attacks. 2015.
109. **Maksim Gorev**. At-Speed Testing and Test Quality Evaluation for High-Performance Pipelined Systems. 2016.
110. **Mari-Anne Meister**. Electromagnetic Environment and Propagation Factors of Short-Wave Range in Estonia. 2016.
111. **Syed Saif Abrar**. Comprehensive Abstraction of VHDL RTL Cores to ESL SystemC. 2016.
112. **Arvo Kaldmäe**. Advanced Design of Nonlinear Discrete-time and Delayed Systems. 2016.
113. **Mairo Leier**. Scalable Open Platform for Reliable Medical Sensorics. 2016.
114. **Georgios Giannoukos**. Mathematical and Physical Modelling of Dynamic Electrical Impedance. 2016.
115. **Aivo Anier**. Model Based Framework for Distributed Control and Testing of Cyber-Physical Systems. 2016.
116. **Denis Firsov**. Certification of Context-Free Grammar Algorithms. 2016.
117. **Sergei Astatpov**. Distributed Signal Processing for Situation Assessment in Cyber-Physical Systems. 2016.
118. **Erkki Moorits**. Embedded Software Solutions for Development of Marine Navigation Light Systems. 2016.
119. **Andres Ojamaa**. Software Technology for Cyber Security Simulations. 2016.